

## Microstructural phenomena in pearlitic railway steels

Mattos Ferreira, V.

**DOI**

[10.4233/uuid:facb282f-74a1-446d-bbc6-5ed294602ed2](https://doi.org/10.4233/uuid:facb282f-74a1-446d-bbc6-5ed294602ed2)

**Publication date**

2024

**Document Version**

Final published version

**Citation (APA)**

Mattos Ferreira, V. (2024). *Microstructural phenomena in pearlitic railway steels*. [Dissertation (TU Delft), Delft University of Technology]. <https://doi.org/10.4233/uuid:facb282f-74a1-446d-bbc6-5ed294602ed2>

**Important note**

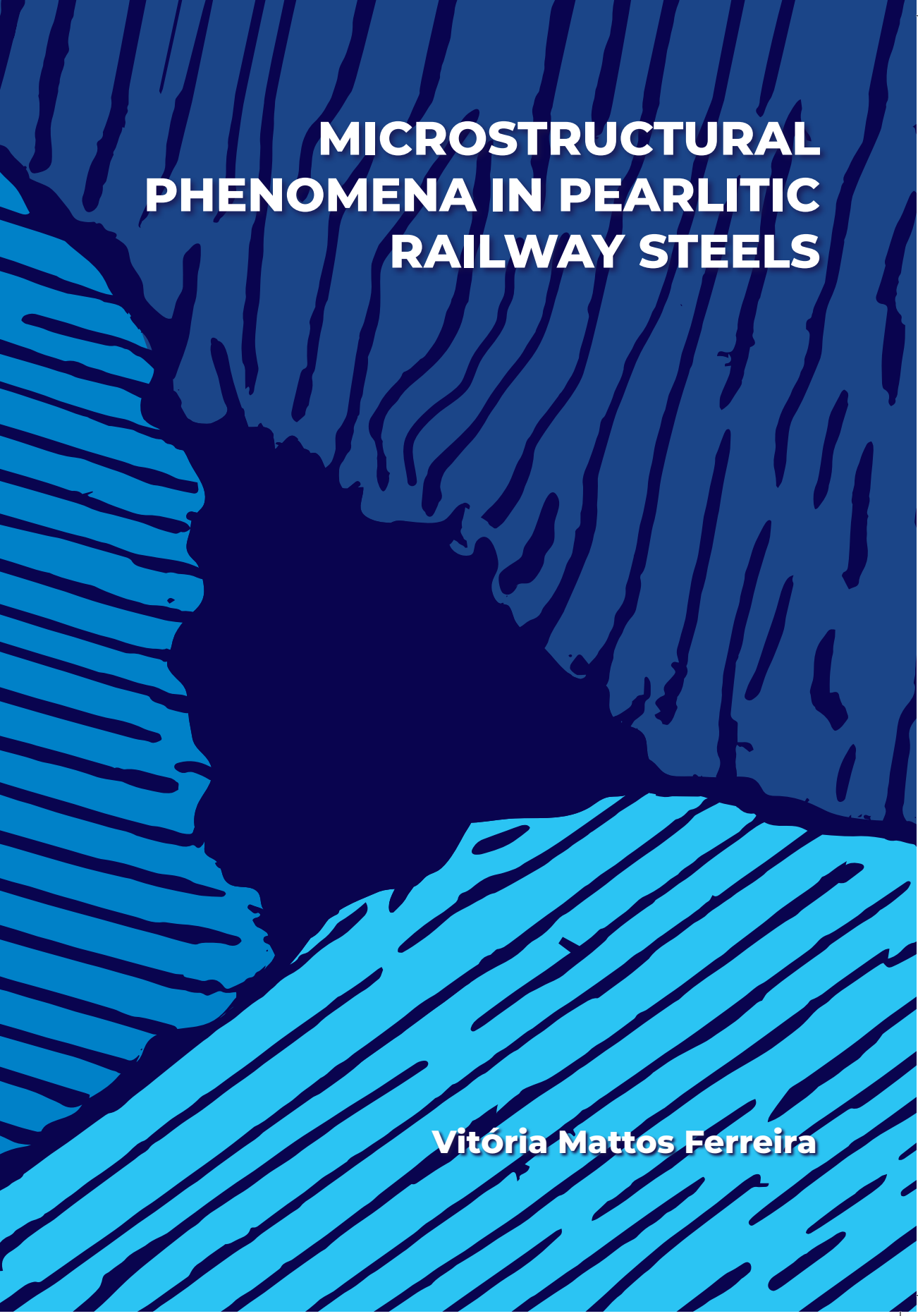
To cite this publication, please use the final published version (if applicable). Please check the document version above.

**Copyright**

Other than for strictly personal use, it is not permitted to download, forward or distribute the text or part of it, without the consent of the author(s) and/or copyright holder(s), unless the work is under an open content license such as Creative Commons.

**Takedown policy**

Please contact us and provide details if you believe this document breaches copyrights. We will remove access to the work immediately and investigate your claim.

The background of the cover is a stylized, high-contrast representation of a pearlitic microstructure. It features a central, dark, irregularly shaped region that resembles a pearlite colony. This central region is surrounded by a dense field of parallel, slightly wavy lines that represent the lamellar structure of pearlite. The lines are drawn in a dark blue color against a lighter blue background, creating a strong visual texture that mimics the appearance of a metal micrograph under a microscope.

# **MICROSTRUCTURAL PHENOMENA IN PEARLITIC RAILWAY STEELS**

**Vitória Mattos Ferreira**

# **MICROSTRUCTURAL PHENOMENA IN PEARLITIC RAILWAY STEELS**



# **MICROSTRUCTURAL PHENOMENA IN PEARLITIC RAILWAY STEELS**

## **Dissertation**

for the purpose of obtaining the degree of doctor  
at Delft University of Technology  
by the authority of the Rector Magnificus prof.dr.ir. T.H.J.J. van der Hagen  
chair of the Board for Doctorates  
to be defended publicly on  
Friday 8<sup>th</sup> of March 2024 at 12:30h

by

**Vitória MATTOS FERREIRA**

Bachelor of Science in Materials Science and Engineering,  
Universidade Federal do Rio de Janeiro, Brazil  
born in Rio de Janeiro, Brazil.

This dissertation has been approved by the promotors.

Composition of the doctoral committee:

Rector Magnificus,	chairperson
Prof. dr. ir. J. Sietsma	Delft University of Technology, promotor
Prof. dr. ir. R.H. Petrov	Delft University of Technology and University of Ghent, promotor

Independent members:

Prof. dr. ir. R.P.B.J. Dollevoet	Delft University of Technology
Prof. dr. M. Militzer	The University of British Columbia
Prof. dr. H. Goldenstein	São Paulo University
Dr. P. R. Yan	SKF Technology

Other member:

Dr. M.G. Mecozzi	Delft University of Technology, daily supervisor
------------------	--

Reserve member:

Prof. dr. M. Santofimia Navarro	Delft University of Technology
---------------------------------	--------------------------------



Rijksdienst voor Ondernemend  
Nederland



**ProRail**

This research was carried out under project number S16042a in the framework of the Partnership Program of the Materials Innovation Institute M2i ([www.m2i.nl](http://www.m2i.nl)) and the Technology Foundation TTW ([www.stw.nl](http://www.stw.nl)), which is part of the Netherlands Organization for Scientific Research ([www.nwo.nl](http://www.nwo.nl)).

Printed by Ridderprint | [www.ridderprint.nl](http://www.ridderprint.nl)

Cover design: Joey Roberts | [www.ridderprint.nl](http://www.ridderprint.nl)

ISBN 978-94-6483-777-3

An electronic version of this dissertation is available at  
<http://repository.tudelft.nl/>.

Copyright © 2024 by Vitória Mattos Ferreira

*Aos meus avós Jirvânio e Sônia,  
Aos meus pais Robson e Elizângela.*





# Contents

<b>Summary</b>	<b>ix</b>
<b>Samenvatting</b>	<b>xiii</b>
<b>List of Figures</b>	<b>xvi</b>
<b>List of Tables</b>	<b>xxii</b>
<b>1 Introduction</b>	<b>1</b>
1.1 Theoretical Background . . . . .	2
1.1.1 Railway pearlitic steels . . . . .	2
1.1.2 White and Brown Etching Layers in railway steels . . . . .	3
1.2 Thesis Outline . . . . .	6
<b>2 Microstructure development of pearlitic railway steels subjected to fast heating</b>	<b>9</b>
2.1 Introduction . . . . .	10
2.2 Material and Methods . . . . .	11
2.2.1 Material . . . . .	11
2.2.2 Methods . . . . .	12
2.3 Results and Discussion . . . . .	14
2.3.1 Heating . . . . .	14
2.3.2 Prior-austenite grain size . . . . .	16
2.3.3 Slow cooling (0.1 and 1 °Cs <sup>-1</sup> ) . . . . .	18
2.3.4 Intermediate cooling (10 °Cs <sup>-1</sup> ) . . . . .	20
2.3.5 Fast cooling (Quench) . . . . .	22
2.3.6 Cyclic heating and cooling . . . . .	23
2.3.7 Microhardness . . . . .	25
2.3.8 CCT diagram . . . . .	26
2.3.9 Comparison with WEL from field . . . . .	27
2.4 Conclusions . . . . .	28
<b>3 Details of pearlite to austenite transformation in steel: experiments and phase-field modeling</b>	<b>31</b>
3.1 Introduction . . . . .	32
3.2 Material and experimental procedure . . . . .	33
3.3 Experimental results . . . . .	35
3.4 Phase-Field Modelling . . . . .	38

3.4.1	Phase-field theory . . . . .	38
3.4.2	Simulation conditions . . . . .	39
3.4.3	Simulation results . . . . .	41
3.5	Conclusions . . . . .	49
<b>4</b>	<b>Microstructure and mechanical response of field and laser-induced white and brown etching layers</b>	<b>51</b>
4.1	Introduction . . . . .	52
4.2	Material and methods . . . . .	53
4.3	Results . . . . .	53
4.3.1	Microstructural characterization . . . . .	53
4.3.2	Nanoindentation . . . . .	57
4.4	Discussion . . . . .	58
4.5	Conclusions . . . . .	63
<b>5</b>	<b>Microstructural characterization of hypereutectoid pearlitic steel containing vanadium</b>	<b>65</b>
5.1	Introduction . . . . .	66
5.2	Material and methods . . . . .	67
5.2.1	Material . . . . .	67
5.2.2	Methods . . . . .	68
5.3	Results . . . . .	69
5.3.1	Interlamellar spacing and hardness . . . . .	69
5.3.2	Grain boundary phases . . . . .	69
5.3.3	Thermodynamics and kinetics analysis . . . . .	72
5.3.4	Tensile behavior . . . . .	76
5.4	Conclusions . . . . .	78
<b>6</b>	<b>Conclusions and Recommendations</b>	<b>81</b>
<b>A</b>	<b>MICRESS driving file</b>	<b>85</b>
A.1	MICRESS driving file example . . . . .	86
	<b>List of Publications</b>	<b>109</b>
	<b>Acknowledgements</b>	<b>111</b>
	<b>Agradecimientos</b>	<b>115</b>
	<b>Biography</b>	<b>119</b>

# SUMMARY

The railway industry constantly seeks advancements in train speed, axle load capacity, reliability, and rail longevity. Rails undergo complex and severe loading during operation due to wheel/rail contact, resulting in two main damage mechanisms: rolling contact fatigue (RCF) and wear. Furthermore, frictional heating during wheel/rail contact causes local temperature rise, leading to microstructural processes on the rail surface, known as white etching layer (WEL) and brown etching layer (BEL). This project aims to gain insight into the microstructural changes in rail steels, with a primary focus on understanding the origins of detrimental surface layers like WEL and BEL. By achieving this understanding, the lifespan of the rails can be extended and the maintenance frequency can be reduced, which has significant effects on the sustainability of the railway network as well as overall life cycle costs. Additionally, the project explores the microstructural characteristics of recently developed steel grades with enhanced resistance to rolling contact fatigue.

In **Chapter 2**, the microstructural evolution of standard pearlitic railway steel (R260Mn grade) subjected to fast heating and different cooling conditions is analyzed and discussed. The material is subjected to different heat treatments using a dilatometer. The first set of heat treatments considered fast heating at  $200\text{ }^{\circ}\text{C s}^{-1}$  immediately followed by cooling at different cooling rates (0.1, 1,  $10\text{ }^{\circ}\text{C s}^{-1}$  and quench), while the second heat treatment had an additional soaking for 5 minutes at  $900\text{ }^{\circ}\text{C}$  before cooling at the same cooling rates. Additional cyclic heating and quenching was performed to investigate the microstructural evolution during thermal cycling due to its relevance for railway applications. The final microstructure is characterized via microhardness measurements, optical microscopy, and scanning electron microscopy. The microstructural features are distinguished and the influence of each condition is detailed. The study allows the construction of transformation diagrams during cooling after fast heating which can serve as a guideline for future reproduction of White Etching Layers in laboratory conditions and interpretation of field conditions, in which also deformation plays a role. The results suggest that phase transformation is the dominant aspect of WEL formation due to a comparable hardness obtained for the WEL produced in laboratory (fast heating + quenching) and the one from field conditions. However, the nanosized grains commonly observed in WELs formed during wheel and rail contact are not reproducible only by thermal heating, suggesting the importance of severe plastic deformation on the grain refinement.

Due to the complexity of understanding the mechanisms of austenite formation at high temperatures in a controlled laboratory environment, multiphase-field modeling is used in **Chapter 3**. This study aims to provide insight into the WEL formation in pearlitic railway steels. The simulations consider the fast heating of an initial pearlitic microstructure with resolved cementite and ferrite lamellae, together with boundary pro-eutectoid ferrite. The austenite growth kinetics and microstructural morphology obtained via simulations are compared with dilatometry and scanning electron microscopy observations of partially austenitized samples. The influence of  $\gamma/\theta$  and  $\gamma/\alpha$  mobilities on the austenite growth morphology are studied. The simulations reproduce the microstructural features

as well as the experimentally observed kinetics behavior of austenite formation, involving the correlation between mobilities and nucleation behavior. Phase field modeling allows the simulation of the different microstructural features of austenite formation from a pearlitic microstructure observed experimentally such as lamellae thinning, flat/sharp austenite front, preferential growth towards a specific pearlite colony and reduced kinetics during pro-eutectoid ferrite dissolution. The simulations also show that different austenite morphologies are obtained according to the values of  $\gamma/\alpha$  and  $\gamma/\theta$  interface mobilities. Furthermore, carbon concentration gradients are observed in both austenite and ferrite for simulations with 10 and 200 °Cs<sup>-1</sup>. These gradients are much stronger for higher heating rates, which is due to the lack of time for carbon to homogenize in austenite. These carbon gradients can lead to inhomogeneities in the microstructure during intercritical heating and cooling such as rails are subjected to in the field.

The focus of **Chapter 4** is on the microstructural characterization and mechanical response of field and laser-induced WEL and BEL. The laser treatment consisted of two passes with low and high speeds to have different heat-affected zones, leading to the formation of a microstructure gradient with WEL and BEL characteristics. The microstructural features of field and laser-induced WEL and BEL are revealed by Light Optical Microscopy and Scanning Electron Microscopy, while nanoindentation allowed the mapping of the hardness variations within each layer. The observations are discussed in terms of the underlying microstructural processes. The laser-induced WEL and BEL layers presented in this chapter show similar microstructural features and hardness as field WEL and BEL. The most distinguishable aspect is the dimensions of these features which are much larger in the layers formed via laser treatment. This might be related to the absence of plastic deformation as only temperature rise is considered in the laser heat treatment. Additionally, laser and field BEL consist of an inhomogeneous microstructure varying along the depth of these layers, suggesting different stages of phase transformation. The different aspects of the investigated WEL and BEL strongly support the hypothesis that the WEL is martensite while the BEL is tempered martensite formed due to the reheating of previously formed WEL. The laser heat treatment also confirmed that WEL and BEL can be formed without severe plastic deformation, demonstrating the importance of high temperatures in the formation of these layers.

Recent developments in railway steel grades have led to improvements in track performance. In **Chapter 5**, the role of vanadium in the microstructure and mechanical behavior of hypereutectoid pearlitic rail steels is investigated. A series of microstructural characterization techniques (Scanning Electron Microscopy and Transmission Electron Microscopy) are used to identify the phases formed at grain boundaries, to determine the interlamellar spacings, and to observe vanadium carbide precipitation. Additionally, the precipitation behavior of vanadium carbide and cementite at the austenite grain boundary is simulated as diffusion-controlled phase transformations using DICTRA. The mechanical behavior of this steel is studied using tensile tests, and the results are compared to those of a standard vanadium-free R260 eutectoid rail steel grade. It is found that the vanadium-containing steel has a slight vanadium enrichment in the pearlitic cementite lamellae, small and randomly distributed VC precipitates within the pearlitic ferrite, and some precipitates containing vanadium at the grain boundaries. The thermodynamic calculations and DICTRA simulations indicate that the presence of boundary ferrite in hypereutectoid steels is due to the carbon depletion of austenite in the vicinity of the boundary cementite particles to

levels below the eutectoid composition. The effect of VC on austenite carbon depletion by itself is not enough for ferrite formation. However, these carbides can play a role in the restriction of the cementite growth along the austenite boundaries.

Finally, a summary of the main conclusions of the thesis is provided in **Chapter 6** together with recommendations for future work, mainly focusing on a more detailed characterization of different WEL and BEL analyzed in this thesis.



# SAMENVATTING

De spoorwegindustrie streeft voortdurend naar verbeteringen op het gebied van treinsnelheid, aslastvermogen, betrouwbaarheid en levensduur van het spoor. Rails ondergaan tijdens het gebruik een complexe en zware belasting als gevolg van wiel-railcontact, hetgeen resulteert in twee belangrijke schademechanismen: rolcontactvermoeiing (RCF) en slijtage. Bovendien veroorzaakt opwarming door wrijving tijdens wiel-rail contact lokale stijging van de temperatuur, hetgeen leidt tot microstructurele processen op het railoppervlak, waarbij wit-etsende lagen (WEL) en bruin-etsende lagen (BEL) gevormd kunnen worden. Dit project heeft tot doel inzicht te verkrijgen in de microstructurele veranderingen in railstaal, met een primaire focus op het begrijpen van het ontstaan van schadelijke oppervlaktelagen zoals WEL en BEL. Door dit inzicht te verwerven kan de levensduur van de rails worden verlengd en de onderhoudsfrequentie worden verlaagd, hetgeen significante effecten heeft op de duurzaamheid van het spoorwegennetwerk. Ook kunnen kosten zo worden verlaagd. Daarnaast onderzoekt het project de microstructurele kenmerken van recent ontwikkelde staalsoorten met verbeterde weerstand tegen rolcontactvermoeidheid.

In **Hoofdstuk 2** wordt de microstructurele evolutie van standaard perlitisch spoorwegstaal (kwaliteit R260Mn) onderworpen aan snelle opwarming en verschillende afkoelingscondities geanalyseerd en besproken. Het materiaal wordt onderworpen aan verschillende warmtebehandelingen met behulp van een dilatometer. Bij de eerste reeks warmtebehandelingen werd uitgegaan van snelle opwarming met  $200\text{ }^{\circ}\text{Cs}^{-1}$ , onmiddellijk gevolgd door afkoeling met verschillende snelheden ( $0,1$ ,  $1$ ,  $10\text{ }^{\circ}\text{Cs}^{-1}$  en afschrikken), terwijl bij de tweede reeks warmtebehandelingen een extra behandeling werd toegepast van 5 minuten bij  $900\text{ }^{\circ}\text{C}$  alvorens af te koelen met dezelfde snelheden. Daarnaast werd cyclisch opwarmen en afschrikken uitgevoerd om de microstructurele evolutie tijdens thermische cycli te onderzoeken vanwege de relevantie daarvan voor spoorwegtoepassingen. De uiteindelijke microstructuur werd gekarakteriseerd via microhardheidsmetingen, optische microscopie en scanning-elektronenmicroscopie. De microstructurele kenmerken worden geïdentificeerd en de invloed van elke warmtebehandeling wordt gedetailleerd. De studie maakt de constructie mogelijk van transformatiediagrammen tijdens afkoeling na snelle opwarming, die kunnen dienen als richtlijn voor toekomstige reproductie van wit-etsende lagen in laboratoriumomstandigheden en interpretatie van veldomstandigheden. De resultaten suggereren dat fase-transformatie het dominante aspect is van WEL-vorming vanwege een vergelijkbare hardheid die wordt verkregen voor de WEL geproduceerd in het laboratorium (snelle verwarming + afschrikken) en die onder veldomstandigheden, waarin ook deformatie een rol speelt. De korrels met een grootte in de nanometer-range die gewoonlijk worden waargenomen in WEL's die worden gevormd tijdens contact tussen wiel en rail, zijn echter niet reproduceerbaar door alleen thermische behandeling, hetgeen het belang van significante plastische vervorming op de korrelverfijning suggereert.

Vanwege de complexiteit van het begrijpen van de mechanismen van austenietvorming bij hoge temperaturen in een gecontroleerde laboratoriumomgeving, wordt in **Hoofdstuk 3** Phase Field modellering toegepast. Deze studie heeft tot doel inzicht te verschaffen in de

WEL-vorming in perlitisch spoorwegstaal. De simulaties houden rekening met de snelle opwarming van een initiële perlitische microstructuur met onderscheiden cementiet- en ferrietlamellen, samen met pro-eutectoïdisch ferriet op korrelgrenzen. De kinetiek van austenietgroei en microstructurele morfologie verkregen via simulaties worden vergeleken met waarnemingen met dilatometrie en scanning-elektronenmicroscopie van gedeeltelijk geaustenitiseerde monsters. De invloed van  $\gamma/\theta$  en  $\gamma/\alpha$  mobiliteiten op de austeniet-groeimorfologie wordt bestudeerd. De simulaties reproduceren zowel de microstructurele kenmerken als het experimenteel waargenomen kinetische gedrag van austenietvorming, waarbij de correlatie tussen mobiliteiten en nucleatiegedrag een rol speelt. Phase Field modellering maakt de simulatie mogelijk van de verschillende microstructurele kenmerken van austenietvorming uit een perlitische microstructuur die experimenteel worden waargenomen, zoals het dunner worden van lamellen, een vlak of scherp austenietgroeifront, preferentiële groei naar een specifieke perlietkolonie en afnemende kinetiek tijdens het oplossen van pro-eutectoïdisch ferriet. De simulaties laten ook zien dat verschillende austenietmorfologieën worden verkregen bij verschillende waarden van  $\gamma/\alpha$  en  $\gamma/\theta$  grensvlakmobiliteiten. Bovendien worden koolstofconcentratiegradiënten waargenomen in zowel austeniet als ferriet voor simulaties met 10 en 200 °Cs<sup>-1</sup>. Deze gradiënten zijn veel sterker bij hogere opwarmingssnelheden, hetgeen veroorzaakt wordt door het gebrek aan tijd voor koolstof om te homogeniseren in austeniet. Deze koolstofgradiënten kunnen leiden tot inhomogeniteiten in de microstructuur tijdens interkritische opwarming en afkoeling, zoals waaraan rails in het veld wordt blootgesteld.

De focus van **Hoofdstuk 4** ligt op de microstructurele karakterisering en mechanische respons van veld- en laser-geïnduceerde WEL en BEL. De laserbehandeling bestond uit twee passages met lage en hoge snelheden om verschillende warmte-beïnvloede zones te verkrijgen, hetgeen leidde tot de vorming van een microstructuurgradiënt met WEL- en BEL-karakteristieken. De microstructurele kenmerken van veld- en laser-geïnduceerde WEL en BEL worden onthuld door optische microscopie en scanning-elektronenmicroscopie, terwijl nano-indentatie het mogelijk maakte de hardheidsvariëaties in kaart te brengen binnen elke laag. De waarnemingen worden besproken in termen van de onderliggende microstructurele processen. De laser-geïnduceerde WEL en BEL die in dit hoofdstuk worden gepresenteerd vertonen vergelijkbare microstructurele kenmerken en hardheid als veld-WEL en -BEL. Het meest onderscheidende aspect zijn de afmetingen van deze kenmerken, die veel groter zijn in de lagen gevormd via laserbehandeling. Dit kan te maken hebben met de afwezigheid van plastische vervorming, aangezien bij de laserwarmtebehandeling alleen een hoge temperatuur wordt toegepast, zonder deformatie. De laser- en veld-BEL bestaan uit een inhomogene microstructuur die varieert over de diepte van deze lagen, hetgeen verschillende stadia van faseformatie suggereert. De verschillende aspecten van de onderzochte WEL en BEL ondersteunen sterk de hypothese dat de WEL martensiet is, terwijl de BEL ontlaten martensiet is, gevormd als gevolg van het opnieuw opwarmen van eerder gevormde WEL. De laserwarmtebehandeling bevestigt ook dat WEL en BEL kunnen worden gevormd zonder significante plastische vervorming, hetgeen het belang aantoont van hoge temperaturen bij de vorming van deze lagen.

Recente ontwikkelingen op het gebied van spoorwegstaalsoorten hebben geleid tot verbeteringen in de spoorprestaties. In **Hoofdstuk 5** wordt de rol van vanadium in de microstructuur en het mechanische gedrag van hypereutectoïdische perlitische railstaalsoorten onderzocht. Een reeks microstructurele karakteriseringstechnieken (Scanning Electron Mi-



croscopy en Transmission Electron Microscopy) worden gebruikt om de fasen te identificeren die worden gevormd bij korrelgrenzen, interlamellaire afstanden te meten en vanadiumcarbideprecipitatie waar te nemen. Bovendien wordt het precipitatiegedrag van vanadiumcarbide en cementiet op de austenietkorrelgrens gesimuleerd als diffusiegecontroleerde fasetransformaties met behulp van DICTRA. Het mechanische gedrag van dit staal wordt bestudeerd met behulp van trekproeven en de resultaten worden vergeleken met die van een standaard vanadiumvrije R260 eutectoïdische railstaalsoort. Er is gevonden dat het vanadiumhoudende staal een lichte vanadiumverrijking heeft in de perlitische cementietlamellen, kleine en willekeurig verdeelde VC-precipitaten in het perlitische ferriet, en verschillende precipitaten die vanadium bevatten aan de korrelgrenzen. De thermodynamische berekeningen en DICTRA-simulaties geven aan dat de aanwezigheid van korrelgrensferriet in hypereutectoïdische staalsoorten het gevolg is van de vermindering van de koolstofconcentratie in austeniet in de buurt van de cementietdeeltjes aan de korrelgrens tot niveaus onder de eutectoïdische samenstelling. Het effect van VC op de koolstofverarming van austeniet is op zichzelf niet voldoende voor de vorming van ferriet. Deze carbiden kunnen echter wel een rol spelen bij het beperken van de cementietgroei langs de austenietkorrelgrenzen.

Tenslotte wordt een samenvatting van de belangrijkste conclusies van het proefschrift gegeven in **Hoofdstuk 6**, samen met aanbevelingen voor toekomstig werk, waarbij de nadruk vooral ligt op een meer gedetailleerde karakterisering van de verschillende WEL en BEL die in dit proefschrift worden geanalyseerd.

# List of Figures

	<b>Page</b>
Figure 1.1 Scanning electron micrograph of a pearlitic steel showing the cementite (white contrast) and ferrite (dark contrast) lamellar microstructure.	2
Figure 1.2 WEL band at the rail surface and optical micrograph of the cross-section highlighting the featureless microstructure of the WEL after chemical etching with Nital. Adapted from [23]. . . . .	3
Figure 2.1 (a) Scanning electron microscopy image of the as-received R260Mn railway steel evidencing the pearlitic microstructure with the white arrow indicating pro-eutectoid ferrite at the grain boundaries and (b) Equilibrium transformation diagram of R260Mn steel calculated with Thermo-Calc software. . . . .	12
Figure 2.2 Graphical representation detailing the heat treatments performed using dilatometry. Heat treatments D consist of fast heating at $200\text{ }^{\circ}\text{C s}^{-1}$ up to $900\text{ }^{\circ}\text{C}$ and direct cooling with different cooling rates. Heat treatments S account for the same fast heating stage followed by intermediate soaking for 5 min at $900\text{ }^{\circ}\text{C}$ before cooling with different cooling rates. . . . .	13
Figure 2.3 (a) Heating stage of dilatometry curves for all specimens analyzed in this work with a focus on the intercritical temperature range where austenite formation takes place. Additionally, the SEM micrograph shows small patches of martensite (austenite at high temperatures) growing in the pearlitic matrix when the sample was heated up to $751\text{ }^{\circ}\text{C}$ followed by quench. (b) The heating stages of sample $D_{\text{cyclic}}$ with increasing order of the cycles is indicated with a red arrow. (c) Temperature and HF Power as a function of time for the first heating cycle of $D_{\text{cyclic}}$ . . . . .	15
Figure 2.4 Color coded unique grain color maps representing the reconstruction of PAGs from martensite variants according to Nishiyama-Wasserman (N-W) orientation relationship of samples $D_{\text{quench}}$ , $D_{\text{cyclic}}$ , $S_{\text{quench}}$ and $S_{0,1}$ using EDAX-TSL OIM Data analyses v8.3 software. . . . .	17

Figure 2.5	(a) Change in length as a function of temperature obtained during cooling in dilatometry tests for specimens subjected to both heat treatments (D - solid line and S - dashed line) with low cooling rates ( $0.1\text{ }^{\circ}\text{Cs}^{-1}$ - red and $1\text{ }^{\circ}\text{Cs}^{-1}$ - blue) together with theoretical FCC expansion curves used to calculate the phase fractions. (b) Transformation product fractions calculated for each cooling rate. . .	18
Figure 2.6	SEM images showing the differences between direct cooling (D-samples) and soaking (S-samples) for low cooling rates. Two different magnifications are used for $0.1$ and $1\text{ }^{\circ}\text{Cs}^{-1}$ samples to highlight the pearlite spheroidization in the former and the pre-eutectoid ferrite size and morphology in the latter. . . . .	19
Figure 2.7	(a) Change in length as a function of temperature curves obtained during cooling in dilatometry tests for specimens subjected to both heat treatments (D - solid line and S - dashed line) with intermediate cooling ( $10\text{ }^{\circ}\text{Cs}^{-1}$ ) together with theoretical FCC expansion curves used to calculate the transformed fractions. (b) Fractions of the microstructural constituents were calculated for each sample. . . . .	20
Figure 2.8	OM and SEM images of samples $D_{10}$ and $S_{10}$ revealing the banded structure composed of martensite (white contrast) and a mix of bainite and pearlite (dark contrast). The orientation is defined as RD - rolling direction, ND - normal direction (perpendicular to rail surface), and TD - transverse direction. . . . .	21
Figure 2.9	EPMA analysis of $D_{10}$ and $S_{10}$ showing Mn (red) and Si (blue) distribution along the banded structure. . . . .	21
Figure 2.10	(a) Change in length as a function of temperature curves obtained during dilatometry tests for specimens subjected to both heat treatments (D - red solid line and S - blue dashed line) with high cooling rates together with theoretical FCC expansion curves used to calculate the phase fractions. (b) Phase fraction calculated for each condition. .	22
Figure 2.11	SEM images showing the differences between direct cooling (D-samples) and soaking (S-samples) for quenched samples. Ghost pearlite is indicated with white arrows. . . . .	23
Figure 2.12	(a) Cooling portion of dilatometry curves for specimen subjected to cyclic heating and quenching. (b) Optimized heating portion of dilatometry curves not considering the axial contraction of the sample. (c) Optimized cooling portion of dilatometry curves not considering the axial contraction of the sample. . . . .	24
Figure 2.13	Vickers microhardness measurements of samples subjected to heat treatments D (direct cooling) and S (with soaking at high temperature). Two distinct measurements are presented for samples with cooling rates of $10\text{ }^{\circ}\text{Cs}^{-1}$ in order to differentiate the mechanical response of the banded structure. . . . .	25

Figure 2.14	Continuous Cooling Transformation diagram obtained via Thermo-Calc software and experimentally. The calculated CCT diagram (lines) considers two initial PAG sizes: 6 $\mu\text{m}$ (red) and 35 $\mu\text{m}$ (green). The experimental CCT (symbols) exposes the starting temperatures of the different transformations formed after heat treatments D (red) and S (green). . . . .	26
Figure 2.15	SEM images of samples subjected to (a) 1 cycle ( $D_{\text{quench}}$ ), (b) 10 cycles and (c) field WEL from a R260Mn steel. White arrows indicate the regions where ghost pearlite was observed. . . . .	27
Figure 3.1	Fe-C phase diagram for R260Mn steel obtained using Thermo-Calc software. The dashed line at 0.64 wt% C represents the carbon concentration in the studied alloy. Black arrows indicate the estimation for $A_1^-$ and $A_3$ temperatures under equilibrium conditions. . . . .	33
Figure 3.2	SEM micrographs of the as-received R260Mn railway steel (a) evidencing the pearlitic microstructure with the red arrow indicating pro-eutectoid ferrite at the grain boundaries and (b) higher magnification micrograph showing the interlamellar spacing and lamella thickness. . . . .	34
Figure 3.3	Dilatation and austenite phase fraction as a function of temperature for samples (a) $H_{900}$ and (b) $L_{900}$ ; (c) Time-temperature graph of $L_{745}$ and $H_{751}$ subjected to intercritical austenitization followed by quenching. . . . .	36
Figure 3.4	SEM image of martensitic patches found in samples $H_{751}$ (a-f) and $L_{745}$ (g-i). White arrows in (b) and (e) indicate sharp- and flat-front growth of austenite, respectively. Black arrows in (b) and (e) show the nuclei of austenite and the undissolved cementite, respectively. Dashed lines in (c) and (h) highlight the pearlite boundary. . . . .	37
Figure 3.5	Initial microstructure with the resolved cementite lamellae in the pearlitic microstructure used in the phase field simulations. . . . .	39
Figure 3.6	(a) Austenite phase fraction as a function of temperature obtained experimentally (black solid curve) and via phase field simulation with different pre-exponential factors for $\gamma/\theta$ mobility (colored lines with symbols) and (b) Number of austenite nuclei as a function of temperature for each simulation with different pre-exponential factors of $\gamma/\theta$ mobility. The unit of the interface mobilities is $\text{m}^4\text{J}^{-1}\text{s}^{-1}$ . . . . .	42
Figure 3.7	(a,b) Simulated microstructural evolution at $t = 1.5$ s and 2.5 s for different $\gamma/\theta$ pre-exponential factors ( $M_0^{\gamma/\theta}$ ) with red grains representing the austenite fase. (c) $\phi$ parameter for $t = 5$ s (fully transformed microstructure) for different $M_0^{\gamma/\theta}$ ( $\text{m}^4\text{J}^{-1}\text{s}^{-1}$ ), with colors indicating the $\phi$ parameter (see section 3.4.2). . . . .	43
Figure 3.8	(a) Carbon content in austenite ( $\gamma$ ) and ferrite ( $\alpha$ ) for highest and lowest $M_0^{\gamma/\theta}$ ( $\text{m}^4\text{J}^{-1}\text{s}^{-1}$ ); (b) Carbon content in $\gamma$ at $T = 739.65$ $^\circ\text{C}$ for simulation with $M_0^{\gamma/\theta} = 10^{-5}$ $\text{m}^4\text{J}^{-1}\text{s}^{-1}$ . . . . .	44

Figure 3.9	(a) Carbon concentration in $\gamma$ at the $\gamma/\theta$ interface along A-B line (see Figure 3.8b) and $\gamma/\alpha$ interface along A-C line (see Figure 3.8b) and the respective equilibrium values as a function of temperature; (b) Velocity of $\gamma/\theta$ (along A-B line) and $\gamma/\alpha$ (along A-C line) interfaces as a function of temperature. The simulation considered $M_0^{\gamma/\theta} = 10^{-5} \text{ m}^4\text{J}^{-1}\text{s}^{-1}$ . . . . .	45
Figure 3.10	(a) Carbon content in $\gamma$ at 739.45 °C and 739.85 °C for simulation with $M_0^{\gamma/\theta} = 10^{-5} \text{ m}^4\text{J}^{-1}\text{s}^{-1}$ . (b) Carbon profile in $\gamma$ across D-E line ( $T = 739.45 \text{ °C}$ ) and D'-E' line ( $T = 739.85 \text{ °C}$ ). . . . .	46
Figure 3.11	(a) Austenite phase fraction as a function of temperature obtained experimentally (black solid curve) and via phase field simulation with different pre-exponential factors for $\gamma/\alpha$ mobility (colored lines with symbols) and (b) Number of austenite nuclei as a function of time for each simulation with different pre-exponential factors of $\gamma/\alpha$ mobility ( $\text{m}^4\text{J}^{-1}\text{s}^{-1}$ ). . . . .	47
Figure 3.12	(a,b) Simulated microstructural evolution at $t = 1.5 \text{ s}$ and $2.5 \text{ s}$ for different $\gamma/\alpha$ pre-exponential factors ( $M_0^{\gamma/\alpha}$ ) with red grains representing the austenite phase. (c) $\phi$ parameter for $t = 5 \text{ s}$ (fully transformed microstructure) for different $M_0^{\gamma/\alpha}$ ( $\text{m}^4\text{J}^{-1}\text{s}^{-1}$ ), with colors indicating the $\phi$ parameter (see section 3.4.2). . . . .	48
Figure 3.13	(a) Phase evolution and (b) carbon content in austenite (top) and ferrite (bottom) of a selected area (black square) for simulation considering $200 \text{ °C s}^{-1}$ at $t = 0.19 \text{ s}$ ( $758 \text{ °C}$ ). (c) Austenite fraction as a function of temperature obtained experimentally and via simulation at a heating rate of $200 \text{ °C s}^{-1}$ . . . . .	49
Figure 4.1	(a) Light optical micrograph of field WEL found in MHH steel with red rectangle highlighting the location where nanoindentation was performed; SEM micrographs at the (b) top of the WEL, (c) bottom of the WEL and (d) interface between WEL and pearlite matrix with the interface highlighted by a dashed red line. . . . .	54
Figure 4.2	(a) Light optical micrograph of field WEL and BEL found in MHH steel with red rectangle highlighting the location where nanoindentation was performed; SEM micrographs at the (b) WEL, (c) top of the BEL, (d) center of the BEL and, (e) interface between BEL and pearlite matrix with the interface highlighted by a dashed red line. The dark semi-circular region within the red rectangle is a moisture stain that formed during sample preparation. . . . .	55
Figure 4.3	(a) Light optical micrograph of WEL and BEL formed through laser heating of MHH steel with red rectangle highlighting the location where nanoindentation was performed; SEM micrographs at the (b) WEL, (c) top of the BEL, (d) center of the BEL, and (e) interface between BEL and pearlite matrix with the interface highlighted by a dashed red line. . . . .	56

Figure 4.4	Dark field optical micrograph (left) of nanoindentation location with the nanohardness mapping (right) for (a) field WEL/pearlite sample, (b) field WEL/BEL/pearlite sample, and (c) laser WEL/BEL/pearlite sample. Dotted lines represent the interfaces between the different layers. . . . .	57
Figure 4.5	Schematic showing the estimated temperature ranges at different depths for each laser pass. . . . .	60
Figure 4.6	Histogram of the hardness with the normal distribution obtained for the three samples analyzed in this chapter: (a) field WEL/pearlite, (b) field WEL/BEL/pearlite, and (c) laser WEL/BEL/pearlite. The dotted line is the sum of the distributions given by the solid lines. . . . .	61
Figure 4.7	Average hardness of the field and laser BEL as a function of depth from the WEL/BEL interface. . . . .	63
Figure 5.1	Sectioning description of the railway rail head evidencing the location of the samples used for microstructural analysis (middle of rail's head) and tensile samples (gauge corner of rail's head). . . . .	68
Figure 5.2	SEM micrograph depicting (a) the pearlitic lamellae and (b) the pearlite colonies of HP335 steel. . . . .	69
Figure 5.3	SEM micrographs depicting the boundary ferrite layers (white arrows) found at different depths from the surface of HP335 steel. . . . .	70
Figure 5.4	High-angle annular dark-field imaging (HAADF) and EDS mapping from the (a) cementite lamella region and (b) boundary region with the presence of VC (white arrows). (c) STEM bright-field image evidencing boundary ferrite and cementite (black arrows) of HP335 steel. . . . .	71
Figure 5.5	(a) Bright-field TEM image highlighting pearlitic ferrite region considered for the selected-area electron diffraction (SAED); (b) SAED evidencing the Baker-Nutting orientation relationship between VC precipitates and the ferrite matrix; (c) Dark-field image with a reduced aperture corresponding to the diffraction point highlighted in (b). . . . .	72
Figure 5.6	Fe-C phase diagram for HP335 steels obtained using Thermo-Calc software. The dashed lines represent the carbon concentration in the alloy studied. . . . .	73
Figure 5.7	DICTRA simulation scheme displaying at $t = 0$ the initial austenite ( $\gamma$ ) domain with width $w_\gamma$ , representing an austenite grain boundary, followed by VC growth at $t_1$ on the left extremity of the domain and cementite growth at a later stage ( $t_j$ ) on the right extremity of the domain. . . . .	73
Figure 5.8	Vanadium (a) and carbon (b) contents in $\gamma$ at the VC/ $\gamma$ and $\gamma/\theta$ interfaces for simulations with $w_\gamma$ equal to 500 nm and 1 $\mu\text{m}$ . (c) Carbon content as a function of the distance at the end of the simulation for $w_\gamma$ equal to 500 nm and 1 $\mu\text{m}$ . The VC, $\theta$ , and $\gamma$ regions are indicated with black arrows for each domain. . . . .	74

Figure 5.9	(a) Carbon content in $\gamma$ at the $\gamma/\theta$ interface with $w_\gamma$ equal to 1 $\mu\text{m}$ for different cooling rates. (b) Position of VC/ $\gamma$ and $\gamma/\theta$ interfaces as a function of temperature for simulations with $w_\gamma$ equal to 500 nm and 1 $\mu\text{m}$ together with the results for simulations considering only cementite formation. The green dot indicates the eutectoid point. . .	76
Figure 5.10	Engineering stress-strain curve obtained for HP335 and eutectoid R260 steel [144]. . . . .	77
Figure 5.11	SEM micrograph of (a) the tensile fracture surface evidencing the brittle fracture features and (b) cross-section plane. . . . .	78

# List of Tables

	<b>Page</b>
Table 2.1	Chemical composition (in wt.%) of as-received R260Mn steel . . . . . 12
Table 2.2	Quantification of the PAG size distribution . . . . . 18
Table 2.3	Phase fractions obtained via XRD for samples subjected to heat treatments D (direct cooling) and S (with soaking) with 0.1 and 1 °Cs <sup>-1</sup> . . . 19
Table 2.4	Phase fractions obtained via XRD for samples subjected to heat treatments D (direct cooling) and S (with soaking) with 10 °Cs <sup>-1</sup> . . . . . 20
Table 3.1	Kinetic parameters used in the simulations with MICRESS <sup>®</sup> . . . . . 40
Table 4.1	Average hardness and standard deviation of field and laser pearlite, WEL and BEL based on the individual normal distributions of each region (Figure 4.6). . . . . 62
Table 5.1	Chemical composition of HP335 steel. . . . . 67
Table 5.2	Tensile test results . . . . . 77



# 1

## INTRODUCTION

The railway industry plays an important role in shaping modern societies. As a fundamental pillar of transportation infrastructure, railways have been instrumental in stimulating economic growth by facilitating the efficient inland movement of goods and people. Additionally, railways significantly contribute to cost-effective and environmentally responsible transportation solutions, making them a key driver for a more sustainable society.

The railway industry is constantly requiring faster trains, higher axle loads, increased reliability, and longer service life. For a long time, researchers have been investigating different aspects of railway systems such as steel microstructures, contact loadings, and failure mechanisms, aiming at getting insight the complex phenomena taking place during wheel and rail contact. Although these studies have led to extensive insight, there is still a long way to go for full comprehension of these mechanisms.

To be adequate for rail track application, steel must meet certain requirements. The manufactured rails must have a high level of straightness and flatness. Good weldability is also important since rail tracks are continuously welded during installation. In addition, fatigue and wear resistance are essential to provide acceptable structural integrity and safety. Last but not least, material and lifetime costs are also decisive factors in guaranteeing commercial value [1]. Pearlitic steels, characterized by a lamellar microstructure (see Figure 1.1), are the most commonly used steels in railway tracks as these grant a satisfactory price-performance ratio. However, bainitic [2, 3, 4] and austenitic [5, 6, 7] steels can also be found in some railway track applications.

During service, rails are subjected to severe and complex loading conditions due to wheel/rail contact, which leads to rolling contact fatigue (RCF) and wear [8, 9]. Different factors such as steel properties, lubrication conditions, and contact loads can influence whether RCF or wear will be the dominant mechanism of rail damage. Since these two mechanisms contribute to rail degradation and failure, they are known as the main causes of rail maintenance and replacement [10, 11, 12]. Crack initiation can occur at the surface or subsurface of rails due to highly localized stresses in a small contact area of the rail's surface. Cyclic loading will then contribute to crack propagation until partial or complete failure, which can lead to train derailment [10, 12, 13]. In addition, local temperature increase due to frictional heating is another complication of the wheel/rail contact that can

lead to microstructural changes at the rail surface.

While analyzing the rail's surface after use (etched with Nital 2%), it is possible to find layers of approximately 10 to 100  $\mu\text{m}$  thickness with a distinctly different microstructure. These so-called White and Brown Etching Layers (WEL and BEL) are seen to be preferential sites for crack nucleation [13, 14]. Several theories have been suggested to explain the formation and morphology of these detrimental layers but none of them is fully accepted. More details on the literature information available regarding the WEL and BEL will be presented in the following sections of this chapter. The outline of this thesis is presented in section 1.2.

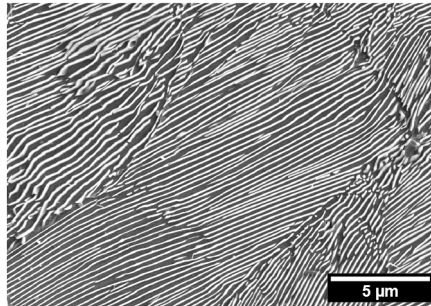


Figure 1.1: Scanning electron micrograph of a pearlitic steel showing the cementite (white contrast) and ferrite (dark contrast) lamellar microstructure.

## 1.1. THEORETICAL BACKGROUND

### 1.1.1. RAILWAY PEARLITIC STEELS

The most common steels used in railway applications are low-alloy C-Mn steels with carbon contents between 0.5 wt.% and 0.8 wt.%. Depending on the cooling rate during the process route, different types of final microstructures can be achieved. The composition of standard railway steel is close to eutectoid (e.g. R260 and R260Mn grades). Such steel has a pearlitic microstructure with some pro-eutectoid ferrite decorating the prior-austenite grain boundaries.

The pearlite has a lamellar structure consisting of alternating layers of soft ferrite and hard cementite. The distance between two consecutive lamellae of the same phase is known as interlamellar spacing, which has a strong influence on the strength of pearlitic steels and can be controlled in order to improve wear and rolling contact fatigue performances. For example, a reduction of the interlamellar spacing provides an increase in hardness [15, 16] and a reduction of the wear rate [17] as the cementite lamellae in the pearlite act as barriers against dislocation movement in ferrite [18].

One approach to refine the interlamellar spacing is by increasing the cooling rate of the steel during production [19]. The high cooling rates lower the eutectoid-transformation temperature which reduces the interlamellar spacing and suppresses the formation of pro-eutectoid ferrite [20]. Thus, the interlamellar spacing and fraction of pro-eutectoid ferrite along the grain boundaries are smaller, refining the pearlitic structure [9].

Alloying elements can also be beneficial to the strength and toughness of pearlitic rails. Silicon and manganese are known to be solid-solution strengtheners of ferrite [21]. In addi-

tion, manganese and chromium reduce the carbon content of the eutectoid composition, increasing pearlite fraction and refinement [11]. Niobium is also used, in small fractions, to ensure the formation of fine pearlite colonies since it refines the prior-austenite grain structure [11]. Vanadium can also be added to pearlitic steels with the main goal of improving the mechanical properties. Since vanadium is a strong carbide former, it has the potential to influence the composition of the pearlitic cementite and to promote additional carbide precipitation in the pearlitic microstructure, influencing the mechanical response of these steels.

### 1.1.2. WHITE AND BROWN ETCHING LAYERS IN RAILWAY STEELS

White Etching Layer (WEL) formation is a phenomenon that occurs in the rail surface during wheel and rail contact. This nomenclature is related to its high resistance to metallographic etching (Nital 2%) [22] resulting in a featureless microstructure under light microscopy, see Figure 1.2. The thickness of these layers can vary between 20 and 300  $\mu\text{m}$  depending on the loading and heating history of the investigated rail [23, 24]. As for the hardness of the WEL, values ranging from 700 to 1200 HV have been reported, which is much higher than for the pearlitic matrix of standard railway steels (around 300 HV) [25, 26].

In general, WELs are found associated with rolling contact fatigue (RCF) defects on the railway surface such as squats [27, 28] and spalling [29, 30]. Several aspects contribute to the WEL being considered as one of the main causes of microcrack formation: the brittle nature of the WEL due to high hardness, the different thermal expansion between WEL and pearlite matrix, and the presence of an interface region between WEL and pearlite matrix which contributes to crack propagation [14, 31, 32]. Therefore, WELs are important for determining the rails' service life. Understanding the formation of this detrimental layer and its composition and microstructure is essential for prolonging the rail service life, improving safety as well as developing effective maintenance strategies.

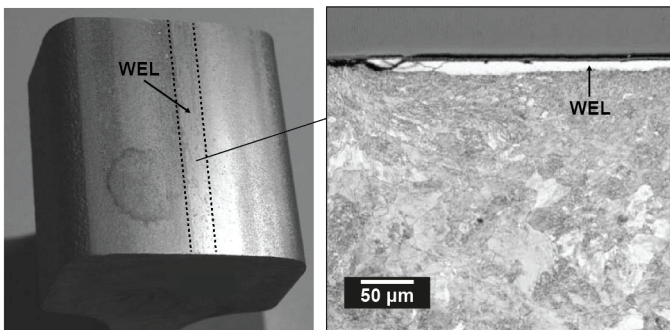


Figure 1.2: WEL band at the rail surface and optical micrograph of the cross-section highlighting the featureless microstructure of the WEL after chemical etching with Nital. Adapted from [23].

Over the past decades, researchers have conducted extensive studies to determine the formation mechanisms of WELs. Two hypotheses have emerged as the most prominent explanations for the origin of the WELs with the first proposing a combined thermomechanical mechanism, while the second suggests a purely mechanical mechanism.

The thermomechanical mechanism considers the effect of both thermal and mechan-

ical loadings on the phase transformations (pearlite-austenite-martensite) of the top surface of the rail head. WEL formed by a thermomechanical mechanism is usually associated with areas where the railway is exposed to significant acceleration and deceleration forces [27, 33], as well as during the customary rail maintenance procedures of grinding [34] and milling. In this case, the frictional heating is expected to be sufficient to increase the rail surface temperature to such values that it causes phase transformation from the initial pearlite to austenite. Subsequent fast cooling takes place due to the high thermal conductivity of the rail steel [35, 36] leading to the formation of a WEL containing the presence of martensite and some retained austenite [37].

Wu et al. [24] identified the presence of austenite diffraction peaks in the WEL of a pearlitic railway steel using X-Ray Diffraction. The presence of retained austenite was also confirmed by EBSD analysis. Kumar et al. [37] then used High-Resolution EBSD (HR-EBSD) to investigate the volume fraction of retained austenite within the WEL at various depths. They concluded that the observed lower fraction of retained austenite in the WEL at the top surface of the rail was related to the strain-induced austenite to martensite transformation. Osterle et al. [38] proposed that the WEL is actually martensite formed after austenitization coupled with severe plastic deformation. This conclusion is based on peak broadening in the X-ray diffraction pattern for BCC structure related to tetragonal distortion of the lattice indicating the presence of martensite. In this case, the WEL also accounted for undissolved cementite particles but no retained austenite was detected. Takahashi et al. [23] performed a detailed characterization of WEL using atom probe tomography. Cementite thinning was found within the WEL but not in the adjacent pearlitic matrix. The authors then suggested that the WEL was formed by phase transformation due to frictional heating as no evidence of heavy plastic deformation was observed at the rail surface. Thus, the main evidence for WELs formed due to a thermomechanical mechanism lies in the presence of retained austenite [14, 39, 40] within the WEL as well as the presence of not severely deformed pearlite beneath the rail WEL [41].

Nonetheless, some researchers argue that the limited time (milliseconds) during which the wheel and rail interact may not generate enough heat to elevate the temperature to austenitization levels. Given the challenge of directly measuring the temperature increase under field conditions, due to the short contact time and small contact area, simulation tools have been employed to substantiate the hypothesis of WEL formation due to frictional heating. Takahashi et al. [23, 42] used finite element modeling to calculate the frictional heating in the wheel and rail contact, confirming the possibility of temperature rise in the austenitization region up to 60  $\mu\text{m}$  below the surface. Wu et al. [41] simulated a Fe-C phase diagram under 1.8 GPa hydrostatic pressure. They observed that higher hydrostatic pressure leads to a reduction in austenitization temperature and eutectoid carbon concentration. Consequently, this can facilitate the formation of austenite at temperatures lower than those anticipated under equilibrium circumstances. In a recent study, Kumar et al. [37] simulated the temperature and contact stresses at the wheel/rail interface via finite element modeling. An increase up to 1200  $^{\circ}\text{C}$  was obtained for the rail surface while a temperature gradient was expected within the WEL. This temperature increase would be sufficient to austenitize the rail surface while the observed gradient within the material can lead to microstructural differences within the WEL.

As explained earlier, an alternative hypothesis for WEL formation suggests a purely mechanical mechanism. This secondary hypothesis emerged in response to two key obser-

variations: the absence of retained austenite and carbides within certain WELs and the presence of WELs in track sections characterized by minimal slippage, where temperature rise to austenitization temperatures would not be expected to occur. Thus, the mechanically-induced WELs origin can be associated with the dissolution of pearlitic cementite lamellae during cyclic severe deformation. The severe plastic deformation increases the dislocation density and strongly refines the grains in the pearlite at the rail surface, providing trapping sites for the carbon provenient from the cementite dissolution. Therefore, it is proposed that mechanically-induced WELs have a nanocrystalline ferritic microstructure with high dislocation density, supersaturated with carbon.

Newcomb and Stobbs [43] studied the WEL using the Transmission Electron Microscopy (TEM) technique. In their study, grain refinement, spheroidized cementite, and higher dislocation density of the ferrite were observed close to WEL regions. Even though the formation of a martensitic microstructure was suggested in this work, the unlikeliness of achieving austenitization temperatures under normal slippage conditions was reported. Thus, cementite decomposition without austenitization during the high-frequency shear fatigue of the rail surface was pointed out as the formation mechanism. Baumann et al. [44] and Lojkowski et al. [45, 46] defined the WEL as a nano-crystalline ferritic structure formed via cementite dissolution during severe cyclic plastic deformation below austenitization temperatures.

In summary, WELs can be classified into two different categories depending on their origin: thermomechanically or mechanically induced WEL. These two formation mechanisms can lead to differences in microstructure, hardness, mechanical properties, and the transition between WEL and the pearlitic matrix. For example, thermomechanically induced WELs are expected to have a sharp interface with the pearlitic matrix due to their thermal origin [23, 47]. This feature is accompanied by a sudden decrease in hardness from the WEL to the pearlite matrix, as well as a slightly deformed or undeformed pearlite matrix in the vicinity of the WEL [23, 48]. On the other hand, mechanically induced WELs are reported to exhibit a smoother decline in hardness, accompanied by a severely deformed pearlitic microstructure below these layers. Furthermore, WELs formed due to a purely mechanical process exhibit greater hardness compared to those induced by thermomechanical mechanisms, potentially attributable to the smaller grain size and higher dislocation density resulting from the severe plastic deformation in such cases [33, 49, 50].

The Brown Etching Layer (BEL) is another layer found at the rail surface with distinctly different microstructural features from both the WEL and the pearlitic matrix. Similarly to the WEL, the designation BEL comes from the brown contrast of this layer in light optical microscopy after etching with Nital. The hardness of this layer, often found between WEL and matrix, is approximately 500-600 HV, which is higher than the pearlitic matrix (300-400 HV) but lower than the WEL (700-1200 HV).

Messaadi and Steenbergen [51] characterized the BEL of three different rail steel grades from field service. A granular bainitic structure with martensite-austenite constituent was suggested for the BEL. The main reason lies in the fact that the thermal loading conditions of pearlitic rail steels can form other phases rather than martensite (WEL). Pal et al. [47] studied the overlapping of two thermomechanically induced WELs, resulting in the formation of BEL. The authors considered that the BEL originated from the tempering of the pre-existing WEL.

Kumar et al. [37] investigated the BEL features in a heat-treated pearlitic steel (R350HT).

The BEL consisted of a complex microstructure composed of ferrite, partially dissolved parent cementite, tempered martensite with secondary carbides, and martensite/austenite islands. EBSD phase maps pointed out a higher austenite fraction in the WEL than in the BEL, suggesting a higher temperature to have been achieved in the WEL region. In this work [37], two possible formation mechanisms of the BEL were suggested.

The first one claims that multiple plastic deformation and heating cycles below the  $A_1$  temperature lead to the fragmentation and/or partial dissolution of the cementite lamellae, followed by enrichment of the surrounding ferrite with carbon. However, some individual wheel/rail contact can raise the temperature above  $A_1$ , forming some islands of austenite that will become martensite during fast cooling. In regions close to the BEL center or the interface between BEL and base material, the temperature rise and time are not sufficient to grow large austenite grains. The final microstructure would then be composed of small islands of martensite/austenite, partially dissolved cementite, and ferrite.

The other option is that the pearlite is subjected to multiple plastic deformation and heating cycles above  $A_1$ . This can be achieved in regions close to the WEL/BEL interface, where temperatures are higher than deeper in the material. The austenite would then grow into larger islands and subsequently transform into martensite. If this microstructure is subjected to multiple temperature cycles in the martensite tempering regime (e.g. below  $A_1$ ), the result would be tempered martensite islands with secondary carbides, lower dislocation density due to tempering, partially dissolved cementite, ferrite and retained austenite.

In both cases, multiple cycles of plastic deformation and temperature rise (above or below  $A_1$ ) are necessary to achieve the final BEL microstructure.

## 1.2. THESIS OUTLINE

This project aims to determine the microstructural development in rail steels to improve damage-control strategies, mainly focusing on the origin of detrimental surface layers such as WEL and BEL, which were previously discussed. This allows for a possible reduction of maintenance frequency and life cycle costs, prolonging rails' lifetime and reducing energy consumption and emissions. Additionally, the project investigates the microstructural characteristics of recently developed steel grades with better resistance when subjected to rolling contact fatigue.

In **Chapter 2**, the microstructural evolution of a pearlitic railway steel (R260Mn grade) subjected to fast heating and different cooling conditions is analyzed and discussed. The material is subjected to different heat treatments using dilatometry. Additionally, the thermally induced formation of WEL in controlled laboratory conditions is explored. Cyclic fast heating and quenching are performed to investigate the effect of thermal cycling on the microstructural evolution. The microstructural features from the laboratory and field WEL are compared and the similarities are discussed and explained.

**Chapter 3** presents the simulation of the pearlite to austenite transformation using the multi-phase field approach. The simulation domain takes into account the resolved cementite and ferrite lamellae of three pearlite colonies and the presence of pro-eutectoid ferrite. The kinetics of phase transformation and the morphology of the austenite front are compared with experimental observations. The effects of different mobility of  $\gamma/\alpha$  and  $\gamma/\theta$  interfaces as well as the carbon distribution are discussed.

In **Chapter 4** the focus is on the microstructural characterization of a field and laser-

induced WEL and BEL. The laser treatment consisted of two passes with low and high speeds in order to have different heat-affected zones, leading to the formation of a microstructural gradient. The microstructural features of field and laser-induced WEL and BEL are compared. Furthermore, nanoindentation was used to obtain a mapping of the hardness variations within each layer. The observations are discussed in terms of the underlying microstructural processes.

**Chapter 5** focuses on the role of vanadium in the microstructure of hypereutectoid pearlitic rail steels. A series of microstructural characterization techniques are used to identify the phases formed at grain boundaries, interlamellar spacing, and vanadium carbide precipitation. The precipitation behavior of vanadium carbide and cementite at the austenite grain boundary is simulated using diffusion-controlled transformation kinetics DICTRA. Additionally, tensile tests are done to determine the changes in the mechanical behavior of these steels when compared with a vanadium-free standard rail grade.

Finally, **Chapter 6** offers an overview of the conclusions derived from the research presented in this thesis, accompanied by suggestions for addressing potential research areas in the future.





## 2

# MICROSTRUCTURE DEVELOPMENT OF PEARLITIC RAILWAY STEELS SUBJECTED TO FAST HEATING

*The influence of soaking and cooling rates on the final microstructure of a R260Mn pearlitic railway steel subjected to fast heating is investigated. Fast-heating experiments followed or not by soaking and cooling at different rates were performed using quenching dilatometry on railway steel specimens obtained from the rail head. Additional cyclic heating and quenching experiments were done to investigate the evolution of the microstructure during thermal cycling, which is relevant for railway applications. The final microstructure is characterized via microhardness measurements, optical microscopy, and scanning electron microscopy. The microstructural features are distinguished and the influence of each condition is detailed. The study allows the construction of transformation diagrams during cooling after fast heating. Furthermore, a comparison between the final microstructures obtained in controlled laboratory conditions and field White Etching Layers is presented. The obtained results can serve as a guideline for future reproduction of White Etching Layers in laboratory conditions and interpretation of field conditions.*

---

This chapter is based on:

- V. Mattos Ferreira, M.G. Mecozzi, R.H. Petrov, J. Sietsma, "Microstructure development of pearlitic railway steels subjected to fast heating", *Materials Design*, 2022, vol.221, 110989.

## 2.1. INTRODUCTION

For many years, railway transportation has been one of the main forms of passenger and freight transportation around the world. The main advantages of this type of transportation lie in its ability to handle large passenger and freight flows, low cost, and congestion-free traffic. Besides that, its carbon emission is lower than other types of inland transportation, especially when combined with clean energy sources. This makes it attractive to many global societies that face a constant growth of urban areas and are searching for cleaner transportation alternatives. Therefore, investments in railway infrastructure and services are important for more sustainable communities.

A key component of the railway infrastructure is the steel railway track, which requires regular maintenance and track replacement. Unexpected maintenance leads to undesirable traffic interruptions which decrease the reliability of the system and leads to additional costs. For the past years, researchers have been investigating different aspects of railway systems such as steel microstructure, contact loadings, and failure mechanisms [9, 10, 14, 52, 53]. Their aim was to get insight the complex phenomena that occur during wheel/rail contact. Although these studies have led to great findings, the comprehension of these mechanisms is still incomplete.

It is known that railway tracks are subjected to two main damage mechanisms: rolling contact fatigue and wear [17, 54]. These mechanisms cause degradation of the rail geometry profile as well as deterioration of the material properties. For the past years, many studies have focused on determining the microstructural essence of damage development in railway tracks. It was found that repeated wheel/rail contacts induce microstructural changes at the rail surface [31, 42, 55]. Two different layers have been observed at the rail surface: White Etching Layer (WEL) and Brown Etching Layer (BEL), named due to their white and brownish contrast in the optical microscope after etching with 2% Nital (2%  $\text{HNO}_3$  in ethanol). These layers are associated with preferential sites for crack nucleation and propagation due to their brittle nature and the interface with the pearlitic base material. For this reason, more insight into the mechanism that leads to microstructural evolution at the surface of rails is necessary for its prevention and consequent increase of the rails' service life and safety.

There are two main theories suggested to explain the formation of WEL and BEL. The first theory claims that these layers are formed due to severe plastic deformation during wheel and rail contact which induces cementite dissolution and grain refinement at the railway surface [44, 46]. In this case, the layers are considered to be composed of carbon-supersaturated nanocrystalline ferrite. The second theory proposes that these layers are formed as a consequence of cyclic ultrafast heating leading to the austenitization of the surface during wheel passage [24, 41]. The temperature should in this explanation be high enough to promote the austenitization of those regions which will be followed by fast cooling, forming a nanocrystalline martensitic structure. Evidence for the second theory lies in the fact that retained austenite and small fractions of cementite can be observed in such layers which can only occur if at least partial austenitization takes place [37, 38]. Additionally, computer simulations have confirmed the possibility of surface heating above austenitization temperature during the wheel and rail contact [23, 35, 37]. However, some researchers are hesitant to accept that the surface can be heated to high temperatures of around 800 °C or more in milliseconds during wheel/rail contact. Although these two hypotheses were suggested, none is fully accepted.

Reproducing the exact loading conditions as on the actual railway in a laboratory is not possible at the moment. Also, the formation of these layers in the field takes place in many cycles and these types of experiments are not possible. An attempt to measure the temperature rise during wheel contact could be an option but currently, existing devices are not able to detect such a rise in temperature in milliseconds at the location where wheel/rail contact occurs. This makes it harder to reach an agreement on which theory is more realistic. As the exact conditions are not reproducible, a good approach is to get insight the behavior of railway steel when subjected to fast heating to determine whether WEL can be formed only due to rapid heating and cooling, which is the main goal of this study.

This chapter focuses on the microstructural evolution of a commonly used railway steel grade (R260Mn) when subjected to several heat treatments with fast heating. This allows for a comparison of the microstructural characteristics of field-formed layers with those simulated under controlled laboratory conditions.

Additionally, the present study aims to provide insight into the behavior of the present steel grade to serve as a guideline for getting insight on WEL and BEL formation. To do this, samples from an actual railway track were subjected to fast heating at  $200\text{ }^{\circ}\text{C}\text{s}^{-1}$  up to  $900\text{ }^{\circ}\text{C}$ . Although in practice heating rates may be higher, using this heating rate provides insight into the phase transformation behavior of R260Mn steel grade when subjected to fast heating. After heating, two routes were applied: (a) soaking for 5 minutes at  $900\text{ }^{\circ}\text{C}$  prior to cooling with different cooling rates or (b) cooling immediately after reaching  $900\text{ }^{\circ}\text{C}$  with different cooling rates.

The soaking allows the understanding of the influence of prior-austenite grain structure and homogenization of carbon in the final microstructure formed, which can also take place during repeated wheel passages in in-field railway steel. As railway steels undergo multiple cycles while in operation, another experiment was conducted to better determine the impact of cyclic heating and cooling on the behavior of these steels. For this, a sample was subjected to 10 cycles of fast heating and quenching, without soaking at high temperatures. Instead of precisely replicating the wheel and rail circumstances, the main objective of the cycling experiment is to gain information on its effect on the phase transformation behavior of railway steels.

The first part of this chapter focuses on the microstructural features found for each testing condition. As a consequence, a Continuous Cooling Transformation (CCT) diagram for R260Mn railway steels subjected to rapid heating was created. In the second part, the effect of cyclic heating on the microstructural aspects of the rails is presented along with a comparison to a WEL formed after repeated cycles of wheel/rail contact in field conditions. The combination of these findings can be used as a reference for steel manufacturers and researchers interested in reproducing WEL and BEL in laboratory conditions and a better understanding of field circumstances.

## 2.2. MATERIAL AND METHODS

### 2.2.1. MATERIAL

The material selected for this study is the R260Mn railway steel grade provided by DekraRail, Utrecht, the Netherlands. The chemical composition of the as-received material is shown in Table 2.1. The initial microstructure consists of pearlite (89% ferrite and 11% cementite) with average hardness and interlamellar spacing of 292 HV and 150 nm, respectively, see

Figure 2.1a. The material also contains 1.7% of pro-eutectoid ferrite decorating the prior-austenite grain boundaries. Furthermore, X-Ray Diffraction analysis did not detect the presence of retained austenite in the as-received material.

The equilibrium transformation temperature range of austenite formation was calculated using the software Thermo-Calc version 2021b with TCFE11 database. Figure 2.1b shows the mole fractions of the phases in equilibrium as a function of temperature for R260Mn steel. These calculations provide insight into the annealing temperature for dilatometry measurements. It can be seen that the austenitic transformation is complete at a temperature ( $A_3$ ) equal to 730 °C.

Table 2.1: Chemical composition (in wt.%) of as-received R260Mn steel

Element	C	Mn	Si	Cr	P	S	V
wt.%	0.64	1.40	0.29	0.03	0.01	0.01	0.001

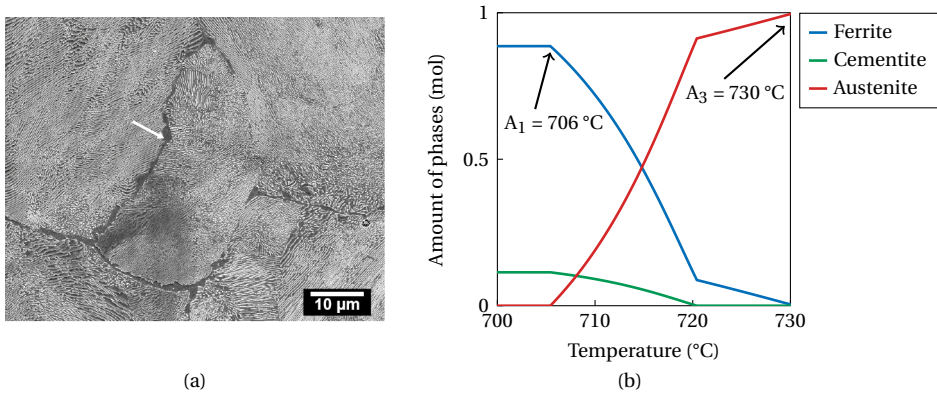


Figure 2.1: (a) Scanning electron microscopy image of the as-received R260Mn railway steel evidencing the pearlitic microstructure with the white arrow indicating pro-eutectoid ferrite at the grain boundaries and (b) Equilibrium transformation diagram of R260Mn steel calculated with Thermo-Calc software.

### 2.2.2. METHODS

A DIL805 Bähr Dilatometer was used to perform fast heating and cooling in R260Mn steel. Dilatometry allows tracking of phase transformations by measuring the change in length of the specimen throughout the heat treatment. In this study, flat dilatometry samples with 10 mm length, 4 mm width, and 1.5 mm thickness were cut from the rail head of the R260Mn steel with the length coinciding with the running direction of the rails. Two thermocouples were used in order to keep track of possible temperature gradients which can affect the final result interpretation. These thermocouples have been welded to the specimen's surface at the middle (TC1) and edge (TC2) of its length.

In order to achieve a fully austenitic microstructure that will transform into martensite during fast cooling, the annealing temperature must be above the  $A_3$  temperature as calculated by Thermo-Calc software. For this reason, the chosen annealing temperature for all heat treatments was 900 °C. This temperature is distinctly higher than the equilibrium

value, which accounts for shifts in  $A_1$  and  $A_3$  temperatures due to ultrafast heating.

A graphical representation of the heat treatments is depicted in Figure 2.2. Each specimen was heated at  $200\text{ }^\circ\text{C s}^{-1}$  up to  $900\text{ }^\circ\text{C}$ . The specimens were then cooled at different controlled cooling rates ( $0.1$ ,  $1$ ,  $10\text{ }^\circ\text{C s}^{-1}$ ) and quenched, either directly after heating (D) or after soaking at  $900\text{ }^\circ\text{C}$  for 5 minutes (S). The 5 minutes of soaking at high temperatures allow austenite grain growth and possible element homogenization in austenite. As a result, the effect of different initial austenite conditions on the phase transformation and final microstructure can be investigated. Helium atmosphere was used during cooling in all experiments except for those with cooling rate  $0.1\text{ }^\circ\text{C s}^{-1}$ , which were cooled under vacuum. The specimen identification has been done in the following manner:  $A_z$  with A being the type of heat treatment (D or S) and z the cooling rate value ( $0.1$ ,  $1$ ,  $10$  or quench). In addition, a cyclic heat treatment was performed to analyze the response of the studied material when subjected to thermal cycling. For these experiments, the samples were heated with  $200\text{ }^\circ\text{C s}^{-1}$  up to  $900\text{ }^\circ\text{C}$  and immediately quenched for a total of ten cycles.

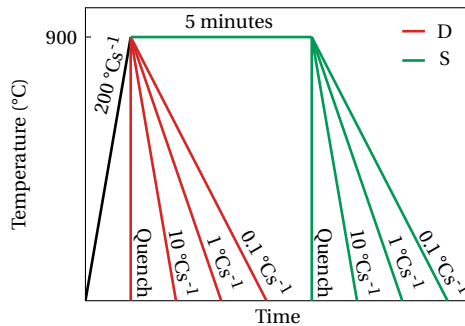


Figure 2.2: Graphical representation detailing the heat treatments performed using dilatometry. Heat treatments D consist of fast heating at  $200\text{ }^\circ\text{C s}^{-1}$  up to  $900\text{ }^\circ\text{C}$  and direct cooling with different cooling rates. Heat treatments S account for the same fast heating stage followed by intermediate soaking for 5 min at  $900\text{ }^\circ\text{C}$  before cooling with different cooling rates.

After the heat treatment, dilation curves were plotted and the fractions of transformation products formed were calculated using the lever rule with respect to BCC and FCC linear expansion curves following the method described in ref. [56]. The retained austenite fractions obtained via XRD measurements were used to calibrate the BCC expansion curves in terms of the phase fractions. The determination of the transformation-start temperatures was done by detecting the temperature at which approximately 2% of the newly-formed structural constituent is obtained.

The surface of the samples at which the thermocouples were welded was then ground and polished up to  $1\text{ }\mu\text{m}$  diamond paste using standard metallographic techniques. X-Ray diffraction (XRD) was carried out in a Bruker D8 Discover diffractometer with a Eiger-2 500k 2D-detector to obtain the phase fractions at room temperature. The  $2\theta$  scan was performed using  $\text{Cu-K}\alpha$  radiation in the angular range from  $30^\circ$  to  $150^\circ 2\theta$  and a step size of  $0.040^\circ 2\theta$ . Vickers microhardness measurements were done on the as-polished samples using a Durascan 70 (Struers) hardness tester by applying a load of  $0.1\text{ kgf}$  for  $10\text{ s}$ . The procedure was followed by etching with Nital 2% for  $10\text{ s}$  to reveal the microstructures, which were observed in a Keyence VHX 6000 light optical microscope. Higher magnification micrographs

were obtained with a JEOL JSM-6500F scanning electron microscope using a 15 kV accelerating voltage, 10 mm working distance and secondary electron imaging detection mode. Electron Probe Micro Analysis (EPMA) was performed with a JEOL JXA 8900R microprobe using an electron beam with energy of 10 keV and beam current of 100 nA employing Wavelength Dispersive Spectrometry (WDS). The points of analysis were located along two 500  $\mu\text{m}$  long lines with points 2  $\mu\text{m}$  apart and involved the elements C, Si, Cr and Mn determining the Fe concentration by difference.

Electron Backscatter Diffraction (EBSD) patterns were obtained using a FEI Quanta 450 Scanning Electron Microscope equipped with a Field Emission Gun (FEG-SEM) through the OIM Data Collection software. The analysis was performed with an acceleration voltage of 20kV, spot size of 5, working distance of 16 mm, tilt angle of 70°, and step size of 20 nm. The EBSD data was then post-processed with TSL OIM Analysis 6.0 software. The cleaning procedure consisted of: 1-grain confidence index (CI) standardization with a tolerance angle of 5° and minimum grain size of 6 pixels and considering grains formed by multiple pixel rows, 2-neighbor-orientation correlation with tolerance angle of 5° and minimum confidence index of 0.1, 3- down-filtering criterion of confidence index higher than 0.1 to reduce pixels poorly indexed.

## 2.3. RESULTS AND DISCUSSION

### 2.3.1. HEATING

Figure 2.3a shows the dilatometry curves obtained during the heating stage of the heat treatment for each specimen analyzed in this work. As only austenite formation took place during heating, the graph is enlarged in this area for a detailed analysis. Oscillations of the temperature profile were present prior to austenite formation for many samples, which affect the dilatometry curves, see Figure 2.3a. These oscillations are due to the difficulty of the equipment to adjust the power input during very fast heating. To overcome this, the control parameters of the dilatometer equipment have been adjusted to obtain a smoother curve as for specimen D<sub>10</sub>, highlighted in black. As the oscillations did not affect the heating profiles which showed high reproducibility, the specimens were still considered valid in this work. The dilatometry curves presented in Figure 2.3a allow to extract information regarding the kinetics and the temperature range for austenite formation.

The experimental results presented in Figure 2.3a show that a deviation from linearity starts at approximately 736 °C. Since austenite has a more compact lattice than ferrite and cementite, a contraction is expected to occur during pearlite to austenite transformation, leading to a decrease in the change in length versus temperature. However, an expansion instead of a contraction is observed at the beginning of the austenitic transformation, followed by the expected contraction. Interrupted heating experiments were performed up to 751 °C to determine whether austenite forms at the onset of the expansion. As can be seen in the inset of Figure 2.3a, small fractions of austenite (martensite after fast cooling) are formed at temperatures up to 751 °C, confirming that austenite nucleates at the very start of the peak.

The same expansion peak before austenite formation is observed in the sample subjected to cyclic heating and quenching. Figure 2.3b presents the heating dilatometry curves obtained for each cycle. A clear distinction between the first (black line) and the following cycles is noted. The first cycle is characterized by an expansion of the sample with a maxi-

mum at 775 °C during pearlite to austenite transformation. When the sample is reheated in the second cycle, fluctuations are observed in the dilatometry curve between 200 and 500 °C, which are due to the tempering of the martensite formed at the end of the first cycle after quenching. During tempering, carbide precipitation is expected to occur, reducing the carbon content of martensite which leads to a slight contraction of the sample [57]. At approximately 735 °C, the austenite starts nucleating and growing in the tempered martensite. In this case, however, the magnitude of the expansion peak during the martensite to austenite transformation is substantially smaller than for the pearlitic initial microstructure.

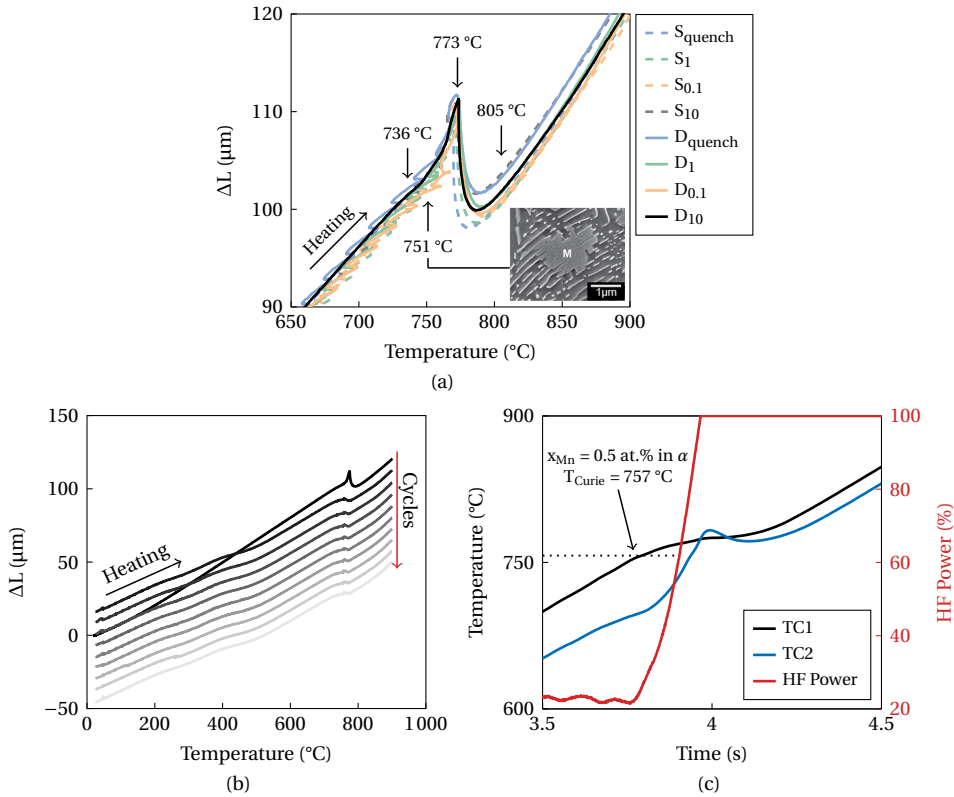


Figure 2.3: (a) Heating stage of dilatometry curves for all specimens analyzed in this work with a focus on the intercritical temperature range where austenite formation takes place. Additionally, the SEM micrograph shows small patches of martensite (austenite at high temperatures) growing in the pearlitic matrix when the sample was heated up to 751 °C followed by quench. (b) The heating stages of sample  $D_{\text{cyclic}}$  with increasing order of the cycles is indicated with a red arrow. (c) Temperature and HF Power as a function of time for the first heating cycle of  $D_{\text{cyclic}}$ .

The actual  $A_{c1}$  and  $A_{c3}$  acquired from dilatometry curves for a heating rate of  $200 \text{ }^{\circ}\text{C}\text{s}^{-1}$  are 736 °C and 805 °C, respectively. These values are higher than the equilibrium  $A_1$  and  $A_3$  calculated by Thermo-Calc, see Figure 2.1, since the experiments were conducted in non-equilibrium conditions with a heating rate of  $200 \text{ }^{\circ}\text{C}\text{s}^{-1}$ . Finally, all experiments were carried out up to 900 °C which guarantees complete austenitization.

Additional investigation was done to determine the nature of the dilatation peak ob-

served for all samples. Figure 2.3c shows the temperatures (TC1 and TC2) and power supply necessary to maintain the heating rate at  $200\text{ }^{\circ}\text{C}\text{s}^{-1}$  as a function of time for the first heating stage of the  $D_{\text{cyclic}}$  sample. It is important to note that the power is adjusted according to the temperature profile registered at TC1 (middle of the sample). As the dilatometer works based on induction heating of the sample, the magnetic properties of the material can affect the power required for heating. In this case, the Curie Temperature ( $T_{\text{Curie}}$ ) of the ferrite matrix in pearlite (initial microstructure in the first cycle) can be estimated based on the Mn content of ferrite (0.5 at.%) [24] and corresponds to  $757\text{ }^{\circ}\text{C}$  (Figure 2.3c). This temperature is similar to the start of austenite formation, at approximately  $751\text{ }^{\circ}\text{C}$ . After TC1 crosses the  $T_{\text{Curie}}$ , a sharp increase of the power is required to maintain the desired heating rate as the middle portion of the sample is now paramagnetic. Since at this point, the edge of the sample (TC2) is at about  $60\text{ }^{\circ}\text{C}$  below this temperature, the sharp increase of the power causes a rise of the heating rate in this still ferromagnetic region, with a consequent increase of the dilatation signal, corresponding to the abnormal peak observed in the first heating cycle.

In the subsequent cycles, however, the initial microstructure is tempered martensite instead of pearlite (ferrite matrix). The martensitic structure is assumed to have the same overall Mn content as the alloy composition (2 at.%) which leads to a decrease of  $T_{\text{Curie}}$  to approximately  $735\text{ }^{\circ}\text{C}$ . In this case, the start of austenite formation occurs after crossing  $T_{\text{Curie}}$ , and a two-step increase of power is observed with a less pronounced dilatation peak, Figure 2.3b. For this reason, it can be concluded that the dilation peak is related to the gradient temperature of the sample which is evidently due to the fast heating imposed. This also leads to a microstructural gradient from the middle to the edge of the sample. For this reason, we only consider the analysis of the middle portion of the sample.

### 2.3.2. PRIOR-AUSTENITE GRAIN SIZE

It is known that high-temperature soaking and cyclic thermal treatments can alter the prior-austenite grain (PAG) structure [58, 59, 60] and, as a result, the final microstructure. For this reason, an investigation of the PAG structure is needed in order to determine the microstructures after the heat treatment.

In this section, the EBSD scans obtained for samples subjected to slow cooling ( $0.1\text{ }^{\circ}\text{C}\text{s}^{-1}$  and  $1\text{ }^{\circ}\text{C}\text{s}^{-1}$ ), fast cooling (quench), and cyclic thermal treatment ( $D_{\text{cyclic}}$ ) have been used to reconstruct the PAG using EDAX's OIM Analysis<sup>®</sup> v8.6 software. These samples were chosen based on the time between the start of cooling and the beginning of pearlite formation which can also play a role in PAG growth. For example, samples with slow cooling are subjected to temperatures above the pearlite formation during cooling for approximately 50 minutes at  $0.1\text{ }^{\circ}\text{C}\text{s}^{-1}$  and 4 minutes at  $1\text{ }^{\circ}\text{C}\text{s}^{-1}$ . This can lead to PAG growth due to prolonged time at high temperatures. On the other hand, samples subjected to intermediate cooling are assumed to have PAG equal to the ones of quenched samples as they are exposed to high temperatures for a short period during cooling.

As the reconstruction of PAG is only possible from martensite, additional interrupted heat treatments were done for slow-cooling samples. These heat treatments consisted of heating the samples with  $200\text{ }^{\circ}\text{C}\text{s}^{-1}$  up to  $900\text{ }^{\circ}\text{C}$  with and without soaking for 5 minutes, followed by slow cooling ( $0.1\text{ }^{\circ}\text{C}\text{s}^{-1}$  and  $1\text{ }^{\circ}\text{C}\text{s}^{-1}$ ) to  $710\text{ }^{\circ}\text{C}$  and subsequent quenching to get a final martensitic microstructure. The temperature choice was based on the dilatometry curves for slow cooling, as will be discussed in section 2.3.3. The temperature of  $710\text{ }^{\circ}\text{C}$  is right before the decomposition of austenite into ferrite and pearlite in all cases, which gives



a good estimation of the PAG development in the cooling stage.

The PAG reconstruction has been performed according to the Nishiyama-Wasserman (N-W) orientation relationships between martensite and parent austenite grains. Figure 2.4 shows the reconstructed PAG for samples  $D_{\text{quench}}$ ,  $D_{\text{cyclic}}$ ,  $S_{\text{quench}}$  and  $S_{0.1}$ . As can be seen, grains with an elongated shape are observed in samples with smaller PAG size ( $D_{\text{quench}}$  and  $D_{\text{cyclic}}$ ). On the contrary, soaking at high temperatures leads to not only an increase in PAG size but also grains with a polygonal morphology. This is expected as the structure tends to reduce its internal energy by reducing the grain boundary area.

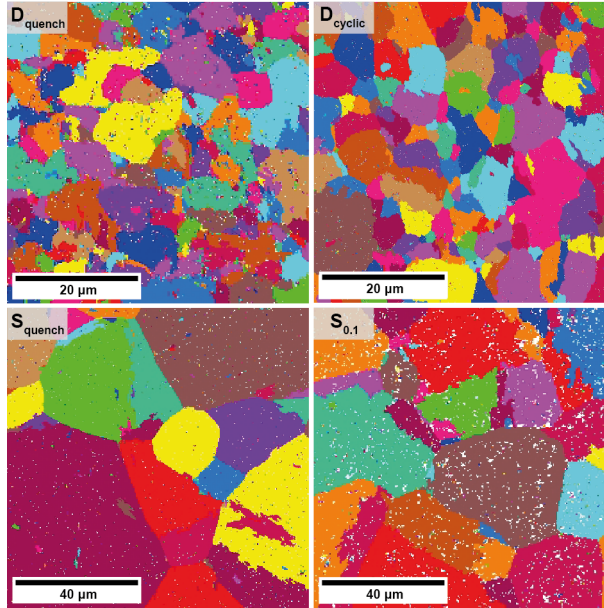


Figure 2.4: Color coded unique grain color maps representing the reconstruction of PAGs from martensite variants according to Nishiyama-Wasserman (N-W) orientation relationship of samples  $D_{\text{quench}}$ ,  $D_{\text{cyclic}}$ ,  $S_{\text{quench}}$  and  $S_{0.1}$  using EDAX-TSL OIM Data analyses v8.3 software.

Table 2.2 presents the average reconstructed PAG size for each sample using N-W orientation relationship. Samples  $D_{\text{quench}}$  and  $D_{\text{cyclic}}$  show a similar average PAG of around  $6 \mu\text{m}$  which is considerably smaller than for the other analyzed samples. The smaller grains are attributed to the short time for grain growth as each heating-cooling cycle takes approximately 9 seconds. The similarities between these two samples also suggest that 10 cycles do not provide further grain refinement of the PAG.

On the other hand, a significantly higher PAG size is obtained for samples subjected to soaking and/or prolonged cooling stages. This increase is observed also for the width of the grain size distribution suggesting a bimodal distribution of PAG size. An additional observation is that the 5 minutes soaking time is sufficient for reaching a maximum growth of PAG. This is supported by the fact that  $S_{0.1}$ , exposed to high temperature for an extended period after soaking, has a PAG size similar to  $S_{\text{quench}}$ .

Table 2.2: Quantification of the PAG size distribution

Sample	Average prior-austenite grain size ( $\mu\text{m}$ )	Distribution width ( $\mu\text{m}$ )
D <sub>0.1</sub>	28.1	15.1
D <sub>1</sub>	20.8	11.9
D <sub>quench</sub>	6.4	3.7
D <sub>cyclic</sub>	6.5	3.3
S <sub>0.1</sub>	29.2	12.4
S <sub>1</sub>	35.4	21.2
S <sub>quench</sub>	34.6	17.6

### 2.3.3. SLOW COOLING ( $0.1$ AND $1\text{ }^{\circ}\text{C}\text{s}^{-1}$ )

Figure 2.5a presents the change in length as a function of temperature for heat treatments D (direct cooling) and S (soaking) during cooling with cooling rates of  $0.1$  and  $1\text{ }^{\circ}\text{C}\text{s}^{-1}$ . These curves allow the detection of phase transformations which are characterized by a change in the slope of the dilatometry curve with respect to the FCC contraction curve (dotted gray line). The XRD results show that these cooling rates lead to a mix of BCC iron plus cementite, similar to the as-received material (89% BCC + 11% Cementite), see Table 2.3.

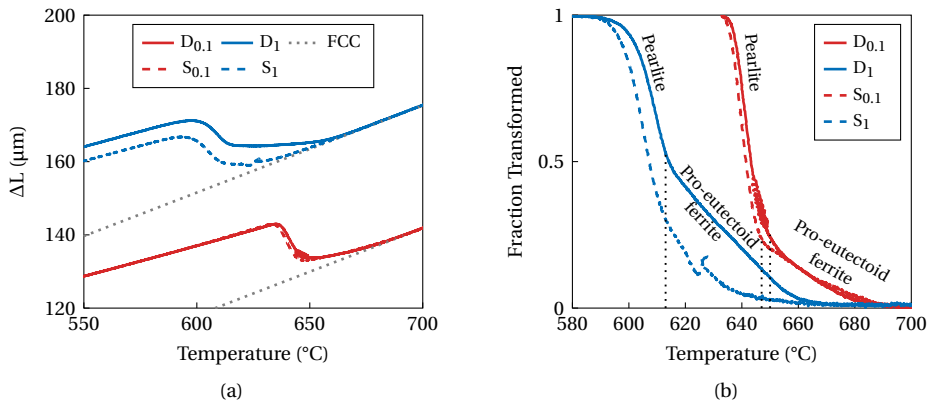


Figure 2.5: (a) Change in length as a function of temperature obtained during cooling in dilatometry tests for specimens subjected to both heat treatments (D - solid line and S - dashed line) with low cooling rates ( $0.1\text{ }^{\circ}\text{C}\text{s}^{-1}$  - red and  $1\text{ }^{\circ}\text{C}\text{s}^{-1}$  - blue) together with theoretical FCC expansion curves used to calculate the phase fractions. (b) Transformation product fractions calculated for each cooling rate.

During slow cooling, a phase transformation is observed in the temperature range of  $575$  to  $675\text{ }^{\circ}\text{C}$ . The analysis of the dilatation curves suggests a two-step transformation with difference in the kinetics of the transformation, see Figure 2.5b. At first, the pro-eutectoid ferrite starts forming at the prior-austenite grain boundaries at  $680\text{ }^{\circ}\text{C}$  for  $0.1\text{ }^{\circ}\text{C}\text{s}^{-1}$  and at  $660\text{ }^{\circ}\text{C}$  for  $1\text{ }^{\circ}\text{C}\text{s}^{-1}$ . The remaining austenite then transforms into pearlite from  $650\text{ }^{\circ}\text{C}$  and  $610\text{ }^{\circ}\text{C}$  for  $0.1\text{ }^{\circ}\text{C}\text{s}^{-1}$  and  $1\text{ }^{\circ}\text{C}\text{s}^{-1}$ , respectively. The SEM microscopy (Figure 2.6) confirms the microstructure to be predominantly pearlitic, with the presence of pro-eutectoid ferrite at the grain boundaries of the prior austenite.

Samples with a cooling rate of  $0.1\text{ }^{\circ}\text{C}\text{s}^{-1}$  (D<sub>0.1</sub> and S<sub>0.1</sub>) show regions of partial or complete spheroidization of the cementite lamellae, see Figure 2.6. This spheroidization occurs

as a consequence of prolonged cooling times after pearlite formation which allows cementite to reconfigure into a more stable morphology aiming at reducing the interfacial energy of the system [61].

Table 2.3: Phase fractions obtained via XRD for samples subjected to heat treatments D (direct cooling) and S (with soaking) with 0.1 and 1 °Cs<sup>-1</sup>

Structure	Phase Fraction ± 1 %			
	D <sub>0.1</sub>	S <sub>0.1</sub>	D <sub>1</sub>	S <sub>1</sub>
BCC	90	91	92	91
Cementite	10	9	8	9
FCC	-	-	-	-

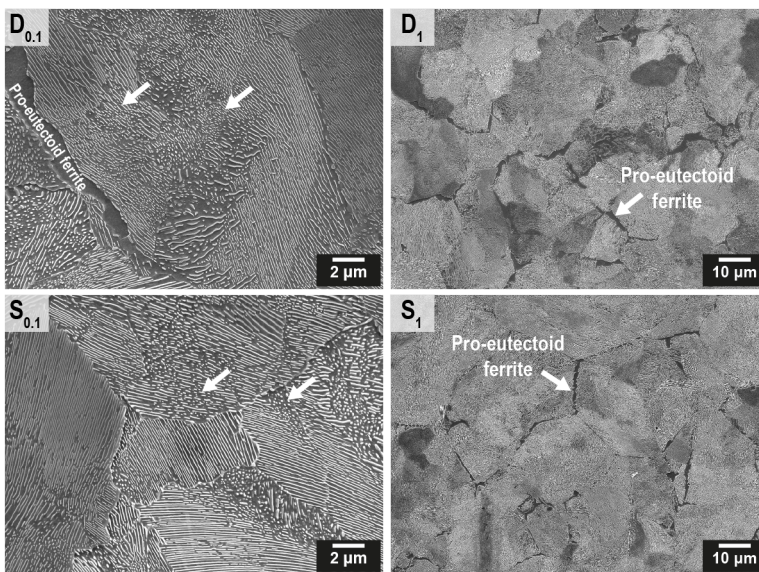


Figure 2.6: SEM images showing the differences between direct cooling (D-samples) and soaking (S-samples) for low cooling rates. Two different magnifications are used for 0.1 and 1 °Cs<sup>-1</sup> samples to highlight the pearlite spheroidization in the former and the pro-eutectoid ferrite size and morphology in the latter.

At the cooling rate of 1 °Cs<sup>-1</sup>, the delay of the start of pearlite formation causes an increase of pro-eutectoid ferrite fraction decorating the austenite grain boundaries when compared to the sample cooled at 0.1 °Cs<sup>-1</sup>. Due to the smaller austenite grain size of D samples than S samples, the pro-eutectoid ferrite fraction is expected to be higher in the former. Unlike the samples subjected to 0.1 °Cs<sup>-1</sup>, no cementite spheroidization is observed in these two treatments which is related to the lack of time during cooling for the cementite to reach a morphology with lower energy.

Cooling rates of 1 °Cs<sup>-1</sup> lead to the formation of more pro-eutectoid ferrite when compared to the samples subjected to 0.1 °Cs<sup>-1</sup>, see Figure 2.5b, which can be explained by the difference in the PAG size. When cooled with very low cooling rates, such as 0.1 °Cs<sup>-1</sup>, the material is exposed to high temperatures for an extended period, resulting in larger PAG

and lower nucleation site density for pro-eutectoid ferrite nucleation. As a result, less pro-eutectoid ferrite is present in the final microstructure, which is also observed in Figure 2.5b.

The pro-eutectoid fraction was obtained via SEM image analysis using ImageJ software for samples with a cooling rate of  $1\text{ }^{\circ}\text{C}\text{s}^{-1}$ . The pro-eutectoid fraction is higher in sample  $D_1$  ( $3.5 \pm 0.5\%$ ) than in sample  $S_1$  ( $2.2 \pm 0.3\%$ ). Not only does sample  $D_1$  have a higher fraction of pro-eutectoid ferrite but also its morphology differs from  $S_1$ , see Figure 2.6. While a relatively coarse pro-eutectoid ferrite is present for specimen  $D_1$ , a distinctly refined morphology is achieved after soaking for 5 minutes.

### 2.3.4. INTERMEDIATE COOLING ( $10\text{ }^{\circ}\text{C}\text{s}^{-1}$ )

A different behavior is observed when the material is cooled with  $10\text{ }^{\circ}\text{C}\text{s}^{-1}$ . The deviation from linearity occurs in both D and S samples at about  $650\text{ }^{\circ}\text{C}$ , indicating the start of austenite decomposition, which progresses in three stages irrespective of soaking, as shown in Figure 2.7. The first stage takes place between  $550$  and  $650\text{ }^{\circ}\text{C}$  and it is related to the pearlite formation. The pearlite formation does not account for two steps of transformation, as observed for samples with slow cooling, implying the absence or only a very small fraction of pro-eutectoid ferrite. The second stage is between  $550$  and  $350\text{ }^{\circ}\text{C}$ , corresponding to bainite formation. The last stage, where the remaining austenite transforms into martensite, is at temperatures below  $250\text{ }^{\circ}\text{C}$ .

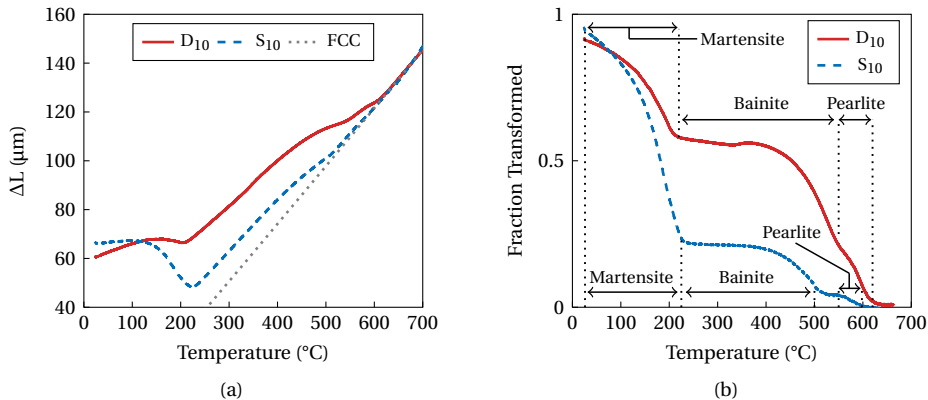


Figure 2.7: (a) Change in length as a function of temperature curves obtained during cooling in dilatometry tests for specimens subjected to both heat treatments (D - solid line and S - dashed line) with intermediate cooling ( $10\text{ }^{\circ}\text{C}\text{s}^{-1}$ ) together with theoretical FCC expansion curves used to calculate the transformed fractions. (b) Fractions of the microstructural constituents were calculated for each sample.

Table 2.4: Phase fractions obtained via XRD for samples subjected to heat treatments D (direct cooling) and S (with soaking) with  $10\text{ }^{\circ}\text{C}\text{s}^{-1}$

Structure	Phase Fraction $\pm 1\%$	
	$D_{10}$	$S_{10}$
BCC	87	93
Cementite	4	5
FCC	9	2

However, the transformation is not completed and a small fraction of retained austenite remains in the final microstructure, see Table 2.4. The main difference between the two samples lies in the fractions of the microstructural constituents. A lower fraction of pearlite and bainite and consequently a higher fraction of martensite is seen (from the dilatometry curve analysis) to be present in the final microstructure of  $S_{10}$  when compared with  $D_{10}$ .

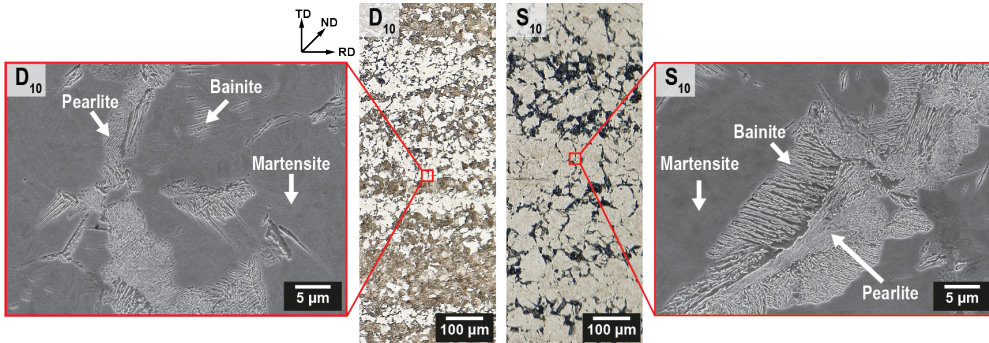


Figure 2.8: OM and SEM images of samples  $D_{10}$  and  $S_{10}$  revealing the banded structure composed of martensite (white contrast) and a mix of bainite and pearlite (dark contrast). The orientation is defined as RD - rolling direction, ND - normal direction (perpendicular to rail surface), and TD - transverse direction.

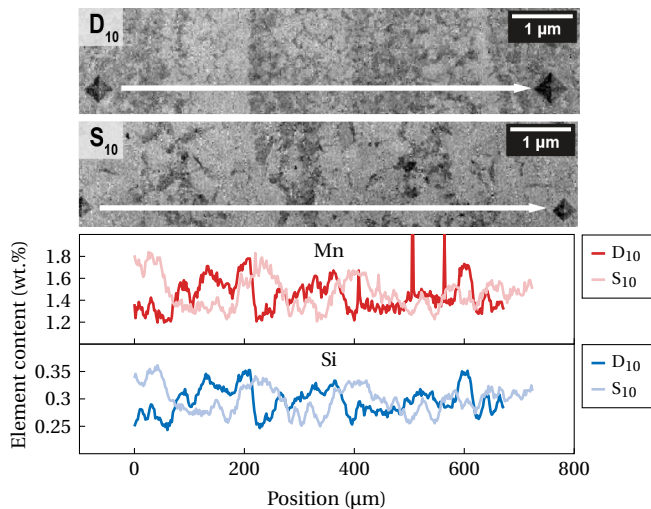


Figure 2.9: EPMA analysis of  $D_{10}$  and  $S_{10}$  showing Mn (red) and Si (blue) distribution along the banded structure.

After the heat treatment, the analysis of the microstructure was performed using Optical Microscopy (OM) to investigate the homogeneity of the phases in low magnification. Figure 2.8 shows the OM images of samples  $D_{10}$  and  $S_{10}$ , together with high magnification SEM images of specific regions. The microstructure consists of a mixture of martensite, bainite, pearlite, and retained austenite. These microstructural constituents, however, are not distributed uniformly, but in alternating bands of bainite/pearlite (OM dark con-

trast) and martensite (OM white contrast). SEM micrographs allow better analysis of the microstructure of the dark-contrast regions which consist of a mix of bainite and pearlite. As expected from the transformed fraction curve, sample D<sub>10</sub> contains a higher fraction of pearlite/bainite bands while sample S<sub>10</sub> has a higher fraction of martensitic bands.

Figure 2.9 displays the EPMA results for samples D<sub>10</sub> and S<sub>10</sub> which was done to determine the segregation of the elements in the bands. The measurement was performed along a line of approximately 700  $\mu\text{m}$  located in the vicinity of thermocouple TC1. Although these experiments were carried out aiming at the detection of C, Mn, Si, and Cr, no segregation of C and Cr was observed. On the other hand, one can see that in both cases, martensitic regions (white contrast) account for positive segregation of Mn and Si, while pearlitic/bainitic regions (dark contrast) are locations of negative segregation of these elements.

### 2.3.5. FAST COOLING (QUENCH)

For the fast cooling experiments, the actual cooling rates were measured in the temperature range of 800  $^{\circ}\text{C}$  and 500  $^{\circ}\text{C}$  after the heat treatment was performed. The approximate cooling rates for samples D<sub>quench</sub> and S<sub>quench</sub> are 347  $^{\circ}\text{C}\text{s}^{-1}$  and 365  $^{\circ}\text{C}\text{s}^{-1}$ , respectively. During fast cooling, no phase transformation takes place at higher temperatures, see Figure 2.10a. According to the dilatometry curves, a final martensitic microstructure with a small fraction of retained austenite is formed. XRD measurements show that a similar content of retained austenite is obtained for both samples: 11% for D<sub>quench</sub> and 9% for S<sub>quench</sub>, with no cementite detected.

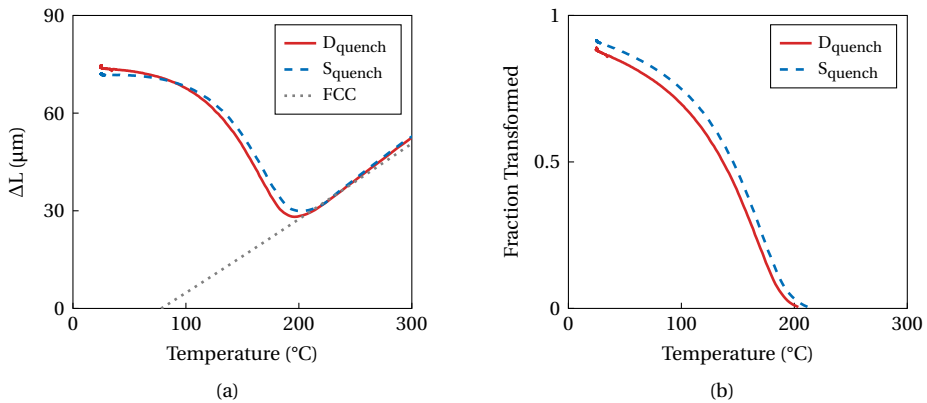


Figure 2.10: (a) Change in length as a function of temperature curves obtained during dilatometry tests for specimens subjected to both heat treatments (D - red solid line and S - blue dashed line) with high cooling rates together with theoretical FCC expansion curves used to calculate the phase fractions. (b) Phase fraction calculated for each condition.

Figure 2.11 depicts the SEM micrographs of quenched samples. As expected, the initial pearlite, after transformation to austenite at high temperature, is completely transformed into martensite with a small fraction of retained austenite. Furthermore, regions of the so-called "ghost pearlite" are present inside martensitic areas in sample D<sub>quench</sub> as indicated by a white arrow in Figure 2.11. Those features have been previously reported in the literature [62, 63, 64, 65] as a result of high Mn concentration in austenite regions formed from cementite dissolution.

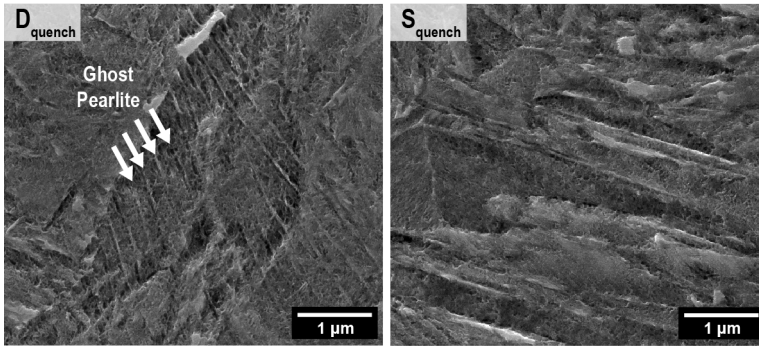


Figure 2.11: SEM images showing the differences between direct cooling (D-samples) and soaking (S-samples) for quenched samples. Ghost pearlite is indicated with white arrows.

In the absence of soaking at high temperature and due to the high heating rate, Mn, present in high concentration in the cementite lamellae, does not have time to homogenize in austenite after cementite dissolution. Martensite containing a high Mn concentration is etched differently, thus revealing what is called "ghost pearlite". On the other hand, soaking for 5 minutes at high temperatures can allow the diffusion of Mn out of cementite regions and its homogenization in austenite, leading to an absence of ghost pearlite, as observed in sample  $S_{\text{quench}}$ . This hypothesis is supported by calculating the diffusion distance of Mn in austenite after 5 minutes at 900 °C, which is expressed as

$$\lambda_{Mn} = \sqrt{2D_{Mn}^Y t} \quad (2.1)$$

where  $\lambda_{Mn}$  is the diffusion distance of Mn in austenite,  $t$  the diffusion time (5 minutes) and  $D_{Mn}^Y$  the diffusivity of Mn in austenite at 900 °C ( $3.8 \times 10^{-17} \text{ m}^2\text{s}^{-1}$ ). The latter is calculated using an activation energy ( $Q$ ) of 246420 J/mol and deriving the pre-exponential factor ( $D_0 = 3.69 \times 10^{-6} \text{ m}^2\text{s}^{-1}$ ) from data obtained with Thermo-Calc software version 2021b with TCFE11 database. The diffusion distance is approximately 152 nm, which is in the same order of magnitude as the interlamellar spacing in pearlite. This supports the theory that under these circumstances, Mn has sufficient time to diffuse and homogenize in austenite, and hence no ghost pearlite is found in soaked samples.

### 2.3.6. CYCLIC HEATING AND COOLING

In this section, the effect of cyclic heating and quenching will be discussed. The experiment aims at simulating the fast heating and cooling of the rail surface during several wheel passages under controlled laboratory conditions. Figure 2.12a shows the cooling stage of dilatometry curves obtained for each cycle. As can be seen, in each cycle the main phase transformation is the martensite formation, which starts at approximately 300 °C.

Both the heating and cooling stages of the dilatometry curve show a shift towards lower dilatation at each cycle, indicating an axial contraction of the sample. The same behavior has been previously observed in the literature [66]. The authors ascribed the sample contraction during multiple thermal cycles to chemical segregation bands parallel to the sample axis. In the study, artificially banded samples (Mn segregation) were analyzed and

the axial strain obtained during cyclic heating was associated not only with the segregation of elements in the banded structure but also with the orientation of the sample with respect to the bands. In order to determine whether the shifts observed in  $D_{\text{cyclic}}$  are related to the anisotropy of the sample, the same heat treatment was imposed on a sample cut transversely to the rolling direction of rails. In this case, not only the shifts were much smaller but they also decreased with each cycle, confirming a relationship between the dilatometric shifts and the anisotropic behavior of the sample.

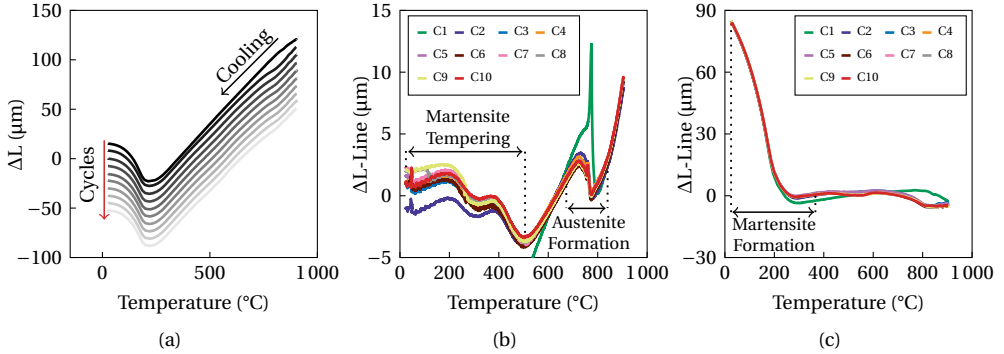


Figure 2.12: (a) Cooling portion of dilatometry curves for specimen subjected to cyclic heating and quenching. (b) Optimized heating portion of dilatometry curves not considering the axial contraction of the sample. (c) Optimized cooling portion of dilatometry curves not considering the axial contraction of the sample.

In order to capture detailed features, the scale at which the curves are depicted is greatly enlarged by subtracting the contribution of thermal expansion and contraction by calculating the length effects due to microstructural processes ( $L_m$ ) according to

$$L_m = \delta L - (\lambda_i + \alpha T) \quad (2.2)$$

in which  $\delta L$  is the original dilatation signal. The slope  $\alpha$  was chosen for both heating ( $0.10 \mu\text{mK}^{-1}$ ) and cooling ( $0.22 \mu\text{mK}^{-1}$ ) to optimise the scale. The parameter  $\lambda_i$  is chosen for each cycle  $i$  to achieve maximum coincidence of curves.

The resulting curves are shown in Figure 2.12b and c. As can be observed, the choice for  $\lambda_i$  aims at coinciding the curves in the austenite formation region in the case of the heating stage and during martensite formation during cooling. During heating, the first cycle diverges from the subsequent ones, which is expected as the initial microstructure differs (pearlite for the first cycle and martensite in all subsequent cycles).

Apart from the peak caused by the temperature gradient (see section 2.3.1), a change in the slope of the dilatation curve during the first portion of heating before austenite starts forming is also present, see Figure 2.12b. It is observed that heating of an initial pearlitic structure accounts for a higher slope than the heating of martensite during the second and subsequent cycles. The change in slope is related to the initial microstructure (pearlite or martensite) and the variation of its thermal expansion, which is in agreement with the theoretical thermal expansion curves based on [67, 68, 69]. Besides that, a slight increase in the tempering effect with the number of cycles is also observed.

The cooling curves are very well reproducible apart from a slight deviation from the linearity (expansion) at high temperatures for the first cycle, see Figure 2.12c. Further investigation is necessary to determine the exact cause of this deviation whether it is due to



ferrite or carbide precipitation or an instrumental artifact. From the second cooling cycle onwards, there is a delay in the inset of this deviation to around 800 °C. At this temperature, austenite becomes unstable (Figure 2.1), and possible precipitation of small fractions of ferrite or carbides can occur. However, in section 2.3.5, sample  $D_{\text{quench}}$  (1 cycle) did not show the presence of ferrite nor carbides when observed in SEM or XRD measurements. Additionally, XRD measurements performed after 10 cycles reveal a total of 92% of BCC and 8% of FCC with no cementite detected. Besides, all cycles show a similar martensite-start temperature which confirms that no major differences are observed during the cooling portion of the cyclic heat treatment.

An interesting factor is that all curves are very well reproducible from the second cooling cycle onwards while deviations are observed in the first heating and cooling cycle and the second heating cycle. One possible explanation is related to the decomposition of austenite and element partitioning, especially Mn, which does not occur with only one cycle. A second explanation can be the carbide morphology which can also vary from the first and subsequent cycles.

### 2.3.7. MICROHARDNESS

Figure 2.13 provides the Vickers microhardness values for each condition analyzed in this work. No significant difference in hardness from the as-received material is observed in samples  $D_{0.1}$  and  $S_{0.1}$ . This confirms that cooling at a rate of  $0.1\text{ °Cs}^{-1}$  only leads to cementite spheroidization in some pearlite colonies. On the other hand, not only is there an increase in hardness for specimens cooled with  $1\text{ °Cs}^{-1}$  when compared with  $0.1\text{ °Cs}^{-1}$ , but the hardness of sample  $S_1$  (339 HV) is slightly higher than that of sample  $D_1$  (319 HV). This difference in hardness is explained by the decreased pro-eutectoid ferrite fraction after soaking which is related to the larger PAG size as discussed in sections 2.3.2 and 2.3.3.

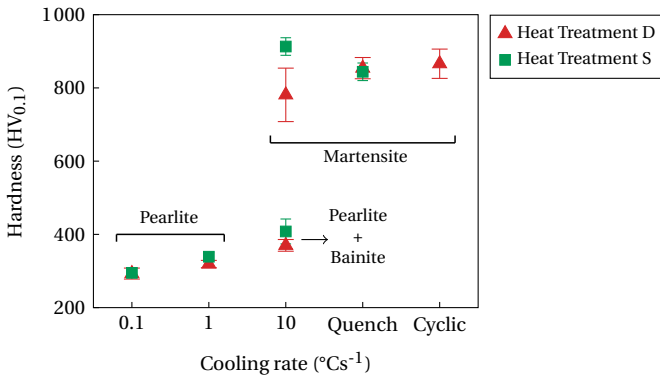


Figure 2.13: Vickers microhardness measurements of samples subjected to heat treatments D (direct cooling) and S (with soaking at high temperature). Two distinct measurements are presented for samples with cooling rates of  $10\text{ °Cs}^{-1}$  in order to differentiate the mechanical response of the banded structure.

A clear difference in hardness is observed between bands in the structure of samples cooled with  $10\text{ °Cs}^{-1}$ . As expected, the martensitic bands have a greater hardness than the combination of pearlite and bainite, regardless of the soaking. In addition, the martensitic band formed after soaking presents a much higher hardness than the one found in sample

D<sub>10</sub>. The higher standard deviation of the hardness of D<sub>10</sub> might be related to the smaller grains of martensite and a higher fraction of pearlite and bainite that can influence the local hardness. Quenching leads to martensitic structures with a hardness of approximately 850 HV, which is lower than the hardness observed for the martensitic band of sample S<sub>10</sub> but higher than sample D<sub>10</sub>. Finally, the cyclic fast heating and quenching present similar hardness as samples subjected to one cycle.

The higher hardness obtained for sample S<sub>10</sub> could be caused by carbon enrichment of martensitic bands. However, both samples cooled at 10 °C s<sup>-1</sup> show similar martensite-start temperatures, implying that strong differences in carbon content are not present. Furthermore, the enrichment of Mn and Si on martensitic bands reported in section 2.3.4 is insufficient to affect the martensite-start temperature and, as a result, the hardness of martensite significantly.

### 2.3.8. CCT DIAGRAM

Figure 2.14 shows the Continuous Cooling Transformation (CCT) diagram for R260Mn steel with two initial PAG sizes (6 μm and 35 μm) simulated with Thermo-Calc software together with the CCT diagrams obtained via analysis of the dilatometry curves. As discussed in section 2.3.2, the initial PAG size is smaller for samples subjected to heat treatment D followed by fast cooling (D<sub>quench</sub> and D<sub>10</sub>). This leads to faster rate of ferrite and pearlite formation due to a higher density of nucleation sites for these microstructural constituents.

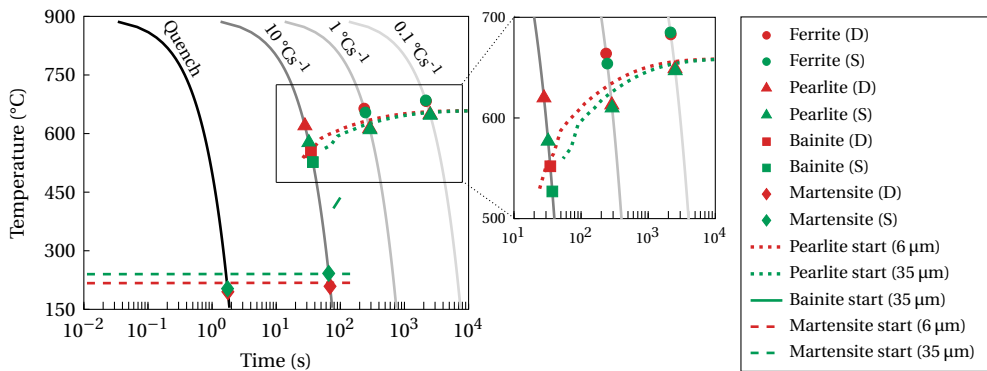


Figure 2.14: Continuous Cooling Transformation diagram obtained via Thermo-Calc software and experimentally. The calculated CCT diagram (lines) considers two initial PAG sizes: 6 μm (red) and 35 μm (green). The experimental CCT (symbols) exposes the starting temperatures of the different transformations formed after heat treatments D (red) and S (green).

The PAG effect is not evident for very low cooling rates (0.1 and 1 °C s<sup>-1</sup>), explained by the prolonged time at high temperatures during cooling which allows similar PAG growth as seen in soaked samples. On the other hand, when cooling with 10 °C s<sup>-1</sup>, a delay is observed at the start of pearlite and bainite transformations for sample S<sub>10</sub>, which is related to the lower nucleation-site density due to larger PAG. Although the simulated CCT diagram does not account for the presence of ferrite, the start temperature of pearlite transformation is consistent with the experiments.

For intermediate cooling rates, the bainitic transformation occurs for both direct-cooling and soaking samples, whereas it is expected to happen only for larger PAG in the

simulated CCT diagram. Furthermore, the bainite start transformation temperatures are higher than expected from simulations. The transformation takes place at temperatures closer to the pearlite-start temperature. The simulation considers a homogeneous material, however, segregation bands are observed while cooling at  $10\text{ }^{\circ}\text{C}\cdot\text{s}^{-1}$ . These bands have a slightly different content of Mn and Si which can affect the bainite-start temperature.

The martensitic transformation starts first for S samples with respect to D samples in both the simulated and the experimental CCT diagram. In this case, the refinement of PAG results in lower martensite-start temperatures as previously mentioned in the literature [70, 71]. However, there's no consensus regarding the exact correlation between PAG size and martensite-start temperatures in the literature.

### 2.3.9. COMPARISON WITH WEL FROM FIELD

This section compares the microstructures acquired in controlled laboratory conditions to the WEL formed during wheel/rail contact in field conditions. A detailed analysis of the WEL from a field R260Mn sample used in this work can be found in the literature [24]. For the comparison, two laboratory samples were chosen: one subjected to fast heating followed by immediate quenching ( $D_{\text{quench}}$ ) and one subjected to cyclic heating and quenching. These samples are thought to be a suitable depiction of the thermal cycle suggested by one of the WEL formation theories: rapid heating of the rail surface due to wheel contact, followed by quick cooling.

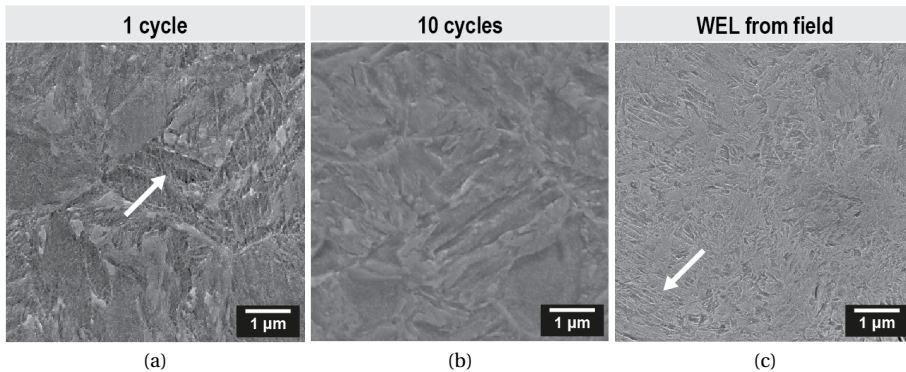


Figure 2.15: SEM images of samples subjected to (a) 1 cycle ( $D_{\text{quench}}$ ), (b) 10 cycles and (c) field WEL from a R260Mn steel. White arrows indicate the regions where ghost pearlite was observed.

Figure 2.15 presents the SEM micrographs of each sample. As previously mentioned, sample  $D_{\text{quench}}$  has a martensitic microstructure with some retained austenite. The same is observed after 10 cycles of fast heating and quenching, Figure 2.15b. However, ghost pearlite (indicated with the white arrow in Figure 2.15a) is not present after cyclic heating and quenching. That indicates that Mn is able to diffuse out of the cementite lamella regions, homogenizing in the martensitic microstructure.

If we now observe the WEL from field R260Mn steel, Figure 2.15c, similar features resembling the ghost pearlite are present. Previous atom probe tomography measurements confirmed Mn-rich zones inside of the WEL [24, 23]. This means that even after several wheel/rail contacts, Mn does not have enough time to diffuse out of prior cementite regions and homogenize in the austenite. This leads to Mn-rich locations which are etched

differently than the matrix, showing the above-mentioned, "ghost-pearlite".

However, according to the literature, the grain size of field WEL is substantially lower (112 nm - 2  $\mu\text{m}$ ) than the grain size produced in the laboratory (6  $\mu\text{m}$ ). This is attributed to the fact that the laboratory experiments focused on creating WEL by imposing certain thermal cycles, but without mechanical loading. As a result, further grain refinement due to severe plastic deformation of the rail surface is not obtained in the experiments. On the other hand, the hardness of the laboratory (850 HV) and field WEL (820 HV) are in good agreement.

According to the comparison of these microstructures, the sample with a single cycle of fast heating and quenching has a microstructure that is more comparable to the one found in WEL from the field than the sample with 10 cycles. However, it is worth noting that in the experiments reported in this chapter, complete austenitization of the rail surface followed by quenching to room temperature is simulated.

During wheel/rail contact, austenitization may not be complete. Certain contacts, for example, may reach intercritical temperature ranges and not cool down to room temperature before the next cycle begins. Furthermore, WEL is known to be formed in specific locations after a certain loading history of the rails which suggests that the rail surface is not fully austenitized in each wheel/rail contact. This means that it is unlikely that each wheel/rail contact reaches temperatures above  $A_3$ , leading to the full austenitization of the surface layer, as simulated in the present chapter. The peak temperature in the contact patch might reach temperatures within the intercritical temperature range and only a fraction of the pearlite is transformed into austenite and thus, martensite after quenching. All these variations might have an impact on the final WEL microstructure.

## 2.4. CONCLUSIONS

This chapter discusses the microstructural changes observed in a pearlitic railway steel subjected to fast heating (200  $^{\circ}\text{Cs}^{-1}$ ) followed by controlled cooling at different cooling rates. The effect of severe plastic deformation is not taken into account. The experimental investigation shows that:

- As a result of the intermediate cooling rates, martensitic bands and pearlitic/bainitic bands are observed in the microstructure. This unforeseen behavior is caused by the segregation of elements such as Mn and Si. The segregation bands promote microstructural anisotropy, which causes a shift in the dilatometer curves during cyclic heat treatments.
- Soaking for 5 minutes at high temperatures allows sufficient Mn diffusion in austenite to eliminate traces of prior cementite.
- Cyclic heating to the fully austenitic range and quenching does not lead to continued grain refinement of prior-austenite grains, indicating that the main cause of grain refinement in the WEL is the plastic deformation of railway surfaces during wheel and rail contact.
- Comparable hardness is obtained for WEL produced in laboratory and the one from field conditions. This suggests that phase transformation is a dominant aspect in WEL formation and increase in hardness of these layers.

- Repeated cycling leads to a microstructure that is more homogeneous than the one observed after one cycle. This is mainly due to the absence of ghost-pearlite after 10 cycles suggesting that Mn can diffuse out of cementite lamellae locations, homogenizing in the austenite. However, in field conditions the rail experiences possible variations in peak temperature, heating rate, and cooling rate which have an effect on the final microstructure of the surface layer.
- Similar microstructural features are observed in WEL from field and after a single cycle of fast heating followed by quenching. However, the very small grain size observed in WEL produced during wheel/rail contact is not reproducible by thermal heating only. This suggests that such a level of grain refinement is due to severe plastic deformation.



# DETAILS OF PEARLITE TO AUSTENITE TRANSFORMATION IN STEEL: EXPERIMENTS AND PHASE-FIELD MODELING

*The austenitization of an initial pearlitic microstructure is simulated using the phase field model to achieve insight into White Etching Layer (WEL) formation in pearlitic railway steels. The simulations take into account the resolution of the cementite lamellae within a pearlite colony as well as the presence of pro-eutectoid ferrite. The austenite growth kinetics and morphology obtained via simulations are compared with dilatometry and microscopy observations. The influence of  $\gamma/\theta$  and  $\gamma/\alpha$  mobilities on the austenite growth morphology are studied. The simulations reproduce the microstructural features as well as the experimentally observed kinetics behavior of austenite formation, involving the correlation between mobilities and nucleation behavior.*

---

This chapter is based on:

- V. Mattos Ferreira, M.G. Mecozzi, R.H. Petrov, J. Sietsma, "Details of pearlite to austenite transformation in steel: experiments and phase-field modeling", Computational Materials Science, 2023, vol.228, 112368.

### 3.1. INTRODUCTION

Railway steels are subjected to complex loading conditions during service due to wheel and rail contact leading to the development of rolling contact fatigue (RCF), the dominant damage mechanism in rails [72]. Several studies have identified the microstructural aspects of RCF damage development in railway steels, such as inclusions, pro-eutectoid ferrite, and microstructural changes in the rail's surface, known as White Etching Layers (WEL) [31, 73, 74, 75]. WEL develops due to wheel and rail contacts and is detrimental to rail service life as it is associated with preferential sites for crack nucleation and growth due to its brittle nature [42, 55]. For this reason, it is critical to comprehend the mechanisms that occur during WEL formation in order to design appropriate methods of reducing or preventing its occurrence.

In the past years, the microstructural features of different WEL found in railway steel grades have been extensively investigated. As a result, several hypotheses were developed to explain the mechanisms of WEL development [41, 44, 46]. One of these hypotheses argues that WEL is formed due to temperature rise during wheel and rail contact [24, 37, 38]. Basically, the wheel and rail contact would generate sufficient heat to increase the temperature at the rail surface above austenitization temperatures. The austenite would then be transformed into martensite during fast cooling, forming the WEL.

However, it is not possible to exactly determine the temperature profile and mechanical loading during heating of the railway surface due to the small contact area and very short time scale. This leads to difficulties when trying to reproduce the field conditions in a laboratory setup. Even if the temperature profile would be known, the characterization of austenite ( $\gamma$ ), which is stable at high temperatures, is quite complex. Therefore, the understanding of austenite formation in such conditions remains a challenge.

Some studies have experimentally investigated the microstructural features of austenite formation in pearlite. Speich et al. [76] separated the kinetics of austenite formation in dual-phase steels into three stages. First, the nucleation of austenite at ferrite/pearlite interfaces with rapid growth of austenite into pearlite as it is controlled by C diffusion over very short diffusion distances. The growth rate is then greatly reduced when austenite grows into pro-eutectoid ferrite. The final step would be the Mn equilibration in austenite which is a very long process. Shtansky et al. [77] focused on the morphology of nucleation and growth of austenite from pearlite using Transmission Electron Microscopy (TEM). Nucleation of austenite seemed to occur preferentially at the pearlite colony boundaries. However, some nuclei were also observed within the pearlite colonies at pearlitic cementite/ferrite interfaces. They also noted the different morphologies of the ferrite/austenite front and the preferential growth of austenite towards one specific neighboring pearlite colony. Li et al. [78] presented a crystallographic study indicating that austenite preferentially nucleates at the high angle boundaries of pearlitic ferrite and it preferentially grows into the adjacent pearlitic ferrite.

On the other hand, advances in computer simulations of phase transformations enable the understanding of the effect of different conditions on the phase transformation kinetics and morphology. Several studies have analyzed the austenite formation from a pearlitic microstructure using different modeling approaches [76, 79, 80, 81].

Phase field modeling (PFM) has the advantage of enabling the simulation of complex growth morphologies [82]. However, not many studies have reported the use of PFM for simulating austenite formation from an initial pearlitic structure. Savran [83] and Thiessen



et al. [84] simulated austenite formation from a ferrite-pearlite microstructure but considered pearlite as supersaturated ferrite with eutectoid carbon content. On the other hand, Rudnizki et al. [85] used the same approach while considering pearlite as a phase with mixed properties of ferrite and cementite. Other studies [13, 64, 83] considered the resolution of the cementite lamellae in the pearlite but in a very small domain only containing two to a maximum of five lamellae in the initial microstructure. Finally, Militzer et al. [86] simulated austenite formation from a 2D and 3D pearlitic structure taking into account the resolution of the cementite lamellae. However, no presence of pro-eutectoid ferrite was considered, and to avoid more complexity, the nucleation behavior as well as its influence was not analyzed in their work.

The focus of this chapter is on the microstructural development during the wheel and rail contact due to thermo-induced phase transformation without incorporating the effect of plastic deformation. In order to do so, the austenitization of an initial pearlitic microstructure is simulated using the phase field model for two different heating rates: 10 and 200 °Cs<sup>-1</sup>. The initial domain consists of a pro-eutectoid ferrite grain which is surrounded by three pearlite colonies with approximately twenty cementite lamellae each. The domain size is chosen to resolve the features of cementite lamellae within a pearlite colony within reasonable limits for the computational time. The austenite growth kinetics and morphology obtained via simulation are compared with dilatometry and microscopic observations. Moreover, the influence of  $\gamma/\theta$  and  $\gamma/\alpha$  mobilities on the morphology is studied.

### 3.2. MATERIAL AND EXPERIMENTAL PROCEDURE

In this study, experiments were performed on R260Mn pearlitic railway steel which is commonly used in the Dutch railway network. This steel grade has a close-to-eutectoid chemical composition as previously shown in Table 2.1 with the main alloying elements being C, Mn, and Si. XRD analysis shows the presence of 89% BCC phase (ferrite) and 11% cementite.

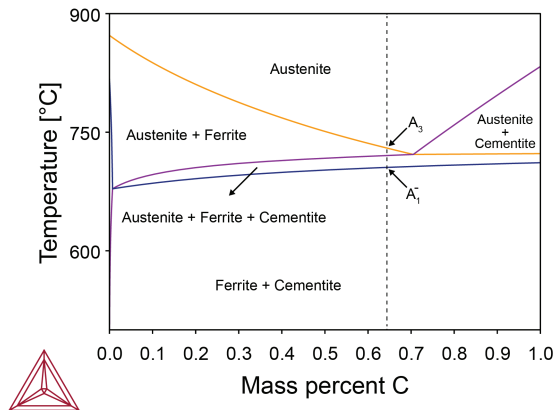


Figure 3.1: Fe-C phase diagram for R260Mn steel obtained using Thermo-Calc software. The dashed line at 0.64 wt% C represents the carbon concentration in the studied alloy. Black arrows indicate the estimation for  $A_1^-$  and  $A_3$  temperatures under equilibrium conditions.

Figure 3.1 shows the Fe-C phase diagram for the constant values of Mn and Si concentrations, calculated using Thermo-Calc version 2021b with TCFE11 database [87]. The dashed vertical line represents the carbon concentration of R260Mn steel (0.64 wt.%) and provides an estimation for the  $A_1^-$  and  $A_3$  temperatures for equilibrium conditions, respectively equal to 705 °C and 730 °C, as indicated by the arrows.

Scanning Electron Microscopy (SEM) shows the presence of pearlite colonies as well as a small fraction of pro-eutectoid ferrite decorating the prior-austenite grain boundaries (Figure 3.2), which results from a slight deviation from the eutectoid composition as shown in Figure 3.1. From the SEM analysis in Figure 3.2b, an estimation for the interlamellar spacing and cementite lamella thickness of approximately 150 and 20 nm is obtained, respectively.

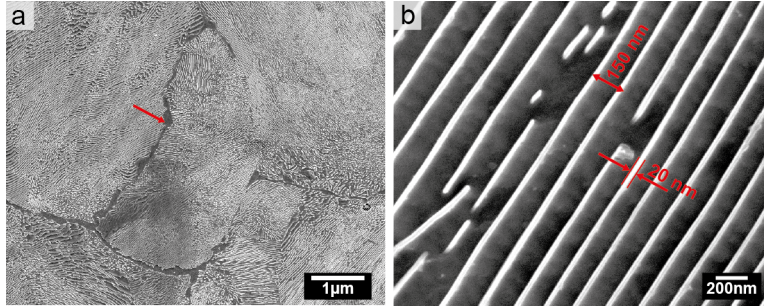


Figure 3.2: SEM micrographs of the as-received R260Mn railway steel (a) evidencing the pearlitic microstructure with the red arrow indicating pro-eutectoid ferrite at the grain boundaries and (b) higher magnification micrograph showing the interlamellar spacing and lamella thickness.

The values of the equilibrium transition temperatures,  $A_1^-$  and  $A_3$ , served as guidelines for the design of dilatometry experiments with low and high heating rates. To investigate the kinetics of pearlite transformation during fast heating, dilatometric tests were performed in a Bähr 805A dilatometer. This instrument uses an induction coil to heat the sample and detects the length change of the sample with a linear variable displacement transducer. The power supply is adjusted to maintain the desired heating rate. Flat specimens with 1.5 mm thickness, 4 mm width, and 10 mm length were machined from the rail piece with the length coinciding with the running direction of the rail. Two thermocouples were spot welded at the center (TC1) and edge (TC2) of the specimen length, to investigate the temperature homogeneity in the sample during the test. The temperature control is based on TC1.

A first heat treatment ( $H_T$ ) was carried out by heating the specimen with a high heating rate ( $200\text{ °C s}^{-1}$ ) up to 900 °C (170 °C above the equilibrium  $A_3$  temperature) followed by quenching. This heat treatment was performed to determine  $A_{c1}$  and  $A_{c3}$ , and therefore the overheating required for the pearlite transformation with respect to the equilibrium transition temperatures due to fast heating. As will be explained in section 3.3, the kinetics of the pearlite to austenite transformation at high heating rates cannot be extracted from the dilatometer curve of the specimen subjected to rapid heating. To overcome this, an additional heat treatment ( $L_T$ ) with a lower heating rate ( $10\text{ °C s}^{-1}$ ) up to 900 °C was performed, aiming at deriving the transformation kinetics to fit the simulation results.

Interrupted heating was performed to examine the microstructural features of austenite during the early stages of transformation. For this reason, two additional heat treatments with high and low heating rates were performed with the heating stage interrupted at

the onset of the pearlite to austenite transformation, slightly above the  $A_{c1}$  temperature, followed by quenching. The goal of this set of experiments is to obtain small fractions of martensite (austenite at high temperatures), which are important for understanding austenite morphology in the early stages of phase transformation and will serve as guidelines for validating the simulation results. It also makes it possible to compare the austenite formed at high and low heating rates.

The microstructural features were observed using a JEOL JSM-6500F scanning electron microscope after standard metallography sample preparation followed by chemical etching with Nital 2%. The microstructural analyses were done in the vicinity of TC1 where the maximum temperature before quenching is measured. Throughout this chapter the specimen identification has been done in the following manner:  $A_z$  with A being the type of heating rate (H or L) and z the peak temperature (in °C) reached before quenching.

### 3.3. EXPERIMENTAL RESULTS

Figure 3.3a shows the dilatation and austenite fraction as a function of temperature for sample H<sub>900</sub> where a sharp increase of the dilatation signal is observed at 773 °C. A detailed explanation of the possible cause of this peak can be found in [88]. In summary, there is a temperature difference of approximately 60 °C between the middle (TC1) and the edge (TC2) of the dilatometry sample. Besides, the Curie temperature of this steel (757 °C) coincides with the onset of austenite formation at high heating rates. When the center of the specimen reaches the Curie temperature (757 °C), the edge of the sample is still 60 °C below this temperature. Therefore, when the controlling thermocouple located in the center of the sample crosses this temperature, the equipment increases the power input to maintain the high heating rate. This causes a sharp increase in the heating rate at the edge of the sample where the material is still ferromagnetic and consequently the anomalous peak, due to thermal expansion, in the dilatation curve.

Unfortunately, this sharp increase of the dilatation coincides with the start of austenite formation, and that makes it impossible to precisely derive the value of  $A_{c1}$ , as is usually done from the deviation of the linearity of the dilatation curve. This peak also interferes with the calculation of the phase fraction formed, especially at the temperature range highlighted with a light grey rectangle in Figure 3.3a, where the temperature gradient and heating rates are substantially different between the central and edge regions. The austenite fraction values within the grey-shaded range are therefore disregarded. However, the later stage of phase transformation kinetics (after 50% of austenite is formed) will still be considered as a reference for the simulations. In this case, we assume that a delay takes place due to thermal gradients which can be estimated by the temperature difference between TC1 and TC2 at approximately 11 °C after the pearlite is fully transformed to austenite. At temperatures above the peak, the decrease in the dilatation signal reflects the ongoing pearlite-to-austenite transformation. The transformation is complete at approximately 805 °C, the value assigned to  $A_{c3}$  for a heating rate of 200 °Cs<sup>-1</sup>.

Figure 3.3b presents the dilatation signal and phase fraction of austenite formed for sample L<sub>900</sub>, subjected to the lower heating rate of 10 °Cs<sup>-1</sup>. As can be seen, both  $A_{c1}$  and  $A_{c3}$  are lower than for sample H<sub>900</sub>. This means that a higher overheating is necessary for austenite to form at 200 °Cs<sup>-1</sup> than at 10 °Cs<sup>-1</sup>. The influence of the heating rate and the intercritical temperature shift has been previously reported in the literature [89].

Figure 3.3c shows the temperature profiles recorded from the two thermocouples

welded to the samples subjected to intercritical heating with different heating rates ( $H_{751}$  and  $L_{745}$ ) followed by quenching. The peak temperatures measured at the location of TC1 were 751 °C and 745 °C. As these samples were subjected to heating up to the early stage of austenite formation, there is no discernible divergence from linearity in the dilatation curves. This is due to the limitation of the equipment to detect such a small fraction of phase transformation in both heating and cooling curves.

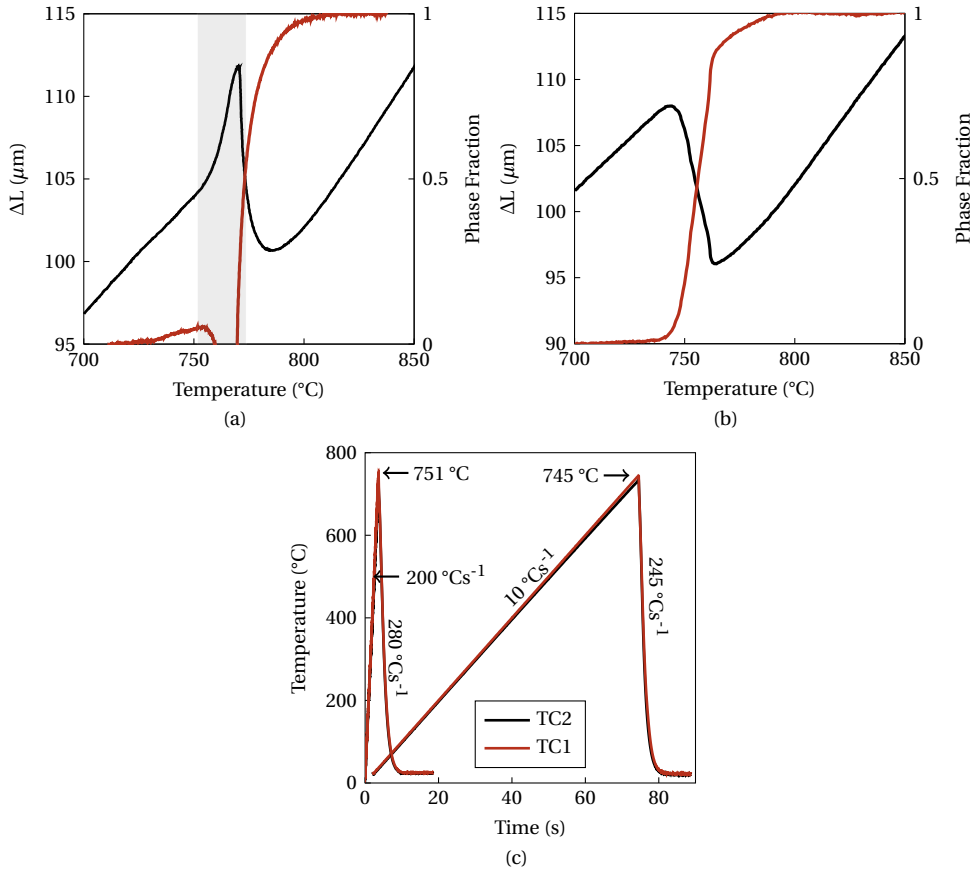


Figure 3.3: Dilatation and austenite phase fraction as a function of temperature for samples (a)  $H_{900}$  and (b)  $L_{900}$ ; (c) Time-temperature graph of  $L_{745}$  and  $H_{751}$  subjected to intercritical austenitization followed by quenching.

The microstructures of samples  $H_{751}$  and  $L_{745}$  were examined using SEM to determine the presence of small martensitic patches (austenite at high temperatures). These patches provide knowledge on the nuclei sites and early growth behavior of austenite, which is necessary to further investigate the microstructural aspects of austenite formation using phase field simulations.

Figure 3.4 shows a series of micrographs of regions containing transformed patches of martensite in  $H_{751}$  (a-f) and  $L_{745}$  (g-i). Overall, the growth morphology of austenite is similar for both samples. The martensite patches observed are not homogeneously distributed in the microstructure but rather situated in preferential locations, such as at pro-eutectoid fer-

rite boundaries (Figure 3.4a,b), inside pearlite colonies (Figure 3.4d,e,g,h) and at the pearlite colonies' boundaries (Figure 3.4c,f,i). These preferential sites for austenite nucleation and growth in pearlitic microstructures have been previously reported in the literature for different heating rates [78, 90].

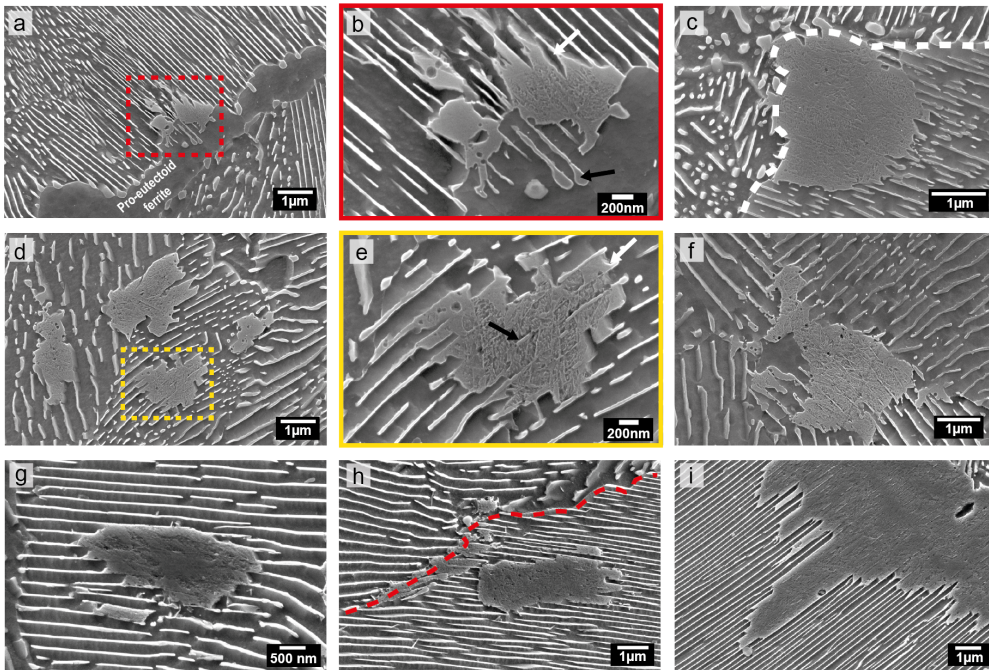


Figure 3.4: SEM image of martensitic patches found in samples H<sub>751</sub> (a-f) and L<sub>745</sub> (g-i). White arrows in (b) and (e) indicate sharp- and flat-front growth of austenite, respectively. Black arrows in (b) and (e) show the nuclei of austenite and the undissolved cementite, respectively. Dashed lines in (c) and (h) highlight the pearlite boundary.

An additional aspect that can be extracted from these micrographs is the growth morphology of austenite at the onset of the pearlite to austenite transformation. The martensite patches that nucleated at the boundaries show a similar pattern of growing towards the bulk of a preferential pearlite colony. This trend is observed in Figure 3.4c where the austenite grows mainly towards one specific colony of pearlite. Figure 3.4b shows an enlarged portion containing a martensite patch. The martensite front (austenite at high temperature) presents a sharp shape, growing preferentially along the cementite lamellae (white arrow). That is reasonable as cementite is richer in carbon than ferrite and thus plays an essential role during austenite growth at high temperatures. On the other hand, the enlarged region in Figure 3.4e accounts for another growth mechanism highlighted by a white arrow. In this case, the austenite front is much flatter between the two cementite lamellae. Moreover, in this case, regions with thinner cementite lamellae can be observed (black arrow) which are due to partial transformation of cementite during the austenitization process. These findings have been previously reported in the literature by Shtansky et al. [77].

In summary, the main microstructural features of austenite growth in pearlite are:

- Growth along cementite lamellae (sharp front);

- Growth along ferrite (flat front);
- Preferential growth towards a pearlite colony;
- Undissolved cementite inside austenite.

### 3.4. PHASE-FIELD MODELLING

#### 3.4.1. PHASE-FIELD THEORY

The multi-phase field model proposed by Steinbach et al. [91] and extended to multicomponent alloys by Eiken et al. [92] is used to simulate the growth of austenite from an initial pearlitic microstructure. In this approach, each grain ( $i$ ) is described by the phase-field parameter,  $\phi_i(\vec{x}, t)$ , which can assume the value of 1 if the grain  $i$  is present at a location  $\vec{x}$  and time  $t$  or the value of 0 if the grain  $i$  is not present. The field parameter varies smoothly at the grain boundaries from 0 to 1 over a diffuse transition region of width  $\eta$ . In addition, each grain has a set of attributes that are relevant for describing the transformation of interest such as the lattice structure (phase) and the crystallographic orientation. In the case of a multi-component alloy, a concentration vector  $\mathbf{c}(\vec{x}, t)$  is defined to describe the local composition of alloying elements:

$$c^k(\vec{x}, t) = \sum_{i=1}^v \phi_i c_i^k(\vec{x}, t) \quad (3.1)$$

with  $v$  being the number of coexisting grains at location  $\vec{x}$  and  $c_i^k$  the concentration of solute  $k$  in the individual grain  $i$ . The time evolution of  $v$  phase-field parameters describes the kinetics of the phase transformation and it is obtained by solving the following phase-field equations:

$$\dot{\phi}_i = \sum_{j \neq i}^v M_{ij}^{\phi} \left[ b \Delta G_{ij} - \sigma_{ij} K_{ij} + \sum_{\substack{j \neq i \\ j \neq k}}^v J_{ijk} \right] \quad (3.2)$$

where  $M_{ij}^{\phi}$  is the phase-field mobility of the interface between grains  $i$  and  $j$ ,  $b$  a numerical weight constant,  $\Delta G_{ij}$  the thermodynamic driving force,  $\sigma_{ij}$  the interfacial energy between grains  $i$  and  $j$ ,  $K_{ij}$  the pairwise curvature contribution and  $J_{ijk}$  the triple junction term, which is zero for  $v = 2$ . The driving force in Eq. (3.2) depends on the local composition  $\mathbf{c}(\vec{x}, t)$ . Therefore, Eq. (3.2) is solved coupled with a set of diffusion equations, given by

$$\frac{\partial c^k}{\partial t} = \nabla \cdot \sum_{i=1}^v \sum_{l=1}^{\xi} \phi_i D_i^{kl} \nabla c_i^l \quad (3.3)$$

$$D_i^{kl} = \sum_{m=1}^{\xi} M_i^{ch, km} \Phi_i^{ml} \quad (3.4)$$

in which  $\xi$  is the number of alloying elements and  $\Phi_i^{ml}$  denotes thermodynamic factors used to convert the chemical atomic mobilities  $M_i^{ch, km}$  into diffusivity  $D_i^{kl}$  [92].

The phase-field model is derived as a growth model, in which the nucleation behavior is considered depending on the input density, distribution, and growth rate of the nuclei [93].

In commercial software such as MICRESS<sup>®</sup>, the nuclei density is controlled by two main parameters: shield distance and shield time. The shield distance defines the minimum distance between nuclei formed within the shield-time interval. The shield time controls the formation of new nuclei, which is only allowed at the onset of a shield-time interval. For example, if a shield time  $t$  is and shield distance  $d$  are considered, simultaneous nucleation will only occur at every time interval  $t$  with a minimum distance of  $d$  between the nuclei. The nucleation occurs when the local overheating (calculated by Thermo-Calc based on the local composition) is higher than the overheating required for nucleation, which is one of the input parameters.

### 3.4.2. SIMULATION CONDITIONS

2D phase-field simulations were performed to study the pearlite to austenite transformation in an Fe - 0.64 wt% C - 1.4 wt% Mn ternary alloy during heating at 10 and 200 °C<sup>s</sup><sup>-1</sup>. The MICRESS<sup>®</sup> (version 7.123, Access e.V., Aachen, Germany) software [94] was used to solve the phase-field equations (eq. (3.2) coupled with eq. (3.3)) and enable the simulation of microstructure morphology and alloy element distribution in time and space.

The construction of the simulated initial microstructure is done by taking the 2D SEM micrograph (Figure 3.2a) as a reference, see Figure 3.5. However, the large domain from the SEM micrograph would impose a challenge in resolving the cementite lamellae because of the extensive simulation time. Due to this limitation, a smaller domain of approximately 6x6 μm<sup>2</sup> is considered as the initial microstructure.

As can be seen from Figure 3.5, the domain contains the boundary region of three pearlite colonies with the resolved cementite lamellae parallel to each other within each colony. In one portion of the colonies, some gaps were placed between cementite segments, one of which is highlighted with a black arrow. This feature is incorporated to take into account the discontinuities observed in the pearlite as it is not a perfectly continuous structure. The interlamellar spacing corresponds to the one measured in the as-received material (150 nm). Moreover, the presence of pro-eutectoid ferrite in the boundary region observed in the SEM micrograph (Figure 3.2) is also taken into account.

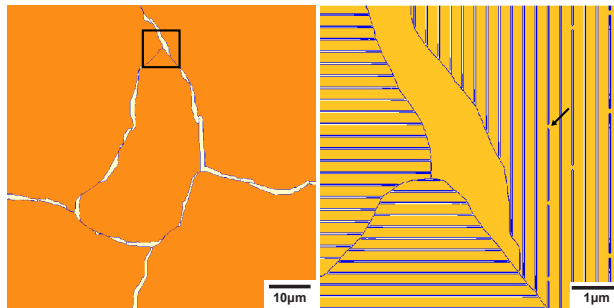


Figure 3.5: Initial microstructure with the resolved cementite lamellae in the pearlitic microstructure used in the phase field simulations.

The grid size was set to 0.01 μm with the interface thickness ( $\eta$ ) corresponding to three grid cells. Isolated boundary conditions were assumed in all simulations. The composition of ferrite and the cementite lamellae was set equal to the equilibrium conditions at 700 °C. The temperature profile applied for dilatometry experiments was employed. The only mod-

ification is that the beginning temperature for the simulation is set to 735 °C and 719 °C for 10 °Cs<sup>-1</sup> and 200 °Cs<sup>-1</sup>, respectively, to shorten simulation time as no phase transformation occurs below these temperatures.

Table 3.1 presents the kinetics parameters assumed in the simulations. The  $\alpha/\alpha$ ,  $\alpha/\theta$ , and  $\gamma/\gamma$  interface mobilities are considered to be very low to limit the study to the analysis of  $\gamma/\alpha$  and  $\gamma/\theta$  interfaces. For  $\gamma/\alpha$  and  $\gamma/\theta$  interfaces, the mobility is considered to be temperature dependent according to the Arrhenius relation:

$$M = M_0 \exp\left(-\frac{Q}{RT}\right) \quad (3.5)$$

where  $Q$  is the activation energy for interface motion (140 kJmol<sup>-1</sup> [95]),  $R$  the gas constant (8.31 JK<sup>-1</sup>mol<sup>-1</sup>) and  $M_0$  the pre-exponential factor. The pre-exponential factor and, consequently, the mobilities of the  $\gamma/\theta$  and  $\gamma/\alpha$  interfaces play an important role in the final morphology of the austenite front. The same counts for the interface energies. However, accurate values of mobility and interfacial energy are still missing. For this reason, values in the same order of magnitude as reported in the literature [96, 97] were chosen, considering that the microstructural evolution is in agreement with the experimental observations. The interfacial energies and the pre-exponential factor values of the mobilities of the different grain boundaries and interfaces are reported in Table 3.1.

Table 3.1: Kinetic parameters used in the simulations with MICRESS<sup>®</sup>.

Interface	$\alpha/\alpha$	$\alpha/\theta$	$\gamma/\alpha$	$\gamma/\theta$	$\gamma/\gamma$
Interfacial energy (Jm <sup>-2</sup> )	0.70	0.50	0.60	0.40	0.70
Interface mobility (m <sup>4</sup> J <sup>-1</sup> s <sup>-1</sup> )	$5 \times 10^{-16}$	$5 \times 10^{-16}$	$M(T)$	$M(T)$	$5 \times 10^{-16}$

MICRESS<sup>®</sup> also requires input parameters for the nucleation of austenite nuclei such as the maximum number of nuclei, shield time, and shield distance. The combination of these parameters defines the nuclei density, which can strongly affect the final result, especially for simulations with small domains. In the current study, all simulations considered two possible nucleation sites for austenite:

- at  $\alpha/\alpha$  grain boundaries (pro-eutectoid ferrite/pearlitic ferrite or pearlitic ferrite/pearlitic ferrite);
- at  $\alpha/\theta$  interfaces (pro-eutectoid ferrite/cementite or pearlitic ferrite/cementite).

The simulations consider a very small pearlitic domain which makes it impossible to obtain a good estimation of the austenite grain sizes and relate these to the experimental values. As a result, no correlation can be made between the experimental grain sizes and the nucleation rate [98]. Consequently, the nucleus density together with interface mobility was set to fit the phase fraction curve for each simulation.

MICRESS allows the attribution of a parameter  $\phi$  for each grain in 2D simulations. This parameter can be used to control the directionality of the mobility anisotropy to accomplish the non-isotropic growth of grains. In this chapter, when a new austenite nucleus is set at the boundary of two colonies, a  $\phi$  value is assigned to it. MICRESS code allows assigning to a new grain a  $\phi$  value which is related to  $\phi$  of one of the two neighboring parent ferrite grains, randomly selected. As a result of the assumed anisotropy, the nuclei exhibit a distinctive



growth pattern, predominantly growing towards a specific pearlite colony rather than displaying isotropic growth towards all neighboring grains. The new austenite grain does grow isotropically within the parent grain and the mobility within the non-parent neighboring grain is set to zero. No acicular morphology is considered.

Thermodynamic data are required to evaluate from the local concentration the overheating to set the nuclei of the austenite phase (a new nucleus is set when the critical nucleation overheating, assigned as an input parameter, is exceeded), the driving force for the austenite growth, and also the diffusivity and partitioning of the alloying elements into the coexisting phases in the diffuse interface under quasi-equilibrium constraint (equal chemical potential at the interface). The evaluation of this constraint is done by minimization of the multiphase Gibbs free energy, calculated from Calphad databases via the TQ-interface of the Thermo-Calc software.

### 3.4.3. SIMULATION RESULTS

#### EFFECT OF $\gamma/\theta$ MOBILITY

The two-dimensional (2D) phase-field simulations presented in this section aim at understanding the effect of the  $\gamma/\theta$  mobility on the growth morphology of the austenite. To achieve this, the pre-exponential factor of the  $\gamma/\alpha$  interface mobility ( $M_0^{\gamma/\alpha}$ ) is set at a value equal to  $10^{-6} \text{ m}^4\text{J}^{-1}\text{s}^{-1}$  while the pre-exponential factor of the  $\gamma/\theta$  interface mobility ( $M_0^{\gamma/\theta}$ ) varies for each simulation. Four values of  $M_0^{\gamma/\theta}$  are considered, ranging from  $10^{-8}$  to  $10^{-5} \text{ m}^4\text{J}^{-1}\text{s}^{-1}$ . It is important to note that the exact values of interface mobility and nucleation parameters are unknown. A strong correlation emerges when achieving agreement between experimental and simulated fraction curves.

The choice of parameters is based on fitting the austenite fraction of the simulations with different  $M_0^{\gamma/\theta}$  conditions to the one obtained experimentally (Figure 3.3b). A change in mobility leads to changes in the kinetics of the phase transformation. To overcome this, the nuclei density is adjusted for each simulation to obtain a good fit for the experimental results. As no experimental information regarding the nucleation rate is available, a shield time of 1.0 s is assumed as an input parameter for all simulations while the nuclei density is adjusted to obtain a proper kinetics representation. In addition, all simulations consider a heating rate of  $10 \text{ }^\circ\text{C s}^{-1}$  in accordance with the experiment (3.3b). This means that new nuclei are allowed to form at intervals equal to 1.0 s (10  $^\circ\text{C}$  intervals on the temperature scale).

Figure 3.6a shows the austenite fraction as a function of temperature for the experimental and simulated conditions. As can be seen, the simulated curves accurately replicate the overall kinetics of the transformation observed experimentally. Figure 3.6b presents the number of austenite nuclei as a function of temperature considered for each pre-exponential mobility factor. The nucleation occurs in two events for all simulations. The first happens at the onset of the simulation (735  $^\circ\text{C}$ ) and is marked by a lower density of nuclei to achieve the slower transformation rates observed at the beginning of the phase transformation, see Figure 3.6a. The second nucleation event takes place at 745  $^\circ\text{C}$  which corresponds to the increase in the kinetics of austenite formation. The faster transformation rates are due to an increase in austenite nuclei density and austenite/pearlite interface area. No further nucleation occurs until the end of the simulation and the kinetics is controlled only by the growth of the existing nuclei.

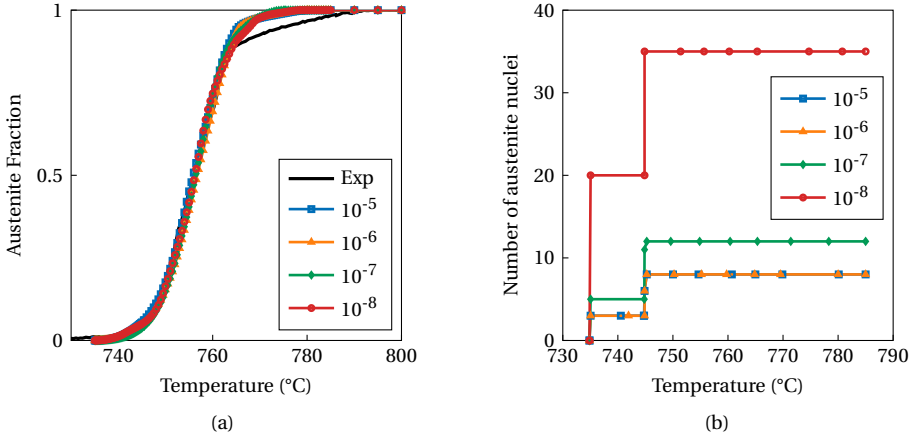


Figure 3.6: (a) Austenite phase fraction as a function of temperature obtained experimentally (black solid curve) and via phase field simulation with different pre-exponential factors for  $\gamma/\theta$  mobility (colored lines with symbols) and (b) Number of austenite nuclei as a function of temperature for each simulation with different pre-exponential factors of  $\gamma/\theta$  mobility. The unit of the interface mobilities is  $\text{m}^4\text{J}^{-1}\text{s}^{-1}$ .

The analysis of the nuclei density in Figure 3.6 shows that a further increase of the interface mobility above a threshold value does not require an adjustment of the nucleation setting to fit the kinetics, meaning that the austenite formation occurs under diffusion control. Diffusion during austenite formation will be discussed later, in section 3.4.3. On the other hand, lower mobilities imply mixed-mode growth, so both interface mobility and diffusion play a significant role in the kinetics. For this, it is necessary to increase the nuclei density to compensate for the lower mobility such as observed for  $M_0^{\gamma/\theta}$  equal to  $10^{-7}$  and  $10^{-8} \text{ m}^4\text{J}^{-1}\text{s}^{-1}$ . In summary, austenite formation can be characterized as a mixed-mode transformation for lower mobilities ( $M_0^{\gamma/\theta}$  equal to  $10^{-7}$  and  $10^{-8} \text{ m}^4\text{J}^{-1}\text{s}^{-1}$ ) but shifts towards diffusion controlled for higher mobilities ( $M_0^{\gamma/\theta}$  equal to  $10^{-6}$  and  $10^5 \text{ m}^4\text{J}^{-1}\text{s}^{-1}$ ).

The dilatometry results highlight a decrease in the rate of austenite formation at the final stages of the austenite formation, see Figure 3.6a. This behavior is attributed to the growth of austenite into the pro-eutectoid ferrite which occurs at a much lower rate than into pearlite due to long-range carbon diffusion [99]. For this reason, the pro-eutectoid ferrite regions are expected to transform to austenite at a later stage and at a lower rate than the pearlite. However, it is not possible to fully control the nuclei positions in the simulation nor differentiate between austenite/pro-eutectoid ferrite and austenite/pearlitic ferrite interfaces. This leads to nucleation and growth occurring in the pro-eutectoid ferrite at 745 °C, reducing its effect by the end of the simulation. Although it was not possible to fit the simulation curves properly in this portion of the experimental curve, a reduction of the transformation rates was still achieved, providing a good representation of the change in kinetics.

In Figure 3.7, the simulated microstructure evolution at 750 °C (a) and 760 °C (b) for different  $M_0^{\gamma/\theta}$  are depicted. These stages are representative of the early and intermediate stages of austenite formation. At 750 °C differences are seen in the growth morphology of austenite (red grains) due to differences in mobility. For higher values of  $M_0^{\gamma/\theta}$ , the grains

nucleated within the pearlite (black arrows) show a sharp front that has also been observed experimentally, see Figure 3.4b. This morphology changes to a more equiaxed round shape by decreasing  $M_0^{\gamma/\theta}$ . For  $M_0^{\gamma/\theta}$  equal to  $10^{-8} \text{ m}^4\text{J}^{-1}\text{s}^{-1}$ , the cementite is encapsulated by the surrounding austenite (see black arrow in Figure 3.7a) instead of being completely transformed, such as observed for the other cases.

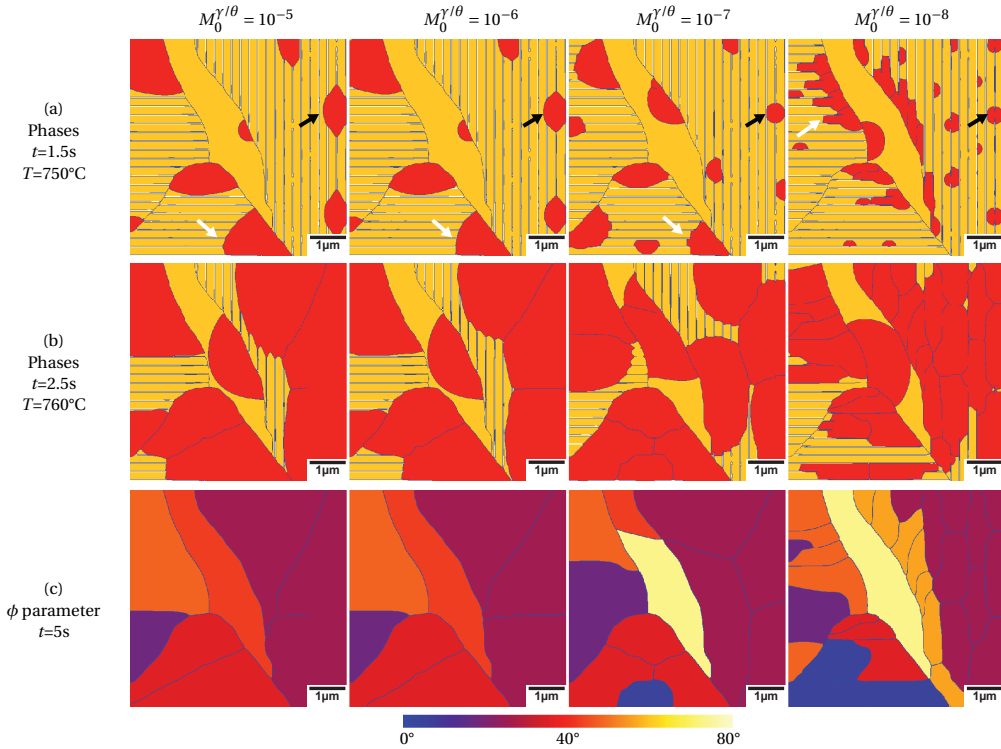


Figure 3.7: (a,b) Simulated microstructural evolution at  $t = 1.5$  and  $2.5$  s for different  $\gamma/\theta$  pre-exponential factors ( $M_0^{\gamma/\theta}$ ) with red grains representing the austenite phase. (c)  $\phi$  parameter for  $t = 5$  s (fully transformed microstructure) for different  $M_0^{\gamma/\theta}$  ( $\text{m}^4\text{J}^{-1}\text{s}^{-1}$ ), with colors indicating the  $\phi$  parameter (see section 3.4.2).

The nuclei located at the colony boundaries (white arrows) not only grow towards the bulk of the pearlite colony but also along the colony boundaries. The preferential growth towards one specific pearlite colony is due to the mobility anisotropy considered in this study and is in accordance with experimental observations.

The growth front of these nuclei has a more continuous appearance for higher mobilities, suggesting that the austenite front moves at approximately the same rate as the cementite dissolution. On the other hand, lower  $\gamma/\theta$  interface mobilities lead to a flat austenite growth front. In this case, the austenite grows preferentially into the ferrite within two adjacent cementite lamella due to the higher mobility of the  $\gamma/\alpha$  interface. In this case, the velocity of the  $\gamma/\theta$  interface is reduced, leading to a delay of the cementite dissolution with the growth of austenite. This flat growth is also experimentally evidenced in partially transformed pearlite microstructures, see Figure 3.4e.

At the end of the simulation, both pearlite and pro-eutectoid ferrite are transformed into austenite. The  $\theta$  parameter of the final grains is depicted in Figure 3.7c. Adjacent austenite grains with the same  $\theta$  parameter can appear in micrographs as a single austenite grain which was transformed into martensite during quenching. As expected, the nuclei density has a clear effect on the final austenite grain size. As previously mentioned, lower mobility requires a higher nuclei density to achieve the same kinetics. Consequently, the austenite grain size decreases with decreasing mobility. The morphology of the grains is also influenced in this case, changing from a more polygonal to an elongated shape during the phase transformation.

### DIFFUSION PROCESSES

Figure 3.8 shows the carbon profile in  $\gamma$  and  $\alpha$  of a small portion of the simulated microstructure for the highest and lowest  $M_0^{\gamma/\theta}$  mobilities at 743 and 751 °C, respectively. As can be seen, carbon concentration gradients in  $\gamma$  and  $\alpha$  are present regardless of the interface mobility. For high mobilities, a sharp austenite front is observed with higher carbon contents at the  $\gamma/\theta$  interface region while lower carbon contents are present at the  $\gamma/\alpha$  interface. At this condition, carbon does not have enough time to homogenize in the fast-growing austenite, which leads to carbon concentration gradients within the austenite grain. As cementite is the main carbon source for austenite growth, the locations near cementite are enriched in carbon.

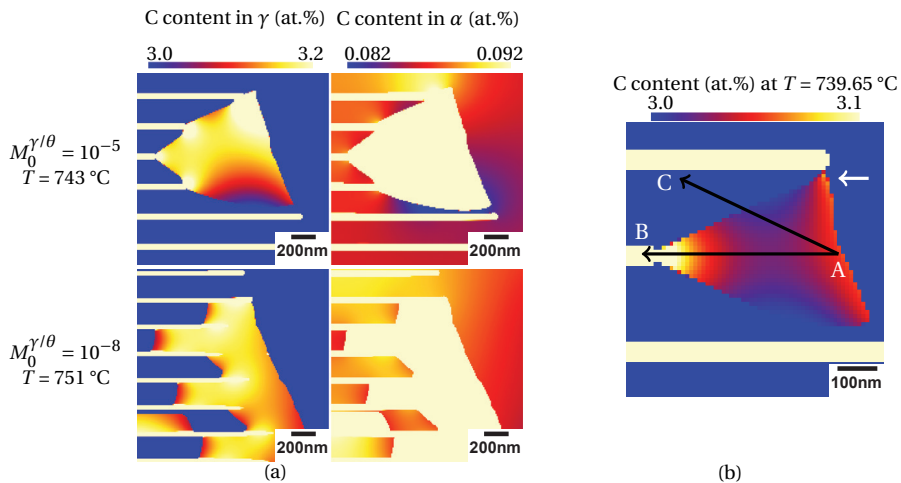


Figure 3.8: (a) Carbon content in austenite ( $\gamma$ ) and ferrite ( $\alpha$ ) for highest and lowest  $M_0^{\gamma/\theta}$  ( $\text{m}^4\text{J}^{-1}\text{s}^{-1}$ ); (b) Carbon content in  $\gamma$  at  $T = 739.65\text{ }^\circ\text{C}$  for simulation with  $M_0^{\gamma/\theta} = 10^{-5}\text{ m}^4\text{J}^{-1}\text{s}^{-1}$ .

On the other hand, if the lowest  $M_0^{\gamma/\theta}$  is considered, the austenite front has a flat shape. In this case, the front growth is compromised as the rate of cementite dissolution is lower than the formation rate of austenite from ferrite, leading to the carbon source (cementite) being located behind the austenite growth front. Also in Figure 3.8, the carbon content in  $\alpha$  is depicted. While a slight enrichment of  $\alpha$  is seen for both mobilities, a bigger variation is seen for the higher mobility.

To have a better insight into the carbon distribution behavior in austenite during growth, the carbon concentrations at  $\gamma/\alpha$  and  $\gamma/\theta$  interfaces were analyzed for the simulation with high  $\gamma/\theta$  mobility ( $M_0^{\gamma/\theta} = 10^{-5} \text{ m}^4\text{J}^{-1}\text{s}^{-1}$ ). Figure 3.8b displays the carbon content in  $\gamma$  at  $T = 739.65 \text{ }^\circ\text{C}$ . As can be seen, the austenite nucleus has mainly grown along the cementite lamella at which it nucleated and laterally towards the neighboring pearlitic ferrite. Above this temperature, the growing austenite encounters an additional carbon source in the adjacent cementite lamella at the top right-hand corner of Figure 3.8b, highlighted with a white arrow. This leads to  $\gamma$  being saturated in carbon at this location and consequently changes the carbon concentration gradients within  $\gamma$ .

Due to the complex topology of the pearlitic structure with additional carbon sources playing a role in the austenite growth at different time steps, a representation of the overall growth of  $\gamma$  is impossible. For this reason, two line profiles are chosen to represent the local behavior of  $\gamma/\theta$  (A-B line) and  $\gamma/\alpha$  (A-C line) interfaces, represented by black arrows in Figure 3.8b.

Figure 3.9a presents a comparison between the carbon content in equilibrium and the carbon content obtained via simulation at the  $\gamma/\theta$  and  $\gamma/\alpha$  interfaces. The equilibrium carbon contents ( $C_{eq}^{\gamma/\theta}$  and  $C_{eq}^{\gamma/\alpha}$ ) are calculated based on the linearization data of the Fe-C-Mn phase diagram provided at the onset of the MICRESS simulation. The plotted interface values consider the carbon content of the last austenite point prior to the diffuse interface region along both A-B ( $C^{\gamma/\theta}$ ) and A-C ( $C^{\gamma/\alpha}$ ) lines for different temperatures. Figure 3.9b shows the interface velocity of both  $\gamma/\theta$  (A-B) and  $\gamma/\alpha$  (A-C) interfaces as a function of temperature. The overall velocity of the  $\gamma/\theta$  interface is much higher than the one observed in the case of  $\gamma/\alpha$  due to its proximity to the carbon source.

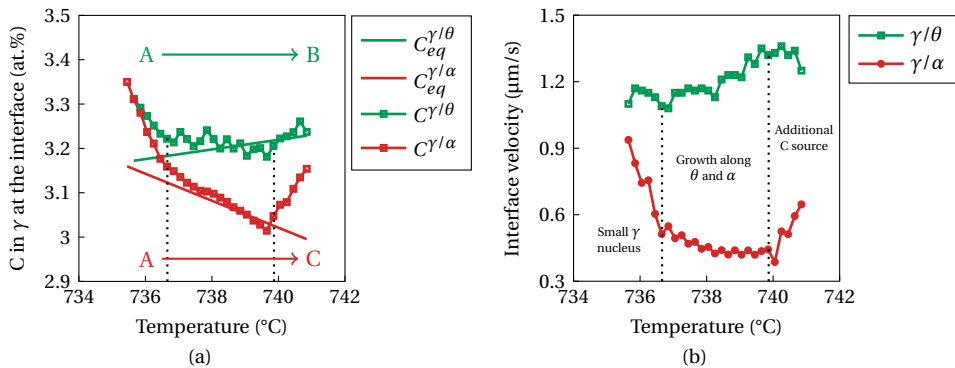


Figure 3.9: (a) Carbon concentration in  $\gamma$  at the  $\gamma/\theta$  interface along A-B line (see Figure 3.8b) and  $\gamma/\alpha$  interface along A-C line (see Figure 3.8b) and the respective equilibrium values as a function of temperature; (b) Velocity of  $\gamma/\theta$  (along A-B line) and  $\gamma/\alpha$  (along A-C line) interfaces as a function of temperature. The simulation considered  $M_0^{\gamma/\theta} = 10^{-5} \text{ m}^4\text{J}^{-1}\text{s}^{-1}$ .

As can be seen from Figure 3.9a, the austenite is supersaturated in carbon at both  $\gamma/\theta$  and  $\gamma/\alpha$  interfaces up to approximately 737  $^\circ\text{C}$ . This is due to the small size of the  $\gamma$  nucleus in the vicinity of  $\theta$  (carbon source) leading to local enrichment of  $\gamma$  and additional driving force for the interface movement of austenite into the low-carbon ferrite. For this reason, a higher interface velocity is observed for the  $\gamma/\alpha$  interface at this temperature range and it decreases with the growth of the austenite nucleus and the consequent decrease of carbon

content towards equilibrium.

From 737 °C to approximately 739 °C, the carbon content at both interfaces stabilizes around the equilibrium value as the austenite grows both along the cementite (carbon source) and ferrite (low in carbon). In this region, the interface is expected to move at a rate controlled by carbon diffusion within the austenite and the velocity stabilizes. However, this behavior changes for temperatures above 739 °C where an increase of the carbon content and the velocity of the  $\gamma/\alpha$  interface are observed.

Figure 3.10a shows the carbon content in austenite at 739.45 and 739.85 °C with D-E and D'-E' lines located parallel to the moving  $\gamma/\alpha$  interface between two cementite lamellae. The carbon profiles along these two lines are plotted in Figure 3.10b. At 739.45 °C,  $\gamma$  is enriched in carbon at the vicinity of point D (carbon source) and a gradual decrease of carbon is seen towards point E due to lack of time for the carbon to homogenize in  $\gamma$ . However, at 739.85 °C, both D' and E' regions are enriched in carbon. At this point, the austenite reaches an additional carbon source at the neighboring cementite lamella. This carbon diffuses towards the low-carbon austenite near the  $\gamma/\alpha$  interface, causing an increase of the carbon content at the  $\gamma/\alpha$  interface, see Figure 3.9a. As a result, an increase in the velocity of the  $\gamma/\alpha$  interface is observed, as shown in Figure 3.9b.

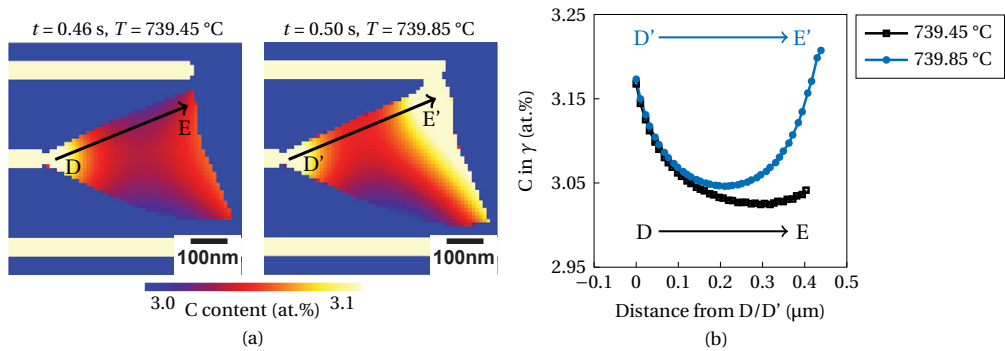


Figure 3.10: (a) Carbon content in  $\gamma$  at 739.45 °C and 739.85 °C for simulation with  $M_0^{\gamma/\theta} = 10^{-5} \text{ m}^4\text{J}^{-1}\text{s}^{-1}$ . (b) Carbon profile in  $\gamma$  across D-E line ( $T = 739.45$  °C) and D'-E' line ( $T = 739.85$  °C).

#### EFFECT OF $\gamma/\alpha$ MOBILITY

In this section, the effect of  $\gamma/\alpha$  mobility on the transformation kinetics is presented. To do so, the  $\gamma/\theta$  mobility was considered equal to  $10^{-6} \text{ m}^4\text{J}^{-1}\text{s}^{-1}$  while variations of  $\gamma/\alpha$  interface mobility were implemented. It was noted that one order of magnitude changes in  $\gamma/\alpha$  mobility lead to a substantial increase in the rate of phase transformation and consequently impossibility to fit the experimental curves. For this reason, lower variations of this interface mobility are assumed for this study.

In Figure 3.11a the simulated and experimental austenite fraction as a function of temperature is presented. With a low  $\gamma/\alpha$  interface mobility it is possible to accurately fit the experimental curve, while high mobility imposes difficulties in fitting the curve, mainly at later stages of the phase transformation. Besides that, with a low mobility it is possible to properly capture the change in kinetics during pro-eutectoid ferrite transformation. In the pro-eutectoid ferrite region, only  $\gamma/\alpha$  interfaces are present. By reducing the  $\gamma/\alpha$  interface

mobility, the movement of this interface is limited and will occur at a lower rate than  $\gamma/\theta$  interface motion. Consequently, the growth rate into the pro-eutectoid ferrite will be lower than in the pearlite region where both interfaces are present, leading to a good correspondence with the experimental kinetics. The nuclei density corresponding to each condition is shown in Figure 3.11b. A much higher nuclei density is needed if lower  $\gamma/\alpha$  mobilities are considered. This reflects the effect of this mobility on the growth kinetics of austenite as the grains will grow at a lower rate and consequently, new nuclei are allowed to form.

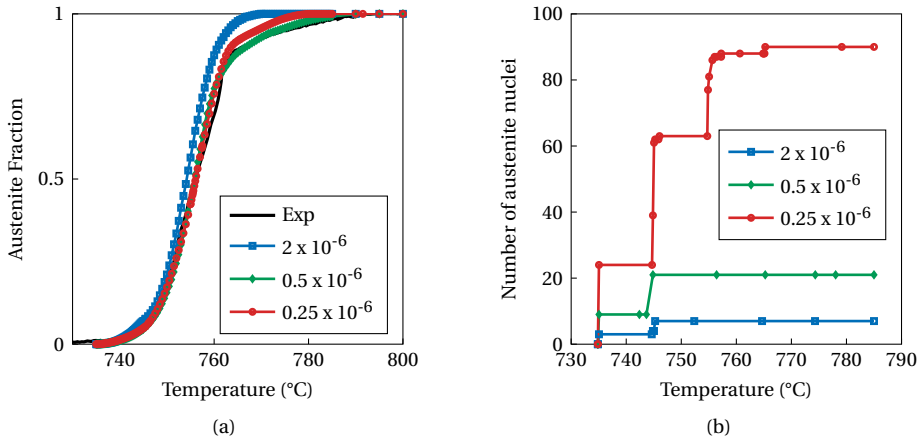


Figure 3.11: (a) Austenite phase fraction as a function of temperature obtained experimentally (black solid curve) and via phase field simulation with different pre-exponential factors for  $\gamma/\alpha$  mobility (colored lines with symbols) and (b) Number of austenite nuclei as a function of time for each simulation with different pre-exponential factors of  $\gamma/\alpha$  mobility ( $\text{m}^4\text{J}^{-1}\text{s}^{-1}$ ).

The changes in the microstructural features are seen in Figure 3.12. In the case where the  $\gamma/\alpha$  mobility is slightly higher than the  $\gamma/\theta$  mobility, the flat growth front is observed. On the other hand, lower values of  $\gamma/\alpha$  mobility relative to  $\gamma/\theta$  mobility cause the sharp front growth morphology with the cementite being consumed at a considerably higher rate than the growth into the pearlitic ferrite. As the final austenite grains are related to the nuclei density, more polygonal shapes are seen for higher  $\gamma/\alpha$  mobilities in which the nuclei density is low.

In summary, the mobility of both  $\gamma/\theta$  and  $\gamma/\alpha$  interfaces influence the kinetics and morphology of austenite formation. In the real material, variations in mobility occur due to interface characteristics such as crystallographic orientation and local chemical composition. This is why different growth morphologies are seen in the real material (Figure 3.4). The combination of these factors can lead to different microstructural features during austenite growth.

#### SIMULATION WITH $200\text{ }^\circ\text{Cs}^{-1}$

This section presents the results obtained for a simulation with a heating rate of  $200\text{ }^\circ\text{Cs}^{-1}$ . The simulation is set to start at  $720\text{ }^\circ\text{C}$  which is below the expected  $A_{c1}$  temperature. The mobility values of  $\gamma/\alpha$  and  $\gamma/\theta$  interfaces are  $3.5 \times 10^{-5}\text{ m}^4\text{J}^{-1}\text{s}^{-1}$ . A higher mobility is needed to fit the experimental curve for higher cooling rates. This increase is required because MICRESS input mobility is not a representation of the intrinsic mobility of the interface

but rather an effective parameter that incorporates the effects of various model simplifications [98]. This effective mobility can vary with the evolution of phases involved and various aspects have been reported to affect the effective mobility in MICRESS, such as heating/cooling rates, grid size and space dimension of the simulations (2D or 3D) [98, 100, 101]. As the interface mobilities are assumed to be equal, the growth morphology shows a flat growth, see Figure 3.13a.

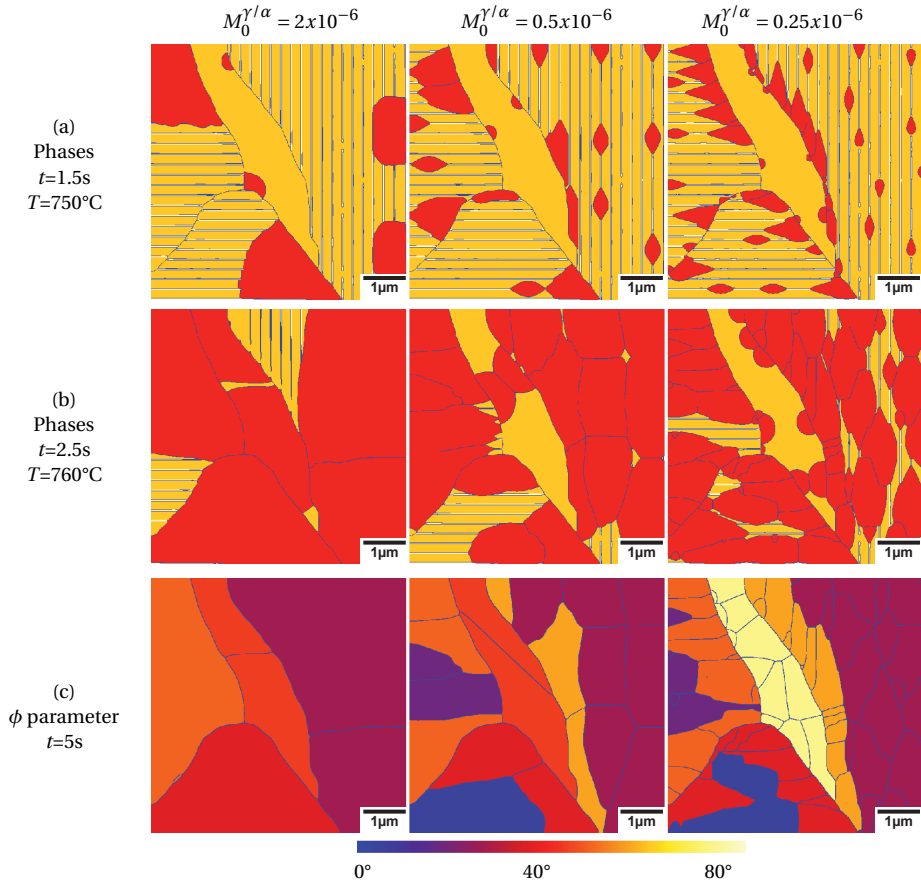


Figure 3.12: (a,b) Simulated microstructural evolution at  $t = 1.5$  s and  $2.5$  s for different  $\gamma/\alpha$  pre-exponential factors ( $M_0^{\gamma/\alpha}$ ) with red grains representing the austenite phase. (c)  $\phi$  parameter for  $t = 5$  s (fully transformed microstructure) for different  $M_0^{\gamma/\alpha}$  ( $\text{m}^4\text{J}^{-1}\text{s}^{-1}$ ), with colors indicating the  $\phi$  parameter (see section 3.4.2).

In Figure 3.13, the experimental and simulated phase fractions are compared. As explained in section 3.3, the experimental phase fraction at high heating rates is affected by the thermal gradient of the dilatometry sample. However, it can still provide an estimation of the kinetics of the phase transformation at the later stages of transformation as depicted in Figure 3.13c. At first glance, it appears that the simulation occurs with higher kinetics than the experiments. As indicated in section 3.3, a temperature lag of  $11^\circ\text{C}$  is estimated for experiments with  $200^\circ\text{C}\text{s}^{-1}$  which is the same order of magnitude as the difference observed



between the simulated and experimental curves (16 °C).

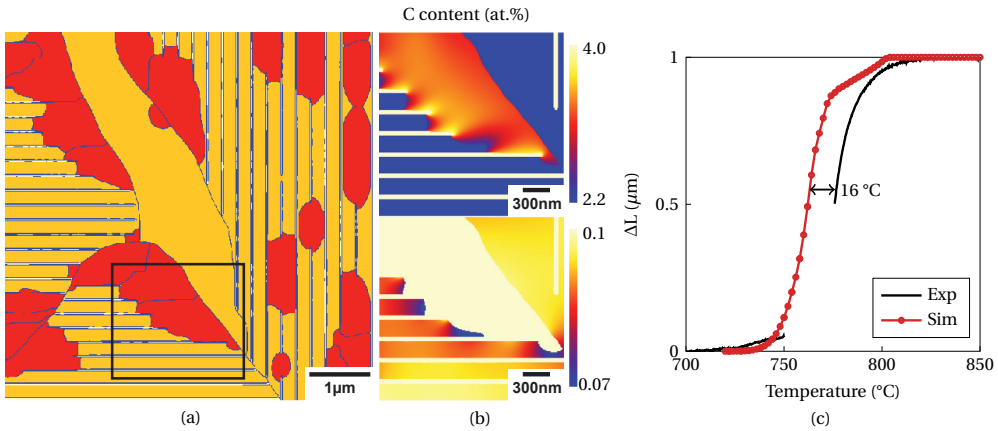


Figure 3.13: (a) Phase evolution and (b) carbon content in austenite (top) and ferrite (bottom) of a selected area (black square) for simulation considering  $200\text{ }^{\circ}\text{C s}^{-1}$  at  $t = 0.19\text{ s}$  ( $758\text{ }^{\circ}\text{C}$ ). (c) Austenite fraction as a function of temperature obtained experimentally and via simulation at a heating rate of  $200\text{ }^{\circ}\text{C s}^{-1}$ .

A stronger carbon concentration gradient is observed both in austenite and ferrite (Figure 3.13a) than obtained for simulations with lower heating rate (Figure 3.8a). This is caused by the shorter time for carbon diffusion in the microstructure due to the very high heating rate. As previously mentioned, carbon concentration gradients influence the movement of the  $\gamma/\alpha$  and  $\gamma/\theta$  interfaces as regions with high carbon content account for an additional driving force for interface movement. These carbon content inhomogeneities can lead to the formation of different microstructures during cooling.

For example, the martensite start temperature is related to the carbon content in the parent austenite which means that martensitic transformation can occur at different temperatures during cooling. Moreover, if the local carbon content leads to the martensite start temperature being below room temperature, then austenite will be stable at room temperature after cooling, characterizing the so-called retained austenite in these regions. Furthermore, the carbon content determines the strength of the martensite. These effects become even more important if several partial austenitization and quenching steps are considered, such as rails are most likely subjected to in field conditions.

### 3.5. CONCLUSIONS

The combination of experimental and phase-field simulation analysis of the austenite formation from a pearlitic microstructure was presented in this chapter. The results show that:

- Austenite nuclei formed at heating rates of  $10$  and  $200\text{ }^{\circ}\text{C s}^{-1}$  show similar growth morphologies. The main microstructural aspects observed are flat and sharp austenite front, nucleation at colony boundaries and within the colonies, and preferential growth towards a pearlite colony.
- Phase-field simulations of austenite growth from a pearlitic microstructure capture these different morphological features depending on the values of the  $\gamma/\alpha$  and  $\gamma/\theta$

interface mobilities. A flat growth front with undissolved cementite is obtained when  $M^{\gamma/\theta}$  is lower than  $M^{\gamma/\alpha}$  while a sharp front is seen for higher  $M^{\gamma/\theta}$  values.

- $M^{\gamma/\alpha}$  has a stronger influence on the kinetics of pearlite to austenite transformation than  $M^{\gamma/\theta}$ . Lower  $M^{\gamma/\alpha}$  reproduces the exact change in kinetics observed at the later stages of pearlite to austenite transformation observed experimentally. At this point the growth of austenite is controlled by the rate of pro-eutectoid ferrite dissolution which is much lower than pearlite due to lack of carbon.
- $M^{\gamma/\theta}$  mainly affects the growth morphology of austenite. This mobility dictates the rate of cementite dissolution and consequently the carbon source for austenite growth.
- Carbon concentration gradients are observed in both austenite and ferrite for simulations with both 10 and 200 °Cs<sup>-1</sup>. This gradient is much stronger for higher heating rates, which is due to the lack of time for carbon to homogenize in austenite. These carbon gradients can lead to inhomogeneities in the microstructure during intercritical heating and cooling such as rails are subjected to in the field.

# 4

## MICROSTRUCTURE AND MECHANICAL RESPONSE OF FIELD AND LASER-INDUCED WHITE AND BROWN ETCHING LAYERS

4

*The primary objective of this chapter is to comprehend the variations in microstructure and hardness associated with the occurrence of White and Brown Etching Layers (WEL and BEL) on the surface of railway steels. To achieve this, the study compares WELs and BELs that formed during wheel and rail contact in field conditions with those formed during laser heating. The laser treatment involved two passes at the same location but at different speeds, as can be expected for railway steel in application, resulting in distinct heat-affected zones with WEL and BEL characteristics. The microstructural features of each sample were examined using Light Optical Microscopy and Scanning Electron Microscopy. Furthermore, nanoindentation mappings were performed to compare the mechanical characteristics of the WEL and BEL formed in field conditions with those induced by the laser treatment.*

## 4.1. INTRODUCTION

White Etching Layer (WEL) and Brown Etching Layer (BEL) are usually observed microstructural features that occur on the surface of railway steels [38, 102]. This nomenclature is related to the white and brown contrast of these layers in a light optical microscope after etching with Nital 2%. These layers have been extensively studied in the literature due to their detrimental character to the rail's service life. WEL and BEL have been associated with preferential sites for crack nucleation and propagation mainly because of their brittle nature when compared with the pearlite matrix [31].

Much attention has been given to the study of the different microstructural features and mechanical properties of WEL. From these studies, two main hypotheses have been proposed to explain the formation of these layers at the rail surface. The first one claims that during wheel and rail contact, the extreme loading conditions induce severe plastic deformation of the pearlite matrix, leading to grain refinement and cementite dissolution [28, 43, 44, 46, 103, 104]. However, this hypothesis was questioned due to the discovery of retained austenite within the WEL as well as no sign of extreme plastic deformation found associated with WEL in some cases. For this reason, a second theory was proposed which suggests the formation of martensite with high dislocation density during rapid heating of the rail surface due to frictional heat generated by wheel and rail contact and subsequent rapid cooling [14, 23, 37, 38, 48].

None of these hypotheses has been widely accepted due to the different and complex service conditions to which the rails are subjected. Therefore, efforts have been made to reproduce the formation of WEL and BEL under laboratory conditions [32, 38, 41, 105]. However, the complex loading and short time of each individual wheel and rail contact impose great difficulty when trying to reproduce the exact same conditions in a laboratory setup.

Wu et al. [41] considered the simultaneous deformation and fast heating and quenching with the results supporting the formation of WEL via martensite transformation. The nanometer grain size commonly observed within the WEL as well as very high hardness were obtained via severe plastic deformation [46]. Additionally, laser heating has been used to simulate the ultrafast heating of the rail surface leading to the formation of WEL in different steel grades [106]. In these studies, only WEL was detected after laser heating but no presence of BEL.

Recent studies have focused on the characterization of BEL. The BEL also shows a sharp interface with the pearlite matrix and is often observed to be an intermediate layer between the pearlite and WEL. Despite being typically associated with regions containing WEL, regions containing only BEL have also been identified at the rail surface [107]. Li et al. [107] suggested that the Brown Etching Layers (BELs) are mainly composed of tempered martensite and formed subsequent to the formation of the White Etching Layers (WELs). A similar idea was proposed by Kumar et al. [37] who characterized the BEL as consisting of tempered martensite, secondary carbides, partially dissolved cementite, and retained austenite due to thermomechanical processes. In another study, Messaadi et al. [51] identified the presence of globular bainite in the microstructures of the BELs.

This chapter will focus on the comparison between two samples from the same railway steel grade (MHH) containing WEL and BEL. These layers were formed through two distinct methods: the first sample's WEL/BEL layers were created during service as a result of contact between wheels and rail, while the second sample's WEL/BEL layers were intentionally generated in a controlled laboratory environment using laser heating. These two sets of

layers are analyzed by Scanning Electron Microscopy (SEM) and nanoindentation.

## 4.2. MATERIAL AND METHODS

The material analyzed in this chapter is the pearlitic MHH railway steel. The chemical composition of this steel is Fe - 0.78 C - 0.93 Mn - 0.65 Si - 0.53 Cr (wt.%). This particular rail steel grade is heat-treated during manufacturing, leading to a finer pearlitic microstructure at the rail's surface than in standard air-cooled pearlitic rail steels. Consequently, improved resistance to wear and rolling contact fatigue is achieved. No information regarding the loading history of this rail is available. The first sample contains WEL/BEL layers that formed during service as a result of wheel and rail contact and it was obtained by sectioning a small portion of the rail's surface. The second sample was taken from the unaffected bulk region of the rail head from the same rail piece to obtain a sample containing only the original pearlitic matrix. After sectioning, the piece was subjected to controlled laboratory laser heating to form WEL and BEL layers.

The laser heat treatment was done using a TruDisk 8002 laser with a wavelength of 1030 nm. The rail-surface heat treatment consisted of two laser passes at the exact same location of the sample with different speeds, as can be expected in field conditions: the first laser pass with a speed of 20 mm/s and the second with a speed of 80 mm/s. The laser power was set to 160 W with a laser beam diameter of 0.6 mm in both cases.

Both samples were ground and polished using a standard metallographic procedure followed by chemical etching with Nital 2% to reveal the microstructure. The microstructural features were observed using Light Optical Microscopy (LOM) and Scanning Electron Microscopy (SEM). The samples were then repolished to remove the chemical etching and obtain a mirror-like surface prior to nanoindentation measurements.

Nanoindentation was performed on a KLA iNano nanoindenter using a Berkovich tip geometry in the WEL/BEL region of both samples. The measurements were done in the CSM (Continuous Stiffness Measurement) mode. This is a dynamic method, which uses a superimposed oscillation of the tip to measure stiffness continuously during the loading. The measurements were performed in displacement control with a maximum displacement depth of  $97.0 \pm 0.5$  nm with a distance of 4  $\mu$ m between the indents.

## 4.3. RESULTS

### 4.3.1. MICROSTRUCTURAL CHARACTERIZATION

The micrographs shown in this section consider the cross-section region of the rail piece close to the running surface such that the running direction of the trains is perpendicular to the observed plane. The red rectangles in Figure 4.1, 4.2, and 4.3 represent the locations where the nanoindentation mapping was performed. The nanoindentation results will be presented and discussed in Section 4.3.2.

#### FIELD WEL/BEL

The analyzed surface area of the MHH railway steel reveals the presence of WEL and BEL resulting from field operation at multiple locations. This study focuses on two distinct regions to highlight the characteristics of these two layers. The first region exclusively contains a WEL (Figure 4.1a), whereas the second region exhibits both WEL and BEL stacked on top of each other (Figure 4.2a).

Figure 4.1 presents the LOM and SEM micrographs of the first analyzed region of the field sample after etching with Nital 2%. As can be seen in Figure 4.1a, the rail surface contains a featureless WEL measuring approximately 35  $\mu\text{m}$  in thickness. A sharp interface separates the WEL from the pearlite matrix underneath it. The brownish etched pearlite matrix shows no sign of extreme plastic deformation which would be characterized by the flattening of the pearlite colonies and by the lamellae orientation.

High-magnification SEM micrographs of the top and bottom of the WEL region and at the WEL/matrix interface are shown in Figure 4.1(b-d), respectively. As expected, very few features can be seen in the WEL due to its low reactivity to the chemical etchant. At the interface between WEL and pearlite matrix, some lamellar features (black lines in Figure 4.1d) are observed within the WEL which appear as a continuation of the pearlitic cementite lamellae, suggesting an incomplete dissolution of the cementite. Lamellar-like features, which have been reported in the literature as "ghost-pearlite" [64], are also found at the bottom of the WEL (Figure 4.1c) but they are less evident at the top of the WEL (Figure 4.1b).

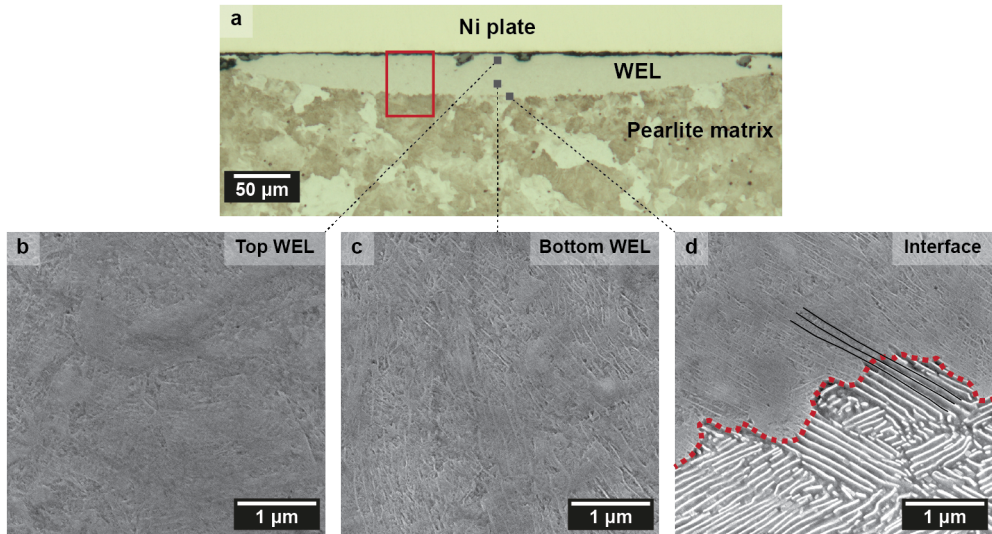


Figure 4.1: (a) Light optical micrograph of field WEL found in MHH steel with red rectangle highlighting the location where nanoindentation was performed; SEM micrographs at the (b) top of the WEL, (c) bottom of the WEL and (d) interface between WEL and pearlite matrix with the interface highlighted by a dashed red line.

The second region of the field sample accounted for the presence of WEL and BEL on top of the pearlite matrix, see the optical micrograph in Figure 4.2a. In this case, the WEL is present along the surface with the BEL underneath it, followed by the pearlite matrix. Although the thickness of these two layers varies along the cross-section, at the region of the nanoindentation (red rectangle) the WEL and BEL thicknesses are approximately 20 and 30  $\mu\text{m}$ , respectively.

Also in this case, the high magnification SEM image of the WEL (Figure 4.2b) has low contrast due to the high resistance to chemical etching with Nital. Unlike the previous WEL analyzed in this section, no sign of lamellar features is observed in this WEL. The BEL region shows a complex and heterogeneous microstructure. The brown contrast is strongest close to the WEL/BEL interface (top of the BEL) and is lighter brown close to the pearlite matrix,

which is bound to be due to differences in the microstructural characteristics of this layer.

At the top of the BEL (Figure 4.2c), some lath-like features are observed with carbide precipitates between these laths. Additionally, this region accounts for fully transformed regions characterized by high resistance to chemical etching, which are seen to contain no trace of parent cementite lamellae. Besides that, only a few regions with partially dissolved parent cementite are present at the top of the BEL. However, the fraction of these regions increases with depth. At the interface between BEL and pearlite, a continuation of the pearlite lamellae towards the BEL is evident, see Figure 4.2e.

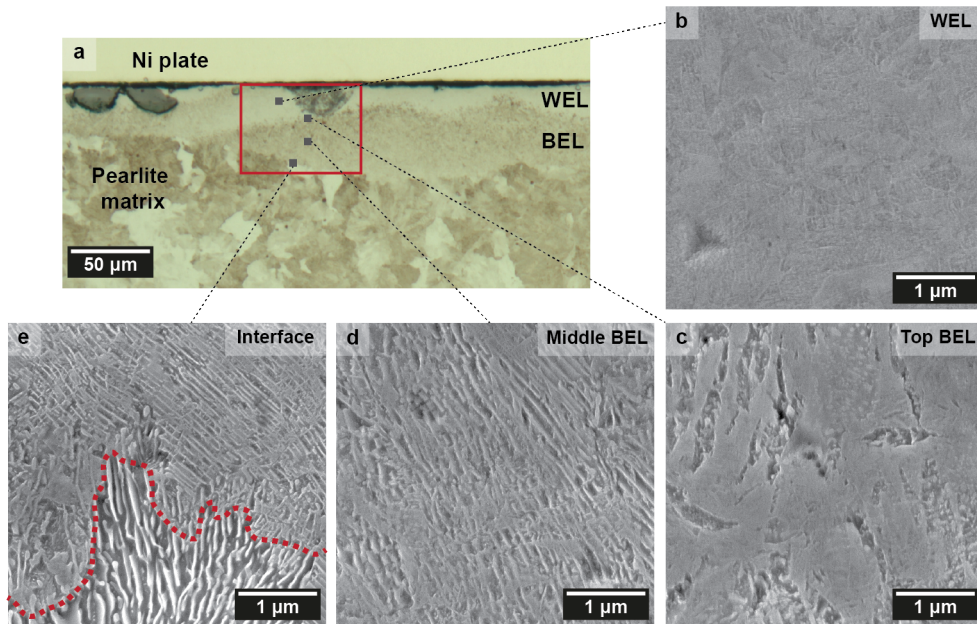


Figure 4.2: (a) Light optical micrograph of field WEL and BEL found in MHH steel with red rectangle highlighting the location where nanoindentation was performed; SEM micrographs at the (b) WEL, (c) top of the BEL, (d) center of the BEL and, (e) interface between BEL and pearlite matrix with the interface highlighted by a dashed red line. The dark semi-circular region within the red rectangle is a moisture stain that formed during sample preparation.

#### LASER WEL/BEL

Laser heat treatment was used to induce WEL and BEL formation during rapid heating and cooling in a sample cut out from the bulk of the same MHH steel. The laser heating consisted of two consecutive passes at 20 mm/s and 80 mm/s at the same location aiming at achieving WEL and BEL formation due to the differences in the heat-affected zone dimensions of the passes.

Figure 4.3a shows the LOM image of the cross-section of the laser-treated sample after chemical etching with Nital 2%. The laser bead dimensions after the second pass are 520 μm width and 300 μm depth, which is much larger than the usual WEL/BEL layers formed due to wheel/rail contact. The laser treatment also caused the melting of the central portion of the white region and for this reason, the analysis will be done in the region below the dashed red line in Figure 4.3a to avoid the previously molten material.

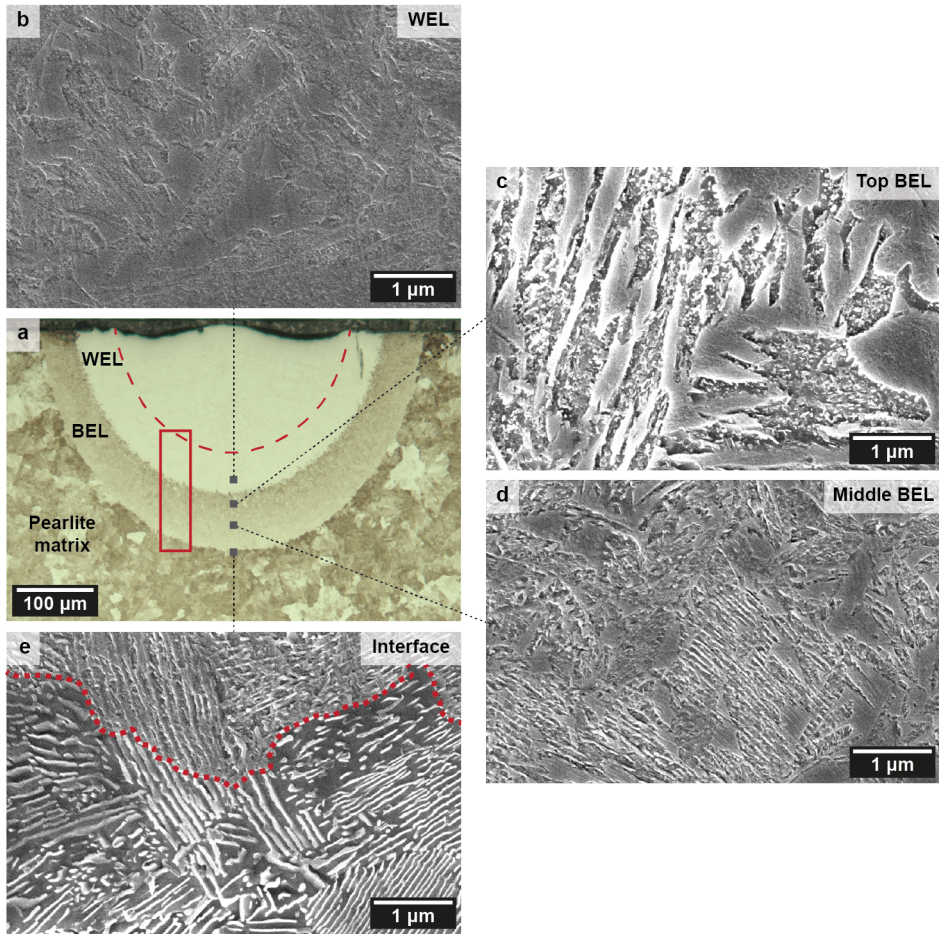


Figure 4.3: (a) Light optical micrograph of WEL and BEL formed through laser heating of MHH steel with red rectangle highlighting the location where nanoindentation was performed; SEM micrographs at the (b) WEL, (c) top of the BEL, (d) center of the BEL, and (e) interface between BEL and pearlite matrix with the interface highlighted by a dashed red line.

Despite the different dimensions, a first analysis of the optical micrograph shows two clear similarities between the laser and the field WEL and BEL. The first is the sharp character of the two interfaces (WEL/BEL and BEL/pearlite). The second is the heterogeneous etching response within the BEL showing a darker region close to the WEL and becoming lighter brown closer to the pearlite matrix.

The SEM micrographs at different depths are presented in Figure 4.3b-e. As seen, the laser WEL shows no trace of parent lamellar structure or visible undissolved carbides. The microstructure of the top of the laser BEL (Figure 4.3c) accounts for the presence of laths with some possible carbide precipitates within these laths. On the other hand, the BEL microstructure changes with depth (Figure 4.3d) to what appears as partially transformed pearlite with some traces of the parent cementite lamellae as well as some featureless regions resembling the laser WEL microstructure. Both laser WEL and BEL microstructures



are similar to the ones observed in the field WEL and BEL shown in Figure 4.2.

### 4.3.2. NANOINDENTATION

Figure 4.4 depicts the three nanoindentation mappings in the regions indicated by the red rectangles in Figure 4.1-4.3 along with their corresponding dark-field optical micrograph images showing the indent locations. The nanoindentation spacing of  $4\ \mu\text{m}$  was kept the same for all measurements but the number of points varied depending on the available area of each layer.

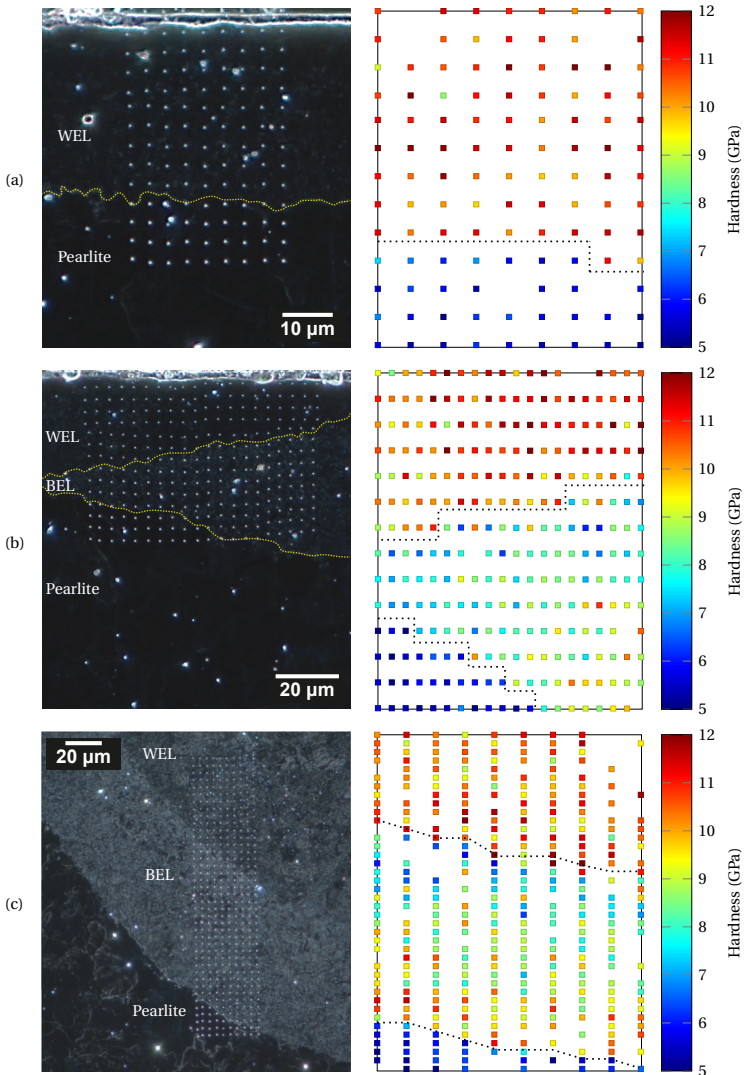


Figure 4.4: Dark field optical micrograph (left) of nanoindentation location with the nanohardness mapping (right) for (a) field WEL/pearlite sample, (b) field WEL/BEL/pearlite sample, and (c) laser WEL/BEL/pearlite sample. Dotted lines represent the interfaces between the different layers.

The nanoindentation measurements were considered reliable for observed Young's modulus values ranging from 195 to 250 GPa. Any missing data points in the nanoindentation mappings indicate indentations that were considered invalid and were excluded from the analysis in this chapter. The remaining data was considered adequate for determining the local nanoindentation response of each layer.

Figure 4.4a and b display the hardness mappings of the field samples. It is evident that the field WEL exhibits the highest hardness values, ranging approximately from 9.7 to 12 GPa. The field BEL is softer than the field WEL, with values ranging from 7 to 9 GPa. The pearlitic matrix exhibits the lowest hardness values, falling below 7 GPa.

The sample featuring the WEL/BEL formed through laser heating (Figure 4.4c) exhibits similar hardness variations. Similar to the field WEL, the laser WEL shows hardness values ranging from 9.5 to 12 GPa. Within the BEL, a hardness gradient is observed, with a softer region (7 to 8 GPa) near the BEL/WEL interface (top BEL), followed by an increase in hardness to values between 8 and 10 GPa closer to the BEL/pearlite interface. Also in this case, the pearlite matrix exhibits lower hardness values, below 7 GPa.

#### 4.4. DISCUSSION

From the microstructural analysis, two clear characteristics are observed in the field and laser-induced WEL and BEL: the sharp interface with the pearlite matrix and the absence of severely deformed pearlite underneath the layers. However, one difference lies in the dimensions of the WEL and BEL features between the laser-induced and field samples, with the former exhibiting larger dimensions due to inevitable differences in heating and cooling.

In field conditions, the wheel and rail contact not only heats up but also plastically deforms the rail surface where WEL and BEL are found, causing grain refinement of these layers. On the other hand, in cases like the laser-induced WEL and BEL, where plastic deformation is absent, grain refinement does not occur. Therefore, the results support the idea that the WEL produced in field conditions primarily forms due to a thermomechanical process, even when severe deformation of the pearlite matrix near the field WEL and BEL is not observed. If the WEL would have been formed exclusively due to severe plastic deformation, a gradient of deformed substructures especially in the pearlite underneath the WEL should have been present [38].

Additionally, the field WEL shows less contrast than the BEL and pearlite, with some traces of the parent lamellar structure still observable in some regions. It is therefore likely that Mn did not homogenize in the WEL due to ultrafast heating leading to the so-called "ghost pearlite". During ultrafast heating, Mn does not have enough time to diffuse out of the Mn-rich regions (cementite) and homogenize in austenite. Consequently, high-Mn regions where previously cementite lamellae were present remain in the austenite structure (and martensite after cooling), leading to different etching properties. The fraction of these lamellar features in the field WEL increases with depth. This is consistent with the temperature gradients with depth expected during the heating of the rail surface [37], where regions further from the rail surface experience a lower temperature rise, retarding the complete dissolution of cementite lamellae.

The microstructural analysis of the laser-induced WEL indicates that, unlike the field WEL, this layer is homogeneous and shows no traces of the parent pearlite microstructure. This suggests that the laser treatment used in this paper was sufficient to fully transform the

region with the white contrast.

Moreover, the results show that both field and laser-induced BEL does not have a uniform microstructure along its depth. The topmost region of the BEL (close to the WEL/BEL interface) shows a quite complex microstructure with some partially dissolved pearlite, a lath-like structure, undissolved carbides, and fully transformed regions resembling the WEL microstructure. On the other hand, the region close to the BEL/pearlite interface accounts for fragmented cementite regions as well as thinned cementite, suggesting partial dissolution/transformation of the pearlite matrix. At the interface between the BEL and pearlite, a continuation of the cementite lamellae from the pearlite matrix into the BEL is also visible.

Similar characteristics for WEL and BEL have been previously reported in [37] where a detailed characterization of WEL and BEL layers was done in an R350HT steel. In that work, the authors correlated the different features to the carbon distribution in different layers and consequently the different stages of phase transformation. It was also proposed that the BEL consists of ferrite, partially dissolved parent cementite, tempered martensite with secondary carbides, and martensite/austenite islands.

The microstructural features of the WEL and BEL are very difficult to identify using only SEM due to their nanosized nature. Higher resolution techniques such as Electron Backscatter Diffraction, Transmission Electron Microscopy, and Atom Probe Tomography would contribute to the understanding of the distribution of chemical elements as well as the phases present. This would provide a more complete understanding of the actual microstructure of both WEL and BEL and consequently support their formation theory.

#### LASER TEMPERATURE PROFILE

A possible explanation for the effect of each laser passage at the rail surface is proposed based on the microstructural observations shown in section 4.3.1. As mentioned in section 4.2, the first laser pass (Figure 4.5a) was performed with a speed of 20 mm/s while the second laser pass (Figure 4.5b) was performed at a higher speed of 80 mm/s. It is important to point out that during the laser treatments, no BEL was produced after a single laser pass. Because of that, we can affirm that laser-induced BEL is formed as a consequence of the reheating of previously fully or partially transformed pearlite. This information serves as the basis for the hypothesis of laser-induced WEL and BEL formation presented in the following paragraphs.

Figure 4.5 presents a schematic of the temperature ranges at different depths during each laser pass. The heat-affected zone (HAZ) is divided into three different regions, representing temperature intervals reached at each laser pass. Region 1 consists of the possible melting pool after the first laser pass and will not be considered in this analysis. ThermoCalc software was used to calculate the equilibrium transformation temperatures for the MHH steel studied in this chapter. The results show that  $A_1$  and  $A_3$  are 739 °C and 797 °C, respectively.

A larger HAZ is obtained after the first pass (lower speed) due to the longer laser interaction with the sample surface, see Figure 4.5a. During the first laser pass, region 2 is assumed to have reached temperatures above  $A_3$  where the pearlite can fully transform into austenite and consequently martensite during fast cooling. However, the short interaction time between the laser and the material might not be sufficient to fully transform the initial pearlite into austenite even at temperatures above  $A_3$ . Thus, microstructural inhomogeneities are present within region 2 after the first laser pass, especially closer to the schematic dotted  $A_3$  line in Figure 4.5a. The temperature will decrease with depth along the HAZ, leading to

region 3 where temperatures fell between  $A_1$  and  $A_3$ . At this intercritical temperature range, only partial transformation of the pearlite occurs with the degree of pearlite transformation varying according to the local temperature rise. Below the solid line in Figure 4.5a, the maximum temperatures are expected to be below  $A_1$  as no transformation of the initial pearlitic microstructure is seen in the microstructural analysis reported in Figure 4.3e, also seen in Figure 4.5. It is possible that  $A_1$  was reached slightly deeper, but the time was too short to induce significant changes in the pearlite.

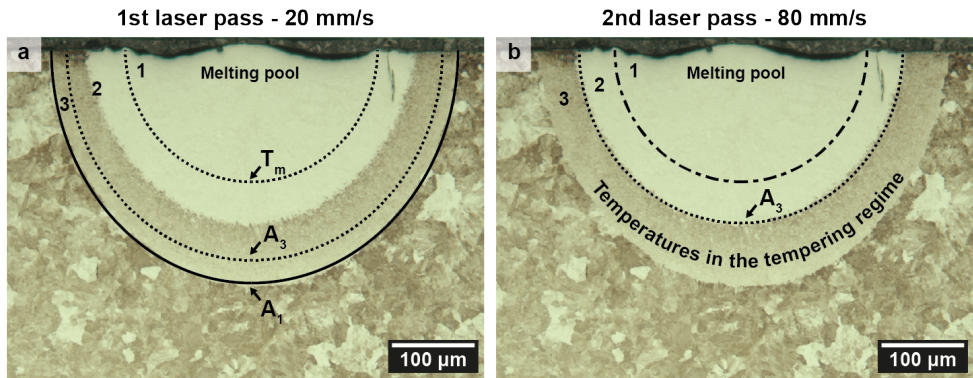


Figure 4.5: Schematic showing the estimated temperature ranges at different depths for each laser pass.

In summary, after the first laser pass, the upper part of region 2 is fully transformed to austenite and consequently martensite forms during fast cooling with the possible presence of retained austenite. The lower part of region 2 (closer to the  $A_3$  line) might account for the presence of microstructural inhomogeneities due to the low overheating and short time. Region 3, on the other hand, has a partially transformed microstructure which might contain regions with pearlite, martensite, and possibly retained austenite with the fraction of each phase varying according to the local temperature rise.

The second laser pass was performed at the exact same location as the first one. Therefore, the region affected by the laser heating in the first pass was subjected to additional reheating. Nevertheless, due to the higher speed of the second pass, the HAZ and consequently the molten pool resulting from the second pass are expected to be smaller than those from the first pass. However, as mentioned in the previous paragraph, region 1 (highlighted by a dash-dotted line in Figure 4.5b) will not be considered in this analysis due to melting during the first laser passage. As for region 2 in Figure 4.5b, it is safe to assume a reheating to temperatures above  $A_3$  as no sign of martensite tempering was seen in the laser-induced WEL (white contrast region). On the other hand, region 3 in Figure 4.5b (laser-induced BEL) is considered to be reheated to temperatures in the tempering regime during the second laser pass. The degree of tempering will vary with depth within the BEL region, being stronger closer to the interface between WEL and BEL (dotted  $A_3$  line). The boundary between BEL and pearlite was established during the first pass and does not indicate a specific temperature in the second laser pass.

Overall, the laser heat treatment performed in this study seems to adequately reproduce the microstructural features of thermally induced WEL and BEL in the steel, although the laser heat treatment parameters must be adjusted in order to optimize the final result by

avoiding melting and recreating WEL and BEL with similar thicknesses as seen in the field samples. Moreover, the temperature ranges at different depths provided in this chapter might be regarded as estimations and not fixed values at fixed locations. In reality, the fast heating rate not only can affect the actual position of the temperature intervals but also the austenitization temperature ranges of the material.

#### NANOINDENTATION

To gain deeper insight into the hardness distribution of the analyzed samples, histograms for each sample together with fitted normal distributions are shown in Figure 4.6. The average hardness of pearlite, BEL and WEL for field and laser samples based on the individual normal distributions in Figure 4.6 of each region is presented in Table 4.1.

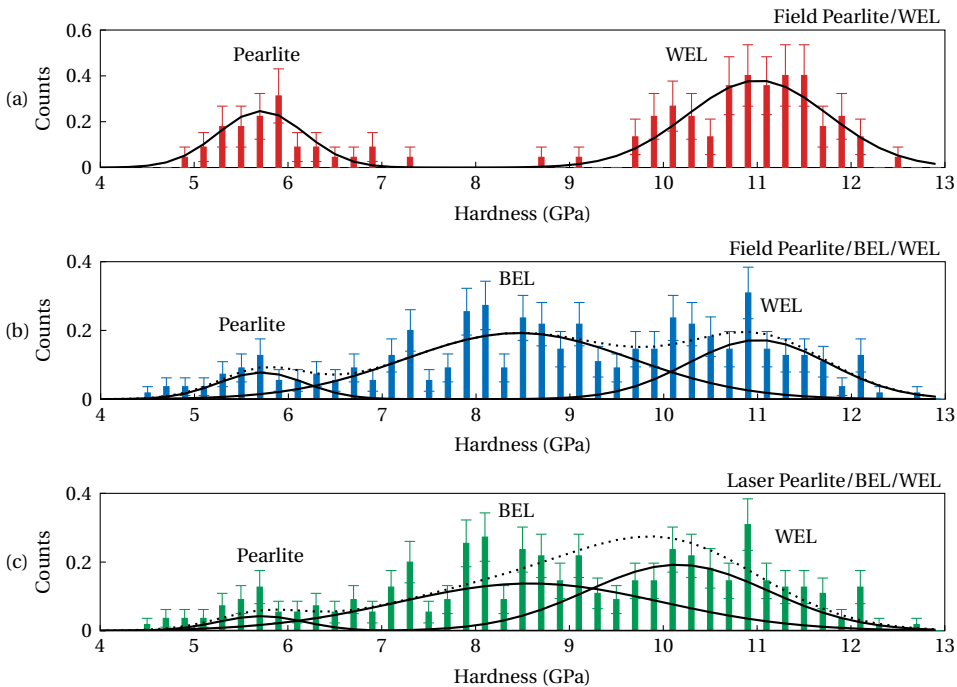


Figure 4.6: Histogram of the hardness with the normal distribution obtained for the three samples analyzed in this chapter: (a) field WEL/pearlite, (b) field WEL/BEL/pearlite, and (c) laser WEL/BEL/pearlite. The dotted line is the sum of the distributions given by the solid lines.

The first histogram (Figure 4.6a) refers to the field sample containing only WEL on top of the pearlite matrix. As can be seen, the hardness histogram accounts for two distinct clusters of data points. The first cluster exhibits hardness values ranging approximately from 4.5 to 7 GPa, while the second one spans from 9 to 13 GPa. As only WEL and pearlite are present in this sample, it can be inferred that the clusters correspond to the hardness of the pearlite matrix (lower hardness) and the field WEL (higher hardness). The normal distributions were therefore fitted separately.

Next, Figure 4.6b presents the results of the second field region with the intermediate BEL between the WEL and the pearlite matrix. Unlike in Figure 4.6a, the hardness distri-

bution in this region has many points with hardness values within the intermediate region between pearlite and WEL. In fact, the overall hardness distribution (dotted line) shows the presence of three distinct normal distributions. In this fit, the normal distributions for WEL and pearlite determined in Figure 4.6a were used. Thus, the BEL hardness of the field sample lies in the interval between the pearlite and the WEL hardness, as given by the middle peak.

Finally, Figure 4.6c shows the hardness distribution of the laser sample. Also in this case three peaks are expected, from the three microstructural zones in the material. Three peaks can be extracted from the overall distribution curve (dotted line), one at a lower hardness corresponding to the pearlite peak previously seen in field samples and two at a higher hardness comprising BEL and WEL hardness intervals from field samples.

As mentioned earlier, in the results section, a distinct hardness gradient is observed within the laser-induced BEL, see Figure 4.4c. To better visualize this behavior, the average hardness per BEL row of the field and laser BEL is plotted in Figure 4.7. As can be seen, both the field and laser BEL exhibit the lowest hardness close to the interface with WEL, followed by an increase in hardness with depth. The hardness increase is more evident for the laser BEL, which eventually reaches values similar to those of the hard WEL in the vicinity of the BEL/pearlite interface. This affects the hardness distribution of the laser sample, leading not only to a higher density of points between 9 and 10 GPa and thus to a slight increase in the average hardness of the laser-induced BEL with respect to the field BEL, see Table 4.1.

Table 4.1: Average hardness and standard deviation of field and laser pearlite, WEL and BEL based on the individual normal distributions of each region (Figure 4.6).

Sample	Average Hardness (GPa)		
	Pearlite	BEL	WEL
Field	$5.7 \pm 0.5$	$8.4 \pm 1.2$	$11.0 \pm 0.8$
Laser	$5.7 \pm 0.5$	$8.6 \pm 1.4$	$10.1 \pm 1.0$

Hardness gradients within the BEL have been previously documented by [107] during their investigation of R260Mn rail steel samples containing mixed layers of WEL and BEL. This softening phenomenon is consistent with the tempering of martensite, which might occur due to the range of temperatures experienced in these specific regions. Additional microstructural characterization techniques (e.g. Electron Backscatter Diffraction and Transmission Electron Microscopy) to characterize the tempered microstructure can confirm the hypothesis of BEL formation for the material studied in this chapter.

The comparison between the average hardness from the field and laser samples reported in Table 4.1 also shows a lower hardness for the laser-induced WEL when compared with the field WEL. This behavior can be linked to the absence of plastic deformation of the laser-induced WEL. Although it is not possible to quantify the grain sizes due to a lack of contrast in the WEL, one can see that the microstructural features are much smaller in the field WEL (Figure 4.1b and Figure 4.2b) than in the laser-induced one (Figure 4.3b). Several studies [37, 24, 108] have used high-resolution characterization techniques to show the nanosized structure of field WEL in detail. In field conditions, the rail surface is severely deformed during wheel and rail contact causing grain refinement of the WEL via the austenite and consequently an increase in hardness. The results suggest that grain refinement is an effect of the plastic deformation of the rail surface and is not achieved by an exclusive ther-

mal process such as laser heating.

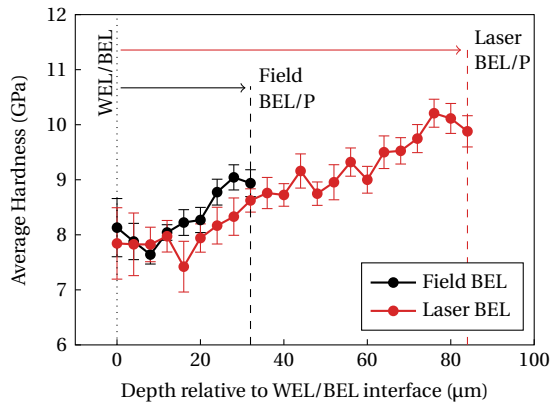


Figure 4.7: Average hardness of the field and laser BEL as a function of depth from the WEL/BEL interface.

## 4.5. CONCLUSIONS

This chapter considers the characterization of field and laboratory laser-induced WEL and BEL. From the results presented in previous sections, the following conclusions can be extracted:

- Laser treatment allows the reproduction of WEL and BEL layers with similar microstructural features and hardness as field WEL and BEL. The most distinguishable aspect is the dimensions of these features which are much larger in the layers formed via laser treatment. This might be related to the absence of plastic deformation in this sample, suggesting that field WEL and BEL are formed due to a thermomechanical process.
- The laser and field BEL consist of a complex microstructure varying along the depth of these layers suggesting different stages of microstructure development. However, more advanced characterization techniques are required in order to evaluate the microstructure in more detail.
- This study strongly supports the hypothesis that the WEL is martensite while the BEL is tempered martensite formed due to the subsequent reheating of previously formed WEL.
- Laser heat treatment shows that WEL and BEL can be formed without severe plastic deformation, demonstrating the importance of high temperatures in the formation of these layers.





# 5

## MICROSTRUCTURAL CHARACTERIZATION OF HYPEREUTECTOID PEARLITIC STEEL CONTAINING VANADIUM

5

*The purpose of this research is to understand the role of vanadium in the microstructure of hypereutectoid pearlitic steels and the effect on mechanical behavior. To accomplish this, scanning electron microscopy and transmission electron microscopy are used to evaluate the microstructure, focusing on phases forming at grain boundaries, interlamellar spacing, and vanadium carbide precipitation. The precipitation behavior of vanadium carbide and cementite at the austenite grain boundary is simulated using DICTRA. Additionally, tensile tests were carried out, and the results are compared to those of a standard vanadium-free R260 eutectoid rail steel grade. The main contribution of the vanadium in this steel is the prevention of the occurrence of grain boundary embrittlement.*

---

This chapter is based on:

- V. Mattos Ferreira, B. Schotsman, M.G. Mecozzi, R.H. Petrov, J. Sietsma, "Microstructural characterization of hypereutectoid pearlitic steel containing vanadium", submitted

## 5.1. INTRODUCTION

Hypereutectoid pearlitic steels with carbon contents between 0.8 and 1.0 wt% are commonly used for heavy haul applications due to their high wear resistance and strength. This very good performance is mainly related to the higher hardness when compared to eutectoid steels. However, the constant demand for increased loading of freight trains imposes a challenge due to the extreme conditions to which heavy haul rails are subjected. As a result, the railway industry has been looking for alternatives in order to reduce the maintenance and increase the service life of heavy haul rails by investing in high-performance railway steel grades with even higher strength and wear resistance.

Microstructural features of pearlitic steels such as interlamellar spacing, intermetallic inclusions, and the presence of ferrite or cementite at the prior-austenite grain boundaries have a great influence on the performance of the rails. The interlamellar spacing has a direct relation with the strength and hardness of pearlitic steels, following a Hall-Petch relationship [109, 110]. This effect has been associated with dislocation pile-ups and the mean free path for dislocations, which is higher for larger interlamellar spacings [15]. Intermetallic inclusions formed during the processing of rail steels are generally considered preferential sites for crack initiation and propagation [111, 112]. These inclusions not only differ in their thermal expansion coefficient compared to the matrix, but they also exhibit an incoherent boundary with the pearlitic matrix. Thus, dislocation movement is restrained during deformation, leading to stress-concentration regions that will ultimately break, generating cracks. Some studies have also observed cracks associated with pro-eutectoid ferrite in pearlitic rail steel [74, 113]. It has been suggested that a high degree of strain accumulates in these regions as a result of severe deformation during train passage [74]. Additionally, pro-eutectoid cementite can induce cleavage cracking or delamination cracking due to its brittle nature, accelerating fatigue crack propagation [114]. Hence, pro-eutectoid ferrite and cementite are considered fragile sites in pearlitic railway steels and their fractions should be minimized in order to optimize the rail service life.

One way of controlling the microstructural aspects of steel grades is by alloying. Silicon and manganese are known to be solid-solution strengtheners of ferrite [21]. In addition, silicon can prevent the formation of pro-eutectoid cementite at the prior-austenite grain boundaries [115, 116, 117]. Manganese, on the other hand, acts on limiting the prior-austenite grain size and interlamellar spacing of the pearlite, leading to an increase in strength and toughness [11, 109].

Vanadium is a strong carbide former with the potential to influence the pearlitic cementite as well as to promote additional carbide precipitation in the pearlitic microstructure. Depending on their density, size, morphology, and distribution, these precipitates can have a significant impact on the mechanical properties of vanadium-alloyed steels. In these steels a phenomenon known as "interphase precipitation" of VC is frequently observed [118, 119]. This precipitation takes place at the interface between austenite and ferrite during austenite decomposition. Interphase precipitation was observed both in the pearlitic ferrite lamellae and in pro-eutectoid ferrite during the isothermal formation of pearlitic steels [120]. These precipitates are usually equally distributed in the form of fine aligned sheets parallel to each other and are assumed to have a role in the strength of these alloys [121]. Moreover, previous studies pointed out that carbide-forming elements, such as vanadium, partition to the cementite [122, 123, 124]. In a study on pearlitic wire steels containing vanadium, the V-enriched cementite showed more fragmentation, suggesting an increase

in the strength of the cementite and thus a reduction in ductility [125]. Vanadium addition also lowers the carbon content of the eutectoid point. This allows steels with an otherwise nominal eutectoid composition to actually become hypereutectoid steels, leading to the formation of pro-eutectoid cementite [126].

At the same time, vanadium addition prevents the formation of a continuous pro-eutectoid cementite layer at the prior-austenite grain (PAG) boundaries in steels with carbon content above 0.8 wt.% [121, 127]. Instead, coarse cementite particles are seen along these boundaries. This behavior was attributed to the presence of a low density of vanadium carbides at the prior-austenite boundaries, leading to a local depletion of carbon in its surroundings. This not only reduces the carbon diffusion towards cementite particles, inhibiting their growth, but also promotes ferrite growth that constrains even further the continuous boundary-cementite network. Previous studies [128, 129, 130] have also shown the effect of vanadium addition on the refinement of the austenite grains caused by the presence of vanadium carbides (VC) in the pearlitic ferrite, causing the pinning of the grain boundaries. However, Solano Alvarez et al. [124] compared rail steel grades with and without vanadium and found no significant differences in austenite grain size.

The objective of this paper is to understand the effects of the addition of 0.1 wt.% of vanadium on the microstructural features and properties of a naturally hard (air-cooled) unused hypereutectoid railway steel with Mn and high Si contents. In order to do so, the interlamellar spacing is evaluated and compared with commonly used railway steel grades. Besides, Transmission Electron Microscopy (TEM) is used to investigate the location and morphology of vanadium carbides in the microstructure. Simulations with diffusion-controlled transformation kinetics (DICTRA) are made to study the precipitation behavior of VC and cementite at the austenite grain boundary during cooling of HP335 steel. Tensile tests are performed to evaluate mechanical properties and fracture behavior to provide an indication of the response of the microstructure of this vanadium-containing steel.

## 5.2. MATERIAL AND METHODS

### 5.2.1. MATERIAL

A pearlitic railway steel grade with hypereutectoid carbon content and the addition of vanadium was selected for studying its microstructure and properties. The main alloying elements in this HP335 rail steel are carbon, manganese, and silicon with 0.1 wt.% of vanadium, as presented in Table 5.1. The HP335 rail is hot rolled in 17 stages after heating to approximately 1240°C. In the last stage, a cross-section area reduction of 13.9% is realized to reach the final rail geometry at a temperature of 1000°C before air cooling. This air cooling is specifically different from most other premium rail steels which are usually subjected to fast cooling to obtain a small interlamellar spacing and improved properties due to the increased cooling rate. X-ray diffraction shows the presence of 91% BCC structure (ferrite) and 9% cementite.

Table 5.1: Chemical composition of HP335 steel.

Steel	Element concentration (wt.%)			
	C	Mn	Si	V
HP335	0.91	0.88	0.87	0.10

### 5.2.2. METHODS

The received rail was fresh from the rolling mill and had not been subjected to any loading on railway tracks. In this work, the microstructural characterization of the as-received material will be performed on samples acquired from the rail head's central location. The sectioning of the rail head is depicted schematically in Figure 5.1.

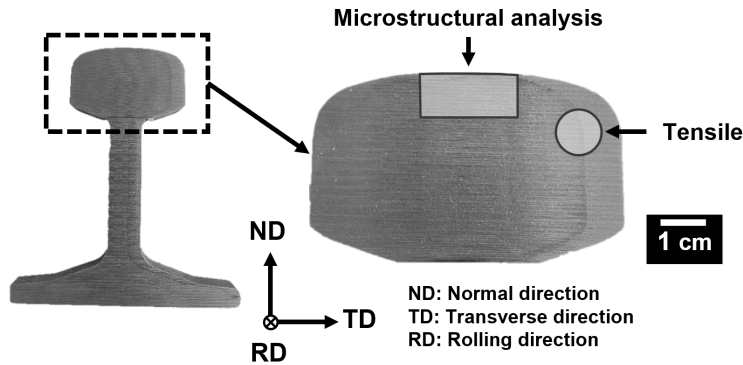


Figure 5.1: Sectioning description of the railway rail head evidencing the location of the samples used for microstructural analysis (middle of rail's head) and tensile samples (gauge corner of rail's head).

After sectioning, the samples used for microstructural characterization were mounted in conductive resin, ground with a series of SiC papers, and polished up to 1  $\mu\text{m}$  diamond paste using standard metallographic techniques. X-Ray Diffraction (XRD) was carried out in a Bruker D8 Discover diffractometer with an Eiger-2 500k 2D detector to obtain the phase fractions. The  $2\theta$  scan was performed using Cu K- $\alpha$  radiation in the angular range from  $30^\circ$  to  $150^\circ 2\theta$  and a step size of  $0.040^\circ 2\theta$ . Vickers microhardness measurements were performed using a Durascan 70 (Struers) hardness tester by applying a load of 10 N for 10 s. Both tests were done on the as-polished sample surface. The procedure was followed by chemical etching with Nital 2% for 10 s to reveal the microstructure.

High magnification micrographs of the microstructure were obtained with a Helios G4 PFIB UXe SEM using a 10 kV accelerating voltage, 0.1 nA current, and secondary electron imaging detection mode. The apparent interlamellar spacing was measured considering the linear intercept method. For that, SEM micrographs with 18,000x magnification were obtained from pearlite colonies with straight lamellae. Then, a total of ten lines perpendicular to the lamellae orientation were placed and the intercepts were counted and used to calculate the apparent interlamellar spacing.

In addition to specimens for microstructural characterization, tensile test specimens were made to investigate the tensile and fracture behavior of the rail steel. The test specimens were designed according to ISO6892-1:2019 for tensile testing at room temperature [131], with a 10 mm diameter and a parallel length of 50 mm. The specimens were obtained parallel to the rolling direction in the rail head close to the gauge corner, as depicted in Figure 5.1. The cross-sectional microstructural analysis of the rail showed that a similar microstructure is observed in both analyzed regions (middle and side of the rail head).

Scanning Transmission Electron Microscopy (STEM) foils were prepared using the twin-jet electropolishing technique. The foils were characterized using a Jeol JEM-2200FS FEG-

TEM with a voltage of 200 kV. The distribution of constituent elements is obtained via Energy Dispersive X-ray Spectroscopy (EDS). A minimum objective aperture size of 100 nm was used for performing Selected-Area Electron Diffraction (SAED) in order to characterize the fine precipitates.

Prior to testing, the specimens were kept for 6 hours at 200 °C to reduce the stress resulting from machining for production, as prescribed by EN13674-1 [132]. The diameter at the parallel length prior to testing was measured at three locations and averaged.

Tensile tests were performed at room temperature using an Instron 5985 static testing system with a self-aligning grip arrangement and a 250 kN load cell. The elongation was measured with an Instron AVE 2 non-contacting video extensometer. A constant crosshead separation speed of 0.75 mm/min is chosen, which corresponds to a strain rate  $\dot{\epsilon}_L = 2.5 \times 10^{-4} \text{ s}^{-1}$ , suitable for the determination of yield strength and elongation at fracture [131]. No differentiation is made for the elastic and plastic stages.

After the tensile tests, two metallographic samples were prepared. The first sample was used for observation of the fracture surface while the second was cut for the analysis of the cross-section. For fractography, images of the fracture surface were made with a JEOL IT100 Scanning Electron Microscope (SEM) in secondary electron detection mode at an acceleration voltage of 20 kV, and a working distance of 11 mm.

## 5.3. RESULTS

### 5.3.1. INTERLAMELLAR SPACING AND HARDNESS

Figure 5.2 shows a high magnification SEM micrograph of HP335 steel evidencing the lamellar pearlitic microstructure. The average apparent interlamellar spacing obtained for HP335 rail steel is  $280 \pm 40 \text{ nm}$ . This value is in the same order of magnitude as measured for standard air-cooled eutectoid rail steels such as R260:  $310 \pm 20 \text{ nm}$  [133] and  $282 \pm 11 \text{ nm}$  [134]. However, the average hardness of the HP335 steel is  $351 \pm 12 \text{ HV}$  which is higher than observed for standard grades (typically 280 HV [134]).

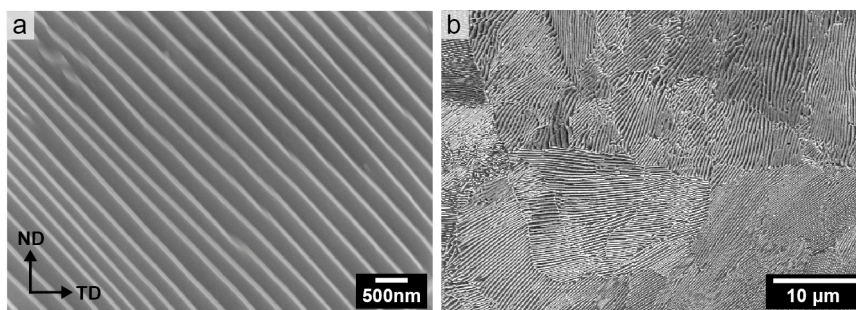


Figure 5.2: SEM micrograph depicting (a) the pearlitic lamellae and (b) the pearlite colonies of HP335 steel.

### 5.3.2. GRAIN BOUNDARY PHASES

#### SCANNING ELECTRON MICROSCOPY

The pearlite microstructure and the prior-austenite grain boundaries were analyzed at different depths from the rail surface to understand the microstructural characteristics of the

bulk material. Figure 5.3 depicts the micrographs corresponding to six different distances from the surface. The minimum depth from the rail surface shown is 0.3 mm to avoid the decarburized layer at the rail surface that is found in all rail grades as a natural consequence of the manufacturing process. The microstructural features are very similar at the various depths from the rail surface as can be seen in Figure 5.3. Thin ferrite layers seem to be present at some colony boundaries, coinciding with the prior-austenite grain boundaries. The layers are not continuous or distributed homogeneously. The observation is quite unexpected as the HP335 steel composition is in the hypereutectoid region of the phase diagram. Therefore, cementite is expected to be present at the boundaries rather than ferrite. This boundary ferrite has been previously reported in the literature [127, 135], mainly for isothermally heat-treated hypereutectoid pearlitic steels with vanadium additions.

Some studies [127, 136, 137, 138] suggested that the boundary ferrite is formed exclusively due to VC precipitation at the austenite grain boundaries. This causes carbon depletion in the vicinity of these carbides, promoting ferrite formation. Nonetheless, Han et al. [139] reported that most of the VC precipitates were present within the boundary ferrite, with only a minor portion found at the austenite boundaries. Therefore, the VC precipitation at the austenite boundary alone would not be enough to promote the formation of a ferrite layer.

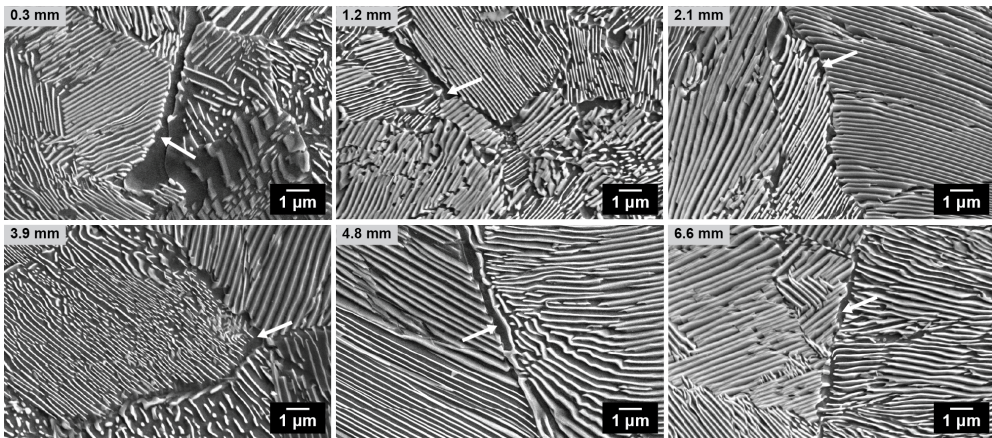


Figure 5.3: SEM micrographs depicting the boundary ferrite layers (white arrows) found at different depths from the surface of HP335 steel.

Other studies [127, 135, 140] propose that vanadium inhibits the growth of a continuous cementite network at the austenite boundaries due to the precipitation of VC. In this case, both cementite particles and VC would be present in the austenite boundary, leading to a depletion in carbon which promotes the formation of ferrite in these regions. This is in line with the microstructural analysis in Figure 5.3 where some coarse cementite particles within or close to the boundary ferrite are observed, which suggests that their formation occurs prior to pearlite growth. No VC precipitates are observed in SEM analysis because of the small particle size of these precipitates, which requires higher resolution techniques as will be presented in the following paragraphs.

## TRANSMISSION ELECTRON MICROSCOPY (TEM)

In previous sections, no presence of VC was detected via XRD and SEM. For this reason, the TEM technique was used in order to locate the possible VC in the microstructure. Figure 5.4 shows the Energy Dispersive Spectroscopy (EDS) mapping of two different regions of the sample: cementite lamellae (Figure 5.4a) and a low-angle grain boundary (Figure 5.4b).

As expected, the region with pearlitic cementite lamella shows a strong Mn enrichment, see Figure 5.4a. According to [141], the cementite lamellae of V micro-alloyed steels are also enriched in V. The dashed lines in Figure 5.4a indicating the cementite lamella are drawn on the basis of the Mn enrichment. The BCC dark-field image shows some overlapping of BCC and cementite ( $\theta$ ) through the sample thickness. However, only a limited V enrichment is observed in the EDS mapping of the pearlitic cementite region in HP335 steel.

At the grain boundary regions, some vanadium-enriched precipitates with approximately 10 nm diameter are detected as highlighted by the white arrows in Figure 5.4b. Figure 5.4c shows the STEM bright-field image of a boundary region. As can be seen, a thin ferrite layer is present at the boundary together with some cementite particles, which are likely to have precipitated prior to pearlite formation. The presence of these precipitates suggests that both cementite and VC lead to a depletion in carbon at the grain boundaries, promoting the formation of boundary ferrite in this hypereutectoid steel.

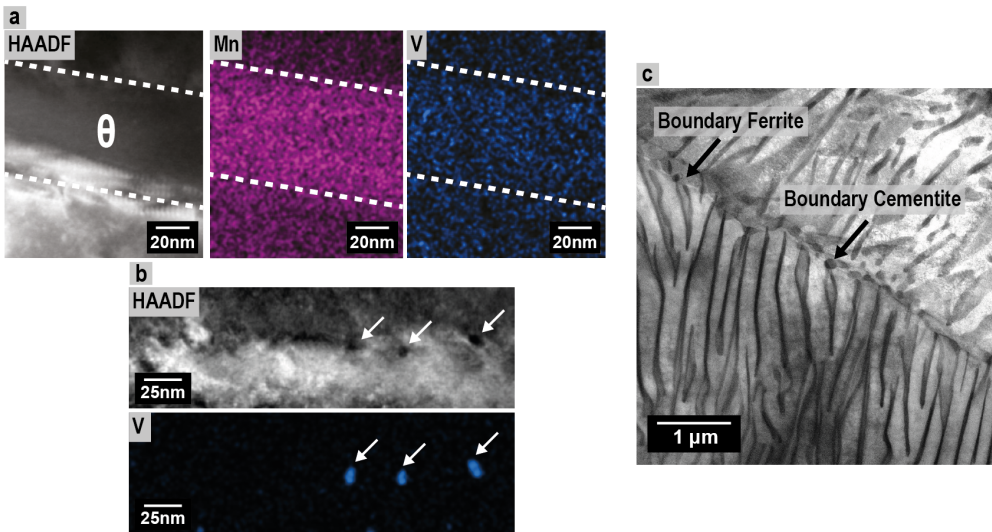


Figure 5.4: High-angle annular dark-field imaging (HAADF) and EDS mapping from the (a) cementite lamella region and (b) boundary region with the presence of VC (white arrows). (c) STEM bright-field image evidencing boundary ferrite and cementite (black arrows) of HP335 steel.

In Figure 5.5, the bright-field image of a pearlitic ferrite region, the selected-area diffraction pattern (SAED), and a dark-field image of VC are depicted. In these regions, spherical precipitates of approximately 9 nm are located within the pearlitic ferrite, suggesting the presence of VC. The selected-area diffraction pattern in Figure 5.5b confirms the Baker-Nutting orientation relationship with  $(001)_{\alpha} // (001)_{VC}$ ,  $[110]_{\alpha} // [100]_{VC}$  between the precipitates and the pearlitic ferrite, which is characteristic of vanadium carbide precipitation in a BCC phase [142]. These precipitates show a random distribution within the pearlitic ferrite

instead of being aligned as commonly observed for interphase precipitation at the moving  $\alpha/\gamma$  interface during pearlite formation [122, 143]. This different precipitation configuration might be due to the lack of time for interphase precipitation to occur due to continuous cooling, resulting in a random distribution due to precipitation within the pearlite.

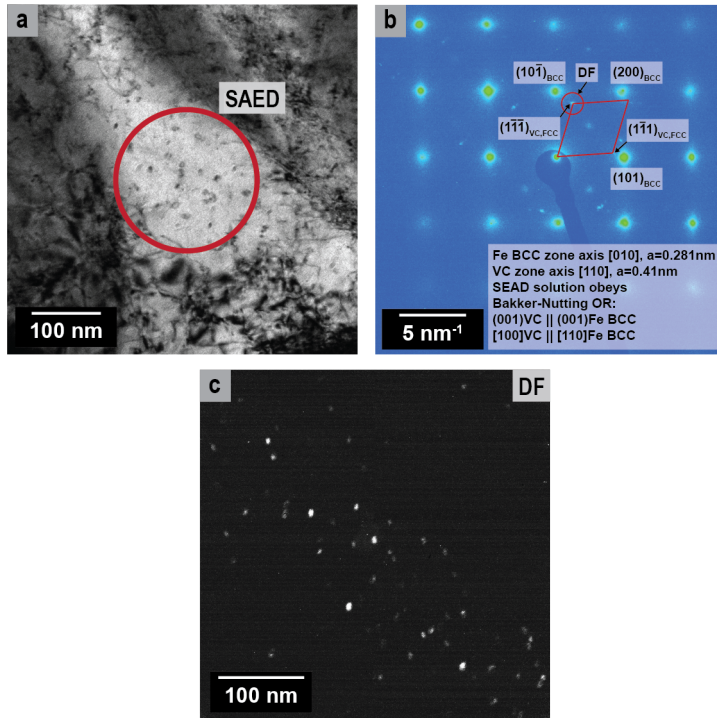


Figure 5.5: (a) Bright-field TEM image highlighting pearlitic ferrite region considered for the selected-area electron diffraction (SAED); (b) SAED evidencing the Baker-Nutting orientation relationship between VC precipitates and the ferrite matrix; (c) Dark-field image with a reduced aperture showing the diffraction point highlighted in (b).

### 5.3.3. THERMODYNAMICS AND KINETICS ANALYSIS

Vanadium is added to the composition of the hypereutectoid HP335 rail steel, which results in a complex phase diagram introducing the precipitation of VC in specific temperature ranges. The Fe-C isopleth for the overall values of Mn, Si, and V concentrations, calculated by the ThermoCalc software using the TCFE13 database, is shown in Figure 5.6 with the overall carbon concentration indicated by the dashed line. Although the phase diagram is only valid for equilibrium conditions, i.e. slower cooling than the air cooling of the HP335 after rolling, it will provide an impression of important temperature ranges and VC precipitation in the microstructure.

As previously mentioned, the steel temperature after the hot rolling is approximately 1000 °C. At this temperature, the vanadium is completely dissolved in the fully austenitic microstructure. During cooling, VC can start to precipitate in austenite ( $\gamma$ ) at approximately 950 °C. When the  $A_{e3}$  temperature is reached at 810 °C, cementite ( $\theta$ ) can precipitate at the



austenite grain boundaries, reducing the carbon content in austenite. When the carbon in austenite reaches the eutectoid composition (0.74 wt.%), the remaining austenite can transform into pearlite. The equilibrium eutectoid temperature of this steel is 738 °C. From the thermodynamics results, the final microstructure of the HP335 steel after equilibrium cooling is expected to be pearlite with pro-eutectoid cementite and VC, most probably at the prior-austenite grain boundaries. However, as observed in the previous sections, the microstructure actually consists of pearlite with ferrite, VC, and fragmented cementite at the boundaries, see Figure 5.4b-c.

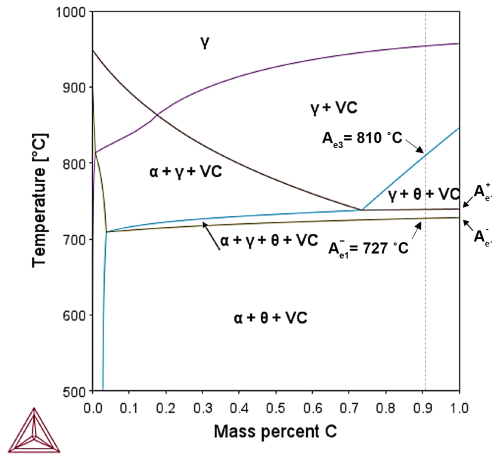


Figure 5.6: Fe-C phase diagram for HP335 steels obtained using Thermo-Calc software. The dashed lines represent the carbon concentration in the alloy studied.

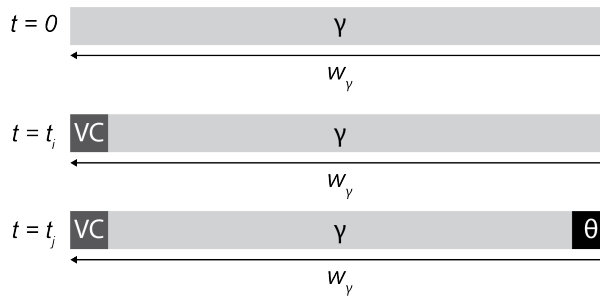


Figure 5.7: DICTRA simulation scheme displaying at  $t = 0$  the initial austenite ( $\gamma$ ) domain with width  $w_\gamma$ , representing an austenite grain boundary, followed by VC growth at  $t_i$  on the left extremity of the domain and cementite growth at a later stage ( $t_j$ ) on the right extremity of the domain.

The diffusion-controlled transformation software DICTRA [87] was used to simulate the growth behavior of cementite and VC at an austenite grain boundary of HP335 steel in order to explain the microstructural features found at these locations. Figure 5.7 presents a scheme of the 1D simulations performed with closed boundary conditions. As can be seen, the initial domain at the start, time  $t = 0$ , considered for all simulations consists only of

austenite. The domain widths ( $w_t$ ) chosen were 500 nm and 1  $\mu\text{m}$ , which are in the same order of magnitude as the distance between boundary cementite particles along the grain boundary found in Figure 5.4c. The different domain widths are chosen to understand the effect of the distance between VC and cementite on carbon and vanadium distribution in austenite as well as on the precipitate growth rate. The initial domain is then cooled from 1030  $^{\circ}\text{C}$  to 680  $^{\circ}\text{C}$  with a constant cooling rate of 1  $^{\circ}\text{C}\text{s}^{-1}$ . During cooling, at time  $t_i$  VC starts growing at the left extremity of the domain followed by cementite growth on the right extremity at a later stage ( $t_j$ ), see Figure 5.7. VC and cementite phases are both set dormant at the beginning of the simulation and they appear once a predefined default critical driving force in DICTRA ( $10^{-5}$  J/mole) for precipitation is attained.

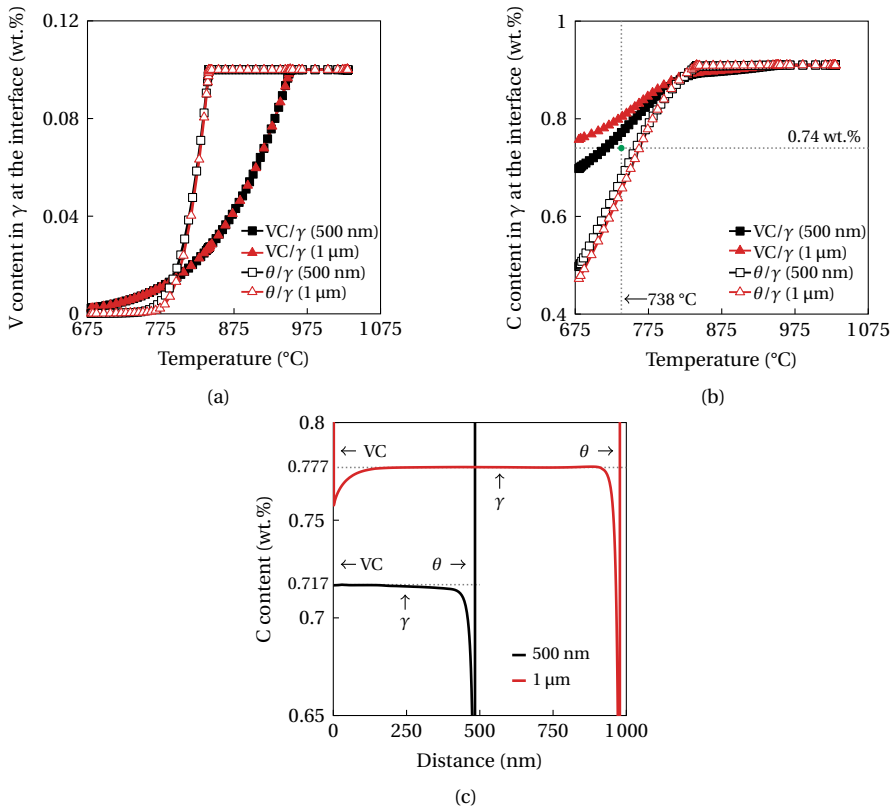


Figure 5.8: Vanadium (a) and carbon (b) contents in  $\gamma$  at the VC/ $\gamma$  and  $\gamma/\theta$  interfaces for simulations with  $w_t$  equal to 500 nm and 1  $\mu\text{m}$ . (c) Carbon content as a function of the distance at the end of the simulation for  $w_t$  equal to 500 nm and 1  $\mu\text{m}$ . The VC,  $\theta$ , and  $\gamma$  regions are indicated with black arrows for each domain.

Figure 5.8a presents the vanadium content in austenite at the VC/ $\gamma$  and  $\gamma/\theta$  interfaces as a function of temperature for both domains. VC precipitation occurs earlier than cementite precipitation, at approximately 950  $^{\circ}\text{C}$ . The VC growth leads to a decrease of the V content in austenite at the VC/ $\gamma$  interface (left extremity in Figure 5.7). However, this V depletion is very localized in the vicinity of the VC as no changes are seen in the austenite at the right extremity of the domain. At approximately 840  $^{\circ}\text{C}$ , cementite starts forming at the

right extremity of the domain leading to local vanadium depletion in austenite at the  $\gamma/\theta$  interface. As seen, the vanadium content at both interfaces is not significantly dependent on the domain distance.

In summary, these results suggest that the vanadium profile in austenite is not affected by the distance between the VC and cementite precipitates, corroborating the idea that V depletion occurs only very locally in the vicinity of these precipitates. However, DICTRA considers bulk diffusion which is relatively slow when compared with grain boundary diffusion. The vanadium diffusivity in austenite is derived from the atomic mobility database (MOBFE8) of Thermo-Calc software and it was not possible to correct this value by taking into account the higher vanadium diffusivity at the austenite grain boundary. Thus, the diffusion lengths can be higher than calculated for the bulk, especially in the case of vanadium. Vanadium depletion therefore could be more significant in the alloy studied than can be concluded from the simulation results.

The carbon content in austenite at the VC/ $\gamma$  and  $\gamma/\theta$  interfaces as a function of temperature is shown in Figure 5.8b. A decrease of the carbon content in austenite at VC/ $\gamma$  and  $\gamma/\theta$  interfaces is seen when both VC and cementite precipitation occurs, where the decrease in carbon content is much more pronounced during cementite precipitation. Additionally, Figure 5.8b reveals that the distance between the precipitates impacts the carbon distribution in austenite, particularly at the VC/ $\gamma$  interface. This is evident at approximately 840 °C when cementite precipitates, leading to a significant decrease in the carbon content within the austenite at the VC/ $\gamma$  interface, reaching values below 0.8 wt.%. The effect of cementite precipitation on the carbon content at the VC/ $\gamma$  interface is more pronounced when the distance between cementite and VC is smaller.

Moreover, as previously mentioned, the austenite at the  $\gamma/\theta$  interface is strongly depleted in carbon. From Figure 5.8b, one can see that for temperatures below 773 °C, the local carbon content in austenite at the  $\gamma/\theta$  interface is below the eutectoid composition (0.74 wt.%) calculated for this steel, as is previously shown in Figure 5.6. This suggests that below this temperature the steel is locally behaving as hypo-eutectoid steel, allowing the possible formation of ferrite at the austenite grain boundaries before the temperature reaches the  $A_{e1}^+$  temperature of 738 °C or slightly lower. Although VC does cause carbon depletion in austenite, the carbon consumption by VC is not significant enough to cause concentrations to fall below the eutectoid point.

In Figure 5.8c, the overall carbon content at the end of the simulation is presented for  $w_t$  equal to 500 nm and 1  $\mu\text{m}$ . One can see that the carbon depletion caused by cementite precipitation is not restricted to the vicinity of the  $\gamma/\theta$  interface but occurs along the entire austenite region. For the simulation with  $w_t$  equal to 500 nm, the carbon content in the entire austenite region is below the eutectoid value (0.74 wt.%) suggesting that in this case, in the remaining austenite boundary, ferrite can form instead of cementite that would be expected for hypereutectoid steels. The temperature at which this can take place varies depending on the cooling rate, see Figure 5.9a. As illustrated, reducing the cooling rate results in a lowering of the temperature at which the carbon content in the austenite at the  $\gamma/\theta$  interface falls below the eutectoid point.

In Figure 5.9b the positions of the VC/ $\gamma$  and  $\gamma/\theta$  interfaces with respect to the left and right domain extremities are presented as a function of the temperature. The plotted curves show that VC growth is slightly affected by the distance between the precipitates. The overall movement of the VC/ $\gamma$  interface can be disregarded due to such a small interface position

change during growth. The cementite growth on the other hand is significantly affected by the inter-precipitate distance. As the distance between the precipitates is smaller, so is the rate of cementite growth. This observation suggests that VC could limit cementite growth at grain boundaries, leading to the formation of discrete cementite particles instead of the typical continuous boundary cementite layer seen in hypereutectoid steels.

To investigate the influence of VC on cementite growth, simulations were conducted exclusively allowing cementite formation within the austenite domain (Figure 5.9b). The resulting cementite growth is the same as the one obtained with the presence of VC for different  $w_\gamma$ . This confirms that cementite growth is impacted by the distance between cementite particles (the domain width is half this distance due to the closed boundary conditions considered in the simulation) and not by the presence of VC. However, VC might serve as a physical barrier to cementite growth in the actual material.

In summary, the simulations show that cementite precipitation is responsible for significant carbon depletion at the austenite grain boundaries of hypereutectoid steels to values below the eutectoid composition at temperatures above  $A_{e1}^+$ , leading to the possible formation of pro-eutectoid boundary ferrite. Increasing the cooling rate increases the temperature at which boundary ferrite precipitation can take place. In addition, the simulation results show that VC does not have a clear impact on cementite growth. The number density of VC and cementite precipitates in the real material can be higher, as previously seen in Figure 5.4b-c, promoting further carbon depletion and consequently the formation of the thin ferrite boundary layers as seen in Figure 5.3.

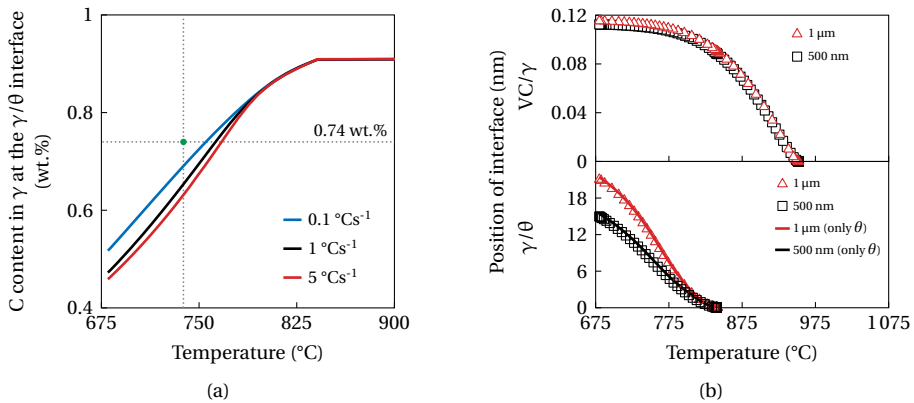


Figure 5.9: (a) Carbon content in  $\gamma$  at the  $\gamma/\theta$  interface with  $w_\gamma$  equal to  $1\text{ }\mu\text{m}$  for different cooling rates. (b) Position of VC/ $\gamma$  and  $\gamma/\theta$  interfaces as a function of temperature for simulations with  $w_\gamma$  equal to  $500\text{ nm}$  and  $1\text{ }\mu\text{m}$  together with the results for simulations considering only cementite formation. The green dot indicates the eutectoid point.

#### 5.3.4. TENSILE BEHAVIOR

Monotonic tensile tests have been executed for a study of the mechanical behavior of the HP335 rail steel. The strain hardening of the material, the fractography, and secondary crack initiation have been analyzed. In Figure 5.10 the engineering stress-strain curves are presented, together with the result for the standard grade R260-rail, as a reference [144].

From the extensometer signal the slope of the elastic linear extension stage is derived.

The slope is then used to calculate the 0.2% offset yield stress,  $R_{p0.2\%}$ . The average  $R_{p0.2\%}$  for the four HP335 tests is  $700 \pm 10$  MPa, which is 31% higher than for R260 railway steel. Before reaching the  $R_{p0.2\%}$  value, the curve shows a sharp transition from elastic to plastic extension, indicating a sudden change from elastic to plastic material response.

The tensile strength,  $\sigma_{UTS}$ , is  $1161 \pm 12$  MPa for the HP335 steel, which is 26% higher than for the R260 steel (Table 5.2). After reaching the ultimate tensile stress at an average plastic strain of 7.2%, an additional 1% strain occurs before the final fracture, during which the limited decrease in stress, a sign of limited localized strain concentration, is observed in the tensile curves of HP335 steel. This is consistent with the absence of visible necking in the tensile sample of the HP335 steel.

Table 5.2: Tensile test results

Steel	$R_{p0.2}$ (MPa)	Tensile strength (MPa)	Elongation (%)
HP335	$700 \pm 10$	$1161 \pm 12$	$8.2 \pm 0.2$
R260 [144]	533	924	12

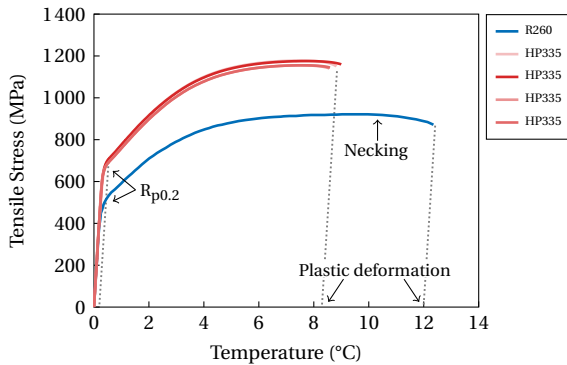


Figure 5.10: Engineering stress-strain curve obtained for HP335 and eutectoid R260 steel [144].

### Fracture surface

In Figure 5.11a, a SEM micrograph of the center portion of the fracture surface of the HP335 tensile specimen is presented. The surface is characterized by the cleavage facets with different orientations and by the presence of river patterns as highlighted. Characteristic are the secondary cracks, which are present throughout the fractured surface. Moreover, some regions contain sub-micron dimples suggesting a localized ductile fracture behavior indicated as ductile tearing [145]. These regions are most likely associated with the boundary  $\alpha$ -ferrite regions discussed in section 5.3.2, as this phase is more ductile than the alternating cementite and ferrite phases in the pearlite colonies.

The cross-section of the tensile fracture surface was investigated to study the shear morphology in the HP335 steel. A close examination of the pearlite colonies at the fractured surface in Figure 5.11b reveals a dominant lamellae orientation parallel to the stress direction. Furthermore, deformed lamellae are observed in pearlite colonies where lamellae are not initially oriented parallel to the applied stress. This suggests fracture by shearing after reorientation parallel to the applied stress.

Additionally, secondary cracks were also present within the pearlite colonies at a distance of 40  $\mu\text{m}$  to 100  $\mu\text{m}$  from the fractured surface. The rupture of the cementite-ferrite phase boundary is most frequently observed. This is locally accompanied by major deformation of the cementite lamellae, without fracturing them, which can be explained by the strain hardening of the ferrite at both sides of the cementite [146].

The propagation of the secondary cracks beyond the colony size requires the shearing of cementite, a process explained by the dislocation pile-up in the ferrite, which finally causes a local stress that ruptures the cementite [146, 147, 148]. The microcracks are therefore usually associated with a 45° angle between crack direction and lamellae orientation [145, 148]. In Figure 5.11b two secondary cracks are presented. Crack (1) seems to be arrested at the colony boundary as crack tip blunting is observed, whereas crack (2) shears through the cementite after realigning to  $\sim 45^\circ$ .

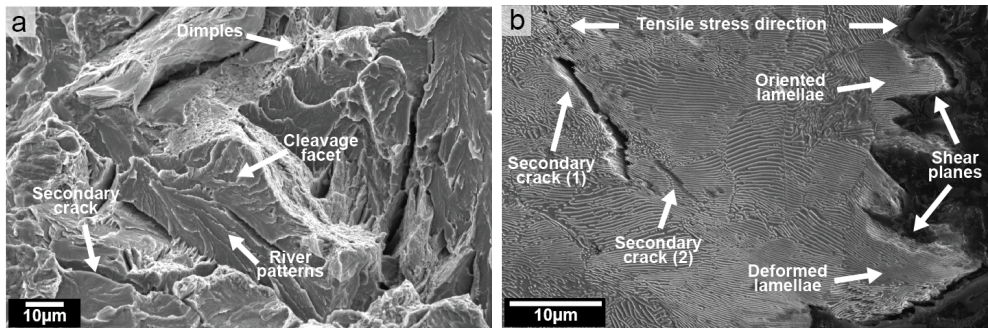


Figure 5.11: SEM micrograph of (a) the tensile fracture surface evidencing the brittle fracture features and (b) cross-section plane.

## 5.4. CONCLUSIONS

This paper investigates the microstructural features of a hypereutectoid railway pearlitic steel containing vanadium (HP335). A correlation between these microstructural features and the mechanical properties of this steel is presented. The results lead to the following conclusions:

- The microstructure of the hypereutectoid HP335 steel consists of pearlite with some fine boundary ferrite together with coarse boundary cementite particles. A slight vanadium enrichment is seen in the pearlitic cementite lamellae. Moreover, small and randomly distributed VC precipitates are found within the pearlitic ferrite. Some precipitates containing vanadium are also present at the grain boundaries.
- Thermodynamic calculations and DICTRA simulations indicate that the presence of boundary ferrite in hypereutectoid steels is due to the carbon depletion of austenite in the vicinity of the boundary cementite particles to levels below the eutectoid composition. The effect of VC on austenite carbon depletion by itself is not enough for ferrite formation. However, these carbides can play a role in the restriction of the cementite growth along the austenite boundaries.

- Despite the similar apparent interlamellar spacing of HP335 steel and R260, the former shows a higher hardness than the latter. The tensile tests show higher strength of HP335 when compared with conventional eutectoid rail steels. However, a lower ductility is also observed. The fracture surface is characterized by the cleavage facets seen in the fractured surface. Secondary cracks are present mostly within the pearlite colonies.





# 6

## CONCLUSIONS AND RECOMMENDATIONS

6

The research presented in this thesis investigated the origin of microstructural changes (White Etching Layer (WEL) and Brown Etching Layer (BEL)) that occur on the surface of railway tracks during wheel and rail contact as well as the microstructural characteristics of vanadium-alloyed hypereutectoid pearlitic railway steels which show improved performance in field conditions. A brief summary of the main findings from this thesis is presented below:

- The experimental investigation focusing on the microstructural changes of a pearlitic railway steel subjected to fast heating ( $200\text{ }^{\circ}\text{Cs}^{-1}$ ) followed by quenching shows that comparable hardness is obtained for WEL produced in the laboratory and the one from field conditions, which indicates the phase transformation as the dominant aspect in WEL formation. Similar microstructural features are observed in WEL from the field and after a single cycle of fast heating followed by quenching. However, the very small grain size observed in WEL produced during wheel/rail contact is not reproduced by thermal treatment only. This suggests that such a level of grain refinement is due to severe plastic deformation.
- Phase field modeling allows the simulation of the different microstructural processes and features of austenite formation from a pearlitic microstructure observed experimentally, such as lamellae thinning, morphology of the austenite front, preferential growth towards a specific pearlite colony and reduced kinetics during pro-eutectoid ferrite dissolution. The simulations show that different austenite morphologies are obtained according to the values of  $\gamma/\alpha$  and  $\gamma/\theta$  interface mobilities. Furthermore, carbon concentration gradients are observed in both austenite and ferrite for simulations with heating rates of 10 and  $200\text{ }^{\circ}\text{Cs}^{-1}$ . These gradients are much stronger for higher heating rates, which is due to the lack of time for carbon to homogenize in austenite. These carbon gradients can lead to inhomogeneities in the microstructure during intercritical heating and cooling such as rails are subjected to in the field.

- The laser-induced WEL and BEL layers presented in this thesis show similar microstructural features and hardness as field WEL and BEL. The most distinguishable aspect is the dimensions of these features, which are much larger in the layers formed via laser treatment. This is likely to be related to the absence of plastic deformation as only temperature rise is considered in the laser heat treatment. Additionally, laser and field BEL consist of a complex inhomogeneous microstructure varying along the depth of these layers, suggesting different stages of phase transformation. The different aspects of the investigated WEL and BEL strongly support the hypothesis that the WEL is martensite while the BEL is tempered martensite formed due to the reheating of previously formed WEL. The laser heat treatment also confirms that WEL and BEL can be formed without severe plastic deformation, demonstrating the importance of high temperatures in the formation of these layers.
- The microstructural characterization of a hypereutectoid railway pearlitic steel containing vanadium (HP335) shows a slight vanadium enrichment in the pearlitic cementite lamellae, small and randomly distributed VC precipitates within the pearlitic ferrite, and some precipitates containing vanadium at the grain boundaries. Moreover, thermodynamic calculations and DICTRA simulations indicate that the presence of boundary ferrite in hypereutectoid steels is due to the carbon depletion of austenite in the vicinity of the boundary cementite particles to levels below the eutectoid composition. The effect of VC on austenite carbon depletion by itself is not enough for ferrite formation. However, these carbides can play a role in the restriction of the cementite growth along the austenite boundaries.

## 6

## RECOMMENDATIONS

The central focus of this dissertation revolves around comprehending the microstructural features known as white and brown etching layers (WEL and BEL), specifically considering the sole influence of temperature rise, which occurs on rail surfaces due to the interaction between wheels and rails. Laboratory experiments have provided compelling evidence indicating that both these layers can indeed form purely as a result of temperature increase. Also, the evidence indicates that in field conditions, grain refinement is primarily due to rigorous plastic deformation. Furthermore, this dissertation presents a thorough characterization of a novel railway steel grade containing vanadium, exhibiting enhanced performance under field conditions. The analysis suggests that the presence of vanadium carbide precipitation within the pearlitic ferrite and at the grain boundaries can significantly contribute to the mechanical response of these steels and consequent improvements in the rail's field performance. However, to gain a more comprehensive understanding of the aforementioned points, further in-depth investigations are still necessary. Based on the information extracted from the study described in this thesis, the following recommendations are proposed in order to fill the remaining knowledge gaps:

- Investigating the impact of simultaneous loading and heating on the evolution of microstructures (WEL formation) in railway steels. This can be achieved through experiments involving dilatometry or Gleeble techniques. By conducting tests that consider rapid heating, compression, and subsequent quenching across various cycles, it is possible to obtain a comprehensive understanding of the distinct microstructural features via a thermomechanical process in a controlled laboratory setup. A comparison between the microstructural features achieved during the thermomechanical

cal process and the purely thermal process as presented in Chapter 2 of this thesis leads to more understanding of the effect of temperature and loading on WEL and BEL formation.

- In Chapter 3, phase field simulations involving the austenite formation from an initial pearlitic microstructure with resolved cementite lamellae were presented. It was shown that the formed austenite accounts for inhomogeneous C content, especially during the early stages of pearlite to austenite transformation. Therefore, it would be interesting to investigate the formation of martensite during fast cooling of austenite via phase field modeling. Differences in C content can lead to different  $M_s$  temperatures and heterogeneous microstructure. This effect could be enhanced if partial austenitization of the pearlite is considered prior to cooling.
- To gain deeper insight into field and laser-induced WEL and BEL, it is crucial to use advanced microstructural characterization techniques such as Transmission Electron Microscopy and Atom Probe Tomography to confirm the unique characteristics of these layers and their formation mechanism. Moreover, optimization of the laser setups to prevent the rail surface from melting during treatments is required. Additionally, the possible susceptibility for the formation of WEL and BEL in different rail steel grades (hypereutectoid, austenitic, bainitic, etc.) will lead to interesting findings.
- Understanding of the different improvements in microstructural features and mechanical properties of hypereutectoid steels containing vanadium, when subjected to different process routes (e.g. fast cooling), is to be developed. Such investigation aims to enhance overall performance by altering the microstructural attributes of pearlite, particularly the interlamellar spacing, and potentially allowing alternative precipitation mechanisms.



**A****MICRESS DRIVING FILE**

In this Appendix, an example of the driving file used for the MICRESS simulations discussed in Chapter 3 is presented.

## A.1. MICRESS DRIVING FILE EXAMPLE

```
#MICRESS binary
# =====
# version number: 7.003 (Windows)
# Language
# Please select a language: 'English', 'Deutsch' or 'Francais'
English
# Output Location
file
# Overwrite files with the same name?
overwrite
# Restart
# Restart using old results?
new
# Geometry
# Grid size?
# Cells in X-direction (CellsX):
600
# Cells in Y-direction (CellsY):
1
# Cells in Z-direction (CellsZ):
600
# Cell dimension (grid spacing in micrometers):
0,01
# Model
# Type of coupling?
concentration
# Thermal Conditions
no_lat_heat
# Boundary Conditions
# Boundary conditions for phase field in each direction
iiii
#
# Boundary conditions for concentration field in each direction
iiii
#
# Unit-cell model symmetric with respect to the x/y diagonal plane?
no_unit_cell_symm
# Database
# =====
# Is a thermodynamic database to be used?
database FeCMn_v2021b
# Which global relineralisation interval shall be used?
manual
# Relineralisation interval [s]
1.00000E-02
# Components
# Type of concentration?
atom_percent
#
# The database contains the following components:
# 1: C
# 2: FE
# 3: MN
# Component 0 (main component) ?
2
# FE identified
# Component 1 ?
1
# C identified
# Component 2 ?
3
# MN identified
# Component 3 ?
```

```

end_of_components
#
# MICRESS component indexing
# 0 -> FE (database)
# 1 -> C (database)
# 2 -> MN (database)
# Phases
# Name or database index of phase 0 (matrix phase)
liquid
# Name or database index of phase 1
3
# Name or database index of phase 2
1
# Name or database index of phase 3
2
# Name or database index of phase 4
end_of_phases
# MICRESS phase indexing
# 0 -> LIQUID
# 1 -> FCC_A1 (database)
# 2 -> BCC_A2 (database)
# 3 -> CEMENTITE (database)
#
# Input/Output Format for Orientations
# How shall grain orientations be defined?
angle_2d
# Phase Properties
# Phase 0 ( LIQUID )
# Type of molar volume input ?
constant
# Value of molar volume ? ((cm**3/mol))
10.0
#
# Phase 1 ( FCC_A1 )
# Simulation of recrystallisation in phase 1 (FCC_A1)?
no_recrySTALL
# Is phase 1 (FCC_A1) anisotropic ?
anisotropic
# Crystal symmetry of phase 1 (FCC_A1) ?
cubic
# Should grains of phase 1 (FCC_A1) be reduced to categories?
no_categorize
# Type of molar volume input ?
constant
# Value of molar volume ? ((cm**3/mol))
7.1824
#
# Phase 2 ( BCC_A2 )
# Simulation of recrystallisation in phase 2 (BCC_A2) ?
no_recrySTALL
# Is phase 2 (BCC_A2) anisotropic ?
anisotropic
# Crystal symmetry of phase 2 (BCC_A2) ?
cubic
# Should grains of phase 2 (BCC_A2) be reduced to categories?
no_categorize
# Type of molar volume input ?
constant
# Value of molar volume ? ((cm**3/mol))
7.2757
#
# Phase 3 ( CEMENTITE )
# Simulation of recrystallisation in phase 3 (CEMENTITE) ?
no_recrySTALL
# Is phase 3 (CEMENTITE) anisotropic ?
anisotropic
# Crystal symmetry of phase 3 (CEMENTITE) ?
orthorhombic
# Should grains of phase 3 (CEMENTITE) be reduced to categories?

```

```

no_categorize
# Type of molar volume input ?
constant
# Value of molar volume ? [(cm**3/mol)]
7.63
# Phase Interactions
# 0 (LIQUID) / 1 (FCC_A1)
# Simulation of interaction between 0 (LIQUID) and 1 (FCC_A1) ?
no_phase_interaction
#
# 0 (LIQUID) / 2 (BCC_A2)
# Simulation of interaction between 0 (LIQUID) and 2 (BCC_A2) ?
no_phase_interaction
#
# 0 (LIQUID) / 3 (CEMENTITE)
no_phase_interaction
#
# 1 (FCC_A1) / 1 (FCC_A1)
phase_interaction
# Type of interfacial energy definition between 1 (FCC_A1) and 1 (FCC_A1) ?
constant
# Interfacial energy between 1 (FCC_A1) and 1 (FCC_A1) ? [J/cm**2]
7.0000E-05
# Type of mobility definition between FCC_A1 and FCC_A1?
constant
# Kinetic coefficient mu between FCC_A1 and FCC_A1 [cm**4/(Js)] ?
5.000000E-8
# Shall misorientation be considered?
no_misorientation
#
# 1 (FCC_A1) / 2 (BCC_A2)
# Simulation of interaction between 1 (FCC_A1) and 2 (BCC_A2) ?
phase_interaction redistribution_control
# 'DeltaG' options: default
avg 0.5 max 100
# Type of interfacial energy definition between 1 (FCC_A1) and 2 (BCC_A2) ?
constant
# Interfacial energy between 1 (FCC_A1) and 2 (BCC_A2) ? [J/cm**2]
6.00E-05 1.000E-04
# Type of mobility definition between FCC_A1 and BCC_A2?
temp_dependent
# File for kinetic coefficient between FCC_A1 and BCC_A2? [cm**4/(Js)]
M01e-6Q140.txt
# Shall misorientation be considered?
misorientation low_angle_limit 0 special_orient 3
# Input of the special orientation relation Nb 1
# Rotation angle? [tolerance] (in degrees)
60 0.1
# Prefactor of interfacial energy for the special OR:
1.0000
# Prefactor of interfacial mobility for the special OR?
1.0000
# Input of the special orientation relation Nb 2
# Rotation angle? [tolerance] (in degrees)
30 0.1
# Prefactor of interfacial energy for the special OR:
1.0000
# Prefactor of interfacial mobility for the special OR?
1.0000
# Input of the special orientation relation Nb 3
# Rotation angle? [tolerance] (in degrees)
0. 360.
# Prefactor of interfacial energy for the special OR:
1.0000
# Prefactor of interfacial mobility for the special OR?
0.0000
# Is interaction isotropic?
isotropic
# Which phase diagram is to be used?

```



```

database global
# Relinearisation interval for interface FCC_A1 / BCC_A2
none
# Please specify the redistribution behaviour of each component:
# Component C:
normal mob_corr
# Component MN:
normal
#
# 1 (FCC_A1) / 3 (CEMENTITE)
# Simulation of interaction between 1 (FCC_A1) and 3 (CEMENTITE) ?
phase_interaction redistribution_control
# 'DeltaG' options: default
avg 1. max 100.
# Type of interfacial energy definition between 1 (FCC_A1) and 3 (CEMENTITE) ?
constant
# Interfacial energy between 1 (FCC_A1) and 3 (CEMENTITE) ? [J/cm**2]
4e-5 1e-4
# Type of mobility definition between FCC_A1 and CEMENTITE?
temp_dependent
# File for kinetic coefficient between FCC_A1 and CEMENTITE? [cm**4/(Js)]
M01e-6Q140.txt
# Shall misorientation be considered?
misorientation low_angle_limit 0 special_orient 3
# Input of the special orientation relation Nb 1
# Rotation angle? [tolerance] (in degrees)
47 0.1
# Prefactor of interfacial energy for the special OR:
1.0000
# Prefactor of interfacial mobility for the special OR?
1.0000
# Input of the special orientation relation Nb 2
# Rotation angle? [tolerance] (in degrees)
17 0.1
# Prefactor of interfacial energy for the special OR:
1.0000
# Prefactor of interfacial mobility for the special OR?
1.0000
# Input of the special orientation relation Nb 3
# Rotation angle? [tolerance] (in degrees)
0. 360.
# Prefactor of interfacial energy for the special OR:
0.0000
# Prefactor of interfacial mobility for the special OR?
0.0000
# Is interaction isotropic?
isotropic
# Which phase diagram is to be used?
database global
# Relinearisation interval for interface FCC_A1 / CEMENTITE
none
# Please specify the redistribution behaviour of each component:
# Component C:
normal mob_corr
# Component MN:
normal
#
# 2 (BCC_A2) / 2 (BCC_A2)
# Simulation of interaction between 2 (BCC_A2) and 2 (BCC_A2) ?
phase_interaction
# Type of interfacial energy definition between 2 (BCC_A2) and 2 (BCC_A2) ?
constant
# Interfacial energy between 2 (BCC_A2) and 2 (BCC_A2) ? [J/cm**2]
7.0000E-05
# Type of mobility definition between BCC_A2 and BCC_A2?
constant
# Kinetic coefficient mu between BCC_A2 and BCC_A2 [cm**4/(Js)] ?
0.500000E-7
# Shall misorientation be considered?

```

```

no_misorientation
#
# 2 (BCC_A2) / 3 (CEMENTITE)
# Simulation of interaction between 2 (BCC_A2) and 3 (CEMENTITE) ?
phase_interaction
# 'DeltaG' options: default
avg 1. max 100.
# Type of interfacial energy definition between 2 (BCC_A2) and 3 (CEMENTITE) ?
constant
# Interfacial energy between 2 (BCC_A2) and 3 (CEMENTITE) ? [J/cm**2]
5.00E-05 1.000E-04
# Type of mobility definition between BCC_A2 and CEMENTITE?
constant
# Kinetic coefficient mu between BCC_A2 and CEMENTITE [cm**4/(Js)] ?
0.500e-7
# Shall misorientation be considered?
no_misorientation
# Is interaction isotropic?
isotropic
# Which phase diagram is to be used?
database global
# Relinearisation interval for interface BCC_A2 / CEMENTITE
none
#
# 3 (CEMENTITE) / 3 (CEMENTITE)
# Simulation of interaction between 3 (CEMENTITE) and 3 (CEMENTITE) ?
no_phase_interaction
#
# Diffusion
# How shall diffusion of component C in phase LIQUID be solved?
diagonal n
# How shall diffusion of component C in phase FCC_A1 be solved?
diagonal g
# How shall diffusion of component C in phase BCC_A2 be solved?
diagonal g
# How shall diffusion of component C in phase CEMENTITE be solved?
diagonal n
# How shall diffusion of component MN in phase LIQUID be solved?
diagonal n
# How shall diffusion of component MN in phase FCC_A1 be solved?
diagonal g
# How shall diffusion of component MN in phase BCC_A2 be solved?
diagonal g
# How shall diffusion of component MN in phase CEMENTITE be solved?
diagonal n
#
# How shall the interval for updating diffusion coefficients data be set?
constant
# Interval for updating diffusion coefficients data? [s]
1.0000
#
# Initial Microstructure
# Type of grain positioning?
from_file
# Filename of initial grain/phase structure [VTK_identifier (default=korn)] ?
portion2_3.txt
# Treatment of data?
n
# CellsX for initial microstructure?
600
# CellsZ for initial microstructure?
600
# Number of grains at the beginning?
57
# Read grain properties from a file?
input
#
# Grain number 1
# _____

```

# Phase number? (integer)  
2  
# Rotation angle? [Degree]  
86.000  
#  
2  
66.000  
2  
78.000  
2  
13.000  
3  
10.000  
3  
10.000  
3  
65.000  
3  
65.000  
3  
65.000  
3  
65.000  
3  
65.000  
3  
65.000  
3  
65.000  
3  
65.000  
3  
65.000  
3  
65.000  
3  
65.000  
3  
65.000  
3  
65.000  
3  
65.000  
3  
65.000  
3  
65.000  
3  
65.000  
3  
65.000  
3  
65.000  
3  
73.000  
3  
73.000  
3  
73.000  
3  
73.000  
3  
73.000  
3  
73.000  
3  
73.000  
3  
73.000  
3  
73.000

A

```
3
73.000
3
73.000
3
73.000
3
73.000
3
73.000
3
73.000
3
73.000
3
73.000
3
73.000
3
73.000
3
73.000
3
53.000
3
53.000
3
53.000
3
53.000
3
53.000
3
53.000
3
53.000
3
53.000
3
53.000
3
53.000
3
53.000
#
# Structure from restart file
# Shall grain(s) be replaced by initial structure(s) from a restart file(s) ?
no_restart_file
#
# Initial Concentrations
# How shall initial concentrations be set?
equilibrium 2
# Initial concentration of component 1 (C) in phase 2 (BCC_A2) ? [at%]
5.50000E-02
# Initial concentration of component 2 (MN) in phase 2 (BCC_A2) ? [at%]
0.71000
# Temperature at which the initial equilibrium will be calculated? [K]
973.00
#
# Process Conditions
# =====
# Temperature
# Type of temperature trend?
linear
# Number of connecting points? (integer)
```

```

0
# Initial temperature at the bottom? (real) [K]
1008.0
# Temperature gradient in z-direction? [K/cm]
0.0000
# Cooling rate? [K/s]
10.000
#
# 1D far field for solute diffusion
# -----
# Enable one dimensional far field approximation for solute diffusion?
no_1d_far_field
#
# Moving frame
# Moving-frame system in z-direction?
no_moving_frame
#
# Nucleation
# Enable further nucleation?
nucleation verbose
# Additional output for nucleation?
out_nucleation
#
# Number of types of seeds?
2
# Input for seed type 1:
# Type of 'position' of the seeds?
interface
# Phase of new grains (integer) [unresolved|add_to_grain|split_from_grain]?
1
# Reference phase (integer) [min. and max. fraction (real)]?
2
# Substrate phase [2nd phase in interface]?
2 2
# Maximum number of new nuclei of seed type 1?
3
# Grain radius [micrometers]?
0.0
# Choice of growth mode:
analytical_curvature
# Critical radius? [micrometers]
0.10000
# min. undercooling [K] (>0)?
0.0000
# Determination of nuclei orientations?
parent_relation
# Minimal value of rotation angle? [Degree]
60.000
# Maximal value of rotation angle? [Degree]
60.000
# Shield effect:
# Shield time [s] [shield phase or group number] ?
1.0
# Shield distance [micrometers] [ nucleation distance [micrometers] ]?
2.0
# Nucleation range
# min. nucleation temperature for seed type 1 [K]
873.00
# max. nucleation temperature for seed type 1 [K]
1273.0
# Time between checks for nucleation? [s]
constant
# Time interval [s]
2.00000E-02
# Shall random noise be applied?
nucleation_noise
# Factor for random noise?
5.00000E-02
#

```

```

# Input for seed type 2:
# Type of 'position' of the seeds?
interface
# Phase of new grains (integer) [unresolved|add_to_grain|split_from_grain]?
1
# Reference phase (integer) [min. and max. fraction (real)]?
2
# Substrate phase [2nd phase in interface]?
2 3
# Maximum number of new nuclei of seed type 2?
6
# Grain radius [micrometers]?
0.0
# Choice of growth mode:
analytical_curvature
# Critical radius? [micrometers]
0.10000
# min. undercooling [K] (>0)?
0.0000
# Determination of nuclei orientations?
parent_relation
# Minimal value of rotation angle? [Degree]
30.000
# Maximal value of rotation angle? [Degree]
30.000
# Shield effect:
# Shield time [s] [shield phase or group number] ?
1.0
# Shield distance [micrometers] [ nucleation distance [micrometers] ]?
2.5
# Nucleation range
# min. nucleation temperature for seed type 2 [K]
1018.0
# max. nucleation temperature for seed type 2 [K]
1273.0
# Time between checks for nucleation? [s]
constant
# Time interval [s]
2.00000E-02
# Shall random noise be applied?
nucleation_noise
# Factor for random noise?
1.00000E-02
#
# Seed for random-number generator initialisation
77777777
# Max. number of simultaneous nucleations?
0
# Shall metastable small seeds be killed?
no_kill_metastable
# Output times
linear_step .02 1
linear_step .05 5
linear_step .5 10
end_of_simulation
#
# Output files
out_restart
out_grains
out_phases
out_fraction 1 2
tab_fractions
out_interface
out_driv_force
out_relin
out_mobility
out_curvature
out_velocity
tab_grains

```

```
no_tab_vnm
tab_grain_data
out_temp
out_conc
out_conc_phase 3
tab_conc
no_out_recrySTALL
no_tab_recrySTALL
no_out_disloc
no_out_miller
out_orientation
no_tab_orientation
tab_lin
tab_log 0.25
#
# Numerical parameters
# Phase field solver
# Time-step ?
automatic_limited
constant
2.E-7 1.E-2
#Number of steps to adjust profiles of initially sharp interfaces [exclude_inactive]?
25
# Type of potential?
multi_obstacle fd_correction
# Phase minimum?
1.00E-06
# Interface thickness (in cells)?
3.0000
# Coefficient for initial dimension of field iFace
0.1
# Coefficient for initial dimension of field nTupel
0.1
#
# Concentration solver
# -----
# Factor for diffusion time stepping? (0.0 < factor < 1.0)
0.95000
#
stoich_enhanced_off
3 1
no_stoichio
```





# BIBLIOGRAPHY

- [1] H.K.D.H. Bhadeshia. "Novel Steels for Rails". In: *Encyclopedia of Materials Science: Science and Technology*. Pergamon, 2002, pp. 1–7. DOI: 10.1016/b0-08-043152-6/01836-2.
- [2] A. Kumar et al. "Design of high-strength and damage-resistant carbide-free fine bainitic steels for railway crossing applications". In: *Materials Science Engineering A* 759. April (2019), pp. 210–223. DOI: 10.1016/j.msea.2019.05.043.
- [3] K. Sawley and J. Kristan. "Development of bainitic rail steels with potential resistance to rolling". In: *Fatigue Fracture of Engineering Materials Structures* 26 (2003), pp. 1019–1029. DOI: <https://doi.org/10.1046/j.1460-2695.2003.00671.x>.
- [4] K. M. Lee and A. A. Polycarpou. "Wear of conventional pearlitic and improved bainitic rail steels". In: *Wear* 259.1-6 (2005), pp. 391–399. DOI: 10.1016/j.wear.2005.02.058.
- [5] Q. Luo et al. "Experimental investigation on the spalling failure of a railway turnout made from Hadfield steel". In: *Wear* 523. March (2023), p. 204779. DOI: <https://doi.org/10.1016/j.wear.2023.204779>.
- [6] O. A. Zambrano, G. Tressia, and R. M. Souza. "Failure analysis of a crossing rail made of Hadfield steel after severe plastic deformation induced by wheel-rail interaction". In: *Engineering Failure Analysis* 115 (2020), p. 104621. DOI: 10.1016/j.engfailanal.2020.104621.
- [7] B. Lv et al. "Micro-mechanism of rolling contact fatigue in Hadfield steel crossing". In: *International Journal of Fatigue* 44 (2012), pp. 273–278. DOI: 10.1016/j.ijfatigue.2012.04.010.
- [8] J. W. Ringsberg et al. "Rolling contact fatigue of rails-finite element modelling of residual stresses, strains and crack initiation". In: *Proceedings of the Institution of Mechanical Engineers, Part F: Journal of Rail and Rapid Transit* 214.1 (2000), pp. 7–19. DOI: <https://doi.org/10.1243/0954409001531207>.
- [9] J. E. Garnham and C. L. Davis. "Rail materials". In: *Wheel-rail interface handbook*. Ed. by R Lewis and U Olofsson. Woodhead Publishing Limited, 2009, pp. 125–171. DOI: 10.1533/9781845696788.1.125.
- [10] M. Ghodrati, M. Ahmadian, and R. Mirzaeifar. "Modeling of rolling contact fatigue in rails at the microstructural level". In: *Wear* 406-407 (2018), pp. 205–217. DOI: <https://doi.org/10.1016/j.wear.2018.04.016>.
- [11] S. S. Sahay, G. Mohapatra, and G. E. Totten. "Overview of Pearlitic Rail Steel: Accelerated Cooling, Quenching, Microstructure, and Mechanical Properties". In: *Journal of ASTM International* 6.7 (2010), pp. 1–26. DOI: 10.1520/JAI102021.
- [12] J. W. Ringsberg. "Shear mode growth of short surface-breaking RCF cracks". In: *Wear* 258.7-8 (2005), pp. 955–963. DOI: 10.1016/j.wear.2004.03.043.

- [13] J. Wu. "Microstructure evolution in pearlitic rail steel due to rail/wheel interaction". PhD thesis. Delft University of Technology, 2018. DOI: 10.4233/uuid:c536ca47-8981-4a9e-916f-396bcbca4bc5.
- [14] L. Wang et al. "Microstructure features on rolling surfaces of railway rails subjected to heavy loading". In: *Materials Science and Engineering A* 359 (2003), pp. 31–43. DOI: 10.1016/S0921-5093(03)00327-7.
- [15] O. P. Modi et al. "Effect of interlamellar spacing on the mechanical properties of 0.65 C steel". In: *Materials Characterization* 46 (2001), pp. 347–352. DOI: [https://doi.org/10.1016/S1044-5803\(00\)00113-3](https://doi.org/10.1016/S1044-5803(00)00113-3).
- [16] K. K. Ray and D. Mondal. "The effect of interlamellar spacing on strength of pearlite in annealed eutectoid and hypoeutectoid plain carbon steels". In: *Acta Metallurgica et Materialia* 39.10 (1991), pp. 2201–2208. DOI: 10.1016/0956-7151(91)90002-I.
- [17] P. Clayton and D. Danks. "Effect of interlamellar spacing on the wear resistance of eutectoid steels under rolling-sliding conditions". In: *Wear* 135 (1990), pp. 369–389. DOI: [https://doi.org/10.1016/0043-1648\(90\)90037-B](https://doi.org/10.1016/0043-1648(90)90037-B).
- [18] K. Nakase and I. M. Bernstein. "The Effect of Alloying Elements and Microstructure on the Strength and Fracture Resistance of Pearlitic Steel". In: *Metallurgical and Materials Transactions A* 19.11 (1988), pp. 2819–2829. DOI: <https://doi.org/10.1007/BF02645816>.
- [19] A. R. Marder and B. L. Bramfitt. "The Effect of Morphology on the Strength of Pearlite". In: *Metallurgical Transactions A* 7 (1976), pp. 365–372. DOI: <https://doi.org/10.1007/BF02642832>.
- [20] A. R. Marder and B. L. Bramfitt. "Effect of Continuous Cooling on the Morphology and Kinetics of Pearlite". In: *Metallurgical Transactions A* 6 (1975), pp. 2009–2014. DOI: <https://doi.org/10.1007/BF03161825>.
- [21] W. Fu, T. Furuhashi, and T. Maki. "Effect of Mn and Si addition on microstructure and tensile properties of cold-rolled and annealed pearlite in eutectoid Fe-C alloys". In: *ISIJ International* 44.1 (2004), pp. 171–178. DOI: 10.2355/isijinternational.44.171.
- [22] T. S. Eyre and A. Baxter. "The formation of white layers at rubbing surfaces". In: *Tribology* 5.6 (1972), pp. 256–261. DOI: 10.1016/0041-2678(72)90104-2.
- [23] J. Takahashi, K. Kawakami, and M. Ueda. "Atom probe tomography analysis of the white etching layer in a rail track surface". In: *Acta Materialia* 58.10 (2010), pp. 3602–3612. DOI: 10.1016/j.actamat.2010.02.030.
- [24] J. Wu et al. "Micro and Nanoscale Characterization of Complex Multilayer-Structured White Etching Layer in Rails". In: *Metals* 8.10 (2018), p. 749. DOI: 10.3390/met8100749.
- [25] P. Clayton and M. B. P. Allery. "Metallurgical aspects of surface damage problems in rails". In: *Canadian Metallurgical Quarterly* 21.1 (1982), pp. 31–46. DOI: 10.1179/cmq.1982.21.1.31.
- [26] G. Baumann, K. Knothe, and H.J. Fecht. "Surface modification, corrugation and nanostructure formation of high speed railway tracks". In: *Nanostructured Materials* 9.1-8 (1997), pp. 751–754. DOI: 10.1016/S0965-9773(97)00162-1.

- [27] A. Al-Juboori et al. "Squat formation and the occurrence of two distinct classes of white etching layer on the surface of rail steel". In: *International Journal of Fatigue* 104 (2017), pp. 52–60. DOI: 10.1016/j.ijfatigue.2017.07.005.
- [28] S. Simon et al. "Tribological characterization of rail squat defects". In: *Wear* 297 (2013), pp. 926–942. DOI: 10.1016/j.wear.2012.11.011.
- [29] M. Steenbergen. "Rolling contact fatigue in relation to rail grinding". In: *Wear* 356-357 (2016), pp. 110–121. DOI: 10.1016/j.wear.2016.03.015.
- [30] M. Steenbergen. "Rolling contact fatigue: Spalling versus transverse fracture of rails". In: *Wear* 380-381 (2017), pp. 96–105. DOI: 10.1016/j.wear.2017.03.003.
- [31] M. Steenbergen and R. Dollevoet. "On the mechanism of squat formation on train rails - Part I: Origination". In: *International Journal of Fatigue* 47 (2013), pp. 361–372. DOI: 10.1016/j.ijfatigue.2012.04.023.
- [32] R. I. Carroll and J. H. Beynon. "Rolling contact fatigue of white etching layer: Part 1. Crack morphology". In: *Wear* 262.9-10 (2007), pp. 1253–1266. DOI: 10.1016/j.wear.2007.01.003.
- [33] A. Al-juboori et al. "Microstructural changes on railway track surfaces caused by electrical leakage between wheel and rail". In: *Tribology International* 140 (2019), p. 105875. DOI: 10.1016/j.triboint.2019.105875.
- [34] C. J. Rasmussen et al. "Surface crack formation on rails at grinding induced martensite white etching layers". In: *Wear* 384-385 (2017), pp. 8–14. DOI: 10.1016/j.wear.2017.04.014.
- [35] Q. Lian et al. "Evolution of thermally induced white etching layer at rail surface during multiple wheel/train passages". In: *International Journal of Fatigue* 159 (2022), p. 106799. DOI: 10.1016/j.ijfatigue.2022.106799.
- [36] Q. Lian et al. "Thermo-mechanical coupled finite element analysis of rolling contact fatigue and wear properties of a rail steel under different slip ratios". In: *Tribology International* 141 (2020), p. 105943. DOI: 10.1016/j.triboint.2019.105943.
- [37] A. Kumar et al. "Microstructural evolution of white and brown etching layers in pearlitic rail steels". In: *Acta Materialia* 171 (2019), pp. 48–64. DOI: 10.1016/j.actamat.2019.04.012.
- [38] W. Österle et al. "Investigation of white etching layers on rails by optical microscopy, electron microscopy, X-ray and synchrotron X-ray diffraction". In: *Materials Science and Engineering A* 303.1-2 (2001), pp. 150–157. DOI: 10.1016/S0921-5093(00)01842-6.
- [39] R. Petrov, J. Wu, and J. Sietsma. "Microstructure of white etching layer of in-field loaded railway steel". In: *Scientific proceedings XIV International Congress "Machines, Technologies, Materials"*. Vol. VII. 2017, pp. 505–508.
- [40] A. Pyzalla et al. "Changes in microstructure, texture and residual stresses on the surface of a rail resulting from friction and wear". In: *Wear* 251 (2001), pp. 901–907. DOI: 10.1016/S0043-1648(01)00748-7.
- [41] J. Wu et al. "Laboratory simulation of martensite formation of white etching layer in rail steel". In: *International Journal of Fatigue* 91 (2016), pp. 11–20. ISSN: 01421123. DOI: 10.1016/j.ijfatigue.2016.05.016.

- [42] J. Takahashi. "Atom probe study on microstructure change in severely deformed pearlitic steels: Application to rail surfaces and drawn wires". In: *IOP Conference Series: Materials Science and Engineering* 219.1 (2017), p. 012007. DOI: 10.1088/1757-899X/219/1/012007.
- [43] S. B. Newcomb and W. M. Stobbs. "A transmission electron microscopy study of the white-etching layer on a rail head". In: *Materials Science and Engineering* 66.2 (1984), pp. 195–204. DOI: 10.1016/0025-5416(84)90180-0.
- [44] G. Baumann, H. J. Fecht, and S. Liebelt. "Formation of white-etching layers on rail treads". In: *Wear* 191.1-2 (1996), pp. 133–140. DOI: 10.1016/0043-1648(95)06733-7.
- [45] W. Lojkowski et al. "The mechanical properties of the nanocrystalline layer on the surface of railway tracks". In: *Materials Science and Engineering A* 303.1-2 (2001), pp. 209–215. ISSN: 09215093. DOI: 10.1016/S0921-5093(00)01948-1. arXiv: arXiv:1011.1669v3.
- [46] W. Lojkowski et al. "Nanostructure formation on the surface of railway tracks". In: *Materials Science and Engineering A* 303.1-2 (2001), pp. 197–208. ISSN: 09215093. DOI: 10.1016/S0921-5093(00)01947-X. arXiv: arXiv:1011.1669v3.
- [47] S. Pal et al. "Surface damage on new AS60 rail caused by wheel slip". In: *Engineering Failure Analysis* 22 (2012), pp. 152–165. ISSN: 1350-6307. DOI: 10.1016/j.engfailanal.2012.01.002.
- [48] R. Pan et al. "The microstructure analysis of white etching layer on treads of rails". In: *Engineering Failure Analysis* 82. January (2017), pp. 39–46. ISSN: 1350-6307. DOI: 10.1016/j.engfailanal.2017.06.018. URL: <http://dx.doi.org/10.1016/j.engfailanal.2017.06.018>.
- [49] B. H. Nguyen et al. "Fracture mechanisms in rails with mechanically and thermomechanically induced white etching layers under three-point bending". In: *Engineering Failure Analysis* 131 (2022), p. 105813. DOI: 10.1016/j.engfailanal.2021.105813.
- [50] Y. Zhou et al. "Phase and microstructural evolution in white etching layer of a pearlitic steel during rolling-sliding friction". In: *Wear* 362-363 (2016), pp. 8–17. ISSN: 00431648. DOI: 10.1016/j.wear.2016.05.007.
- [51] M. Messaadi and M. Steenbergen. "Stratified surface layers on rails". In: *Wear* 414-415. December 2017 (2018), pp. 151–162. ISSN: 00431648. DOI: 10.1016/j.wear.2018.07.019.
- [52] N. Larijani et al. "The effect of anisotropy on crack propagation in pearlitic rail steel". In: *Wear* 314.1-2 (2014), pp. 57–68. ISSN: 00431648. DOI: 10.1016/j.wear.2013.11.034. URL: <http://dx.doi.org/10.1016/j.wear.2013.11.034>.
- [53] J. W. Ringsberg and A. Bergkvist. "On propagation of short rolling contact fatigue cracks". In: *Fatigue Fracture of Engineering Materials Structures* 26 (2003), pp. 969–983.
- [54] P. Clayton and D. N. Hill. "Rolling contact fatigue of rail steel". In: *Wear* 117 (1987), pp. 319–334.

- [55] H. W. Zhang et al. "Microstructural investigation of white etching layer on pearlite steel rail". In: *Materials Science and Engineering A* 421.1-2 (2006), pp. 191–199. ISSN: 09215093. DOI: 10.1016/j.msea.2006.01.033.
- [56] S. M. C. van Bohemen. "The nonlinear lattice expansion of iron alloys in the range 100-1600 K". In: *Scripta Materialia* 69.4 (2013), pp. 315–318. DOI: 10.1016/j.scriptamat.2013.05.009. URL: <http://dx.doi.org/10.1016/j.scriptamat.2013.05.009>.
- [57] M. Jung, S. J. Lee, and Y. K. Lee. "Microstructural and dilatational changes during tempering and tempering kinetics in martensitic medium-carbon steel". In: *Metallurgical and Materials Transactions A: Physical Metallurgy and Materials Science* 40.3 (2009), pp. 551–559. ISSN: 10735623. DOI: 10.1007/s11661-008-9756-2.
- [58] J. Hidalgo and M. J. Santofimia. "Effect of Prior Austenite Grain Size Refinement by Thermal Cycling on the Microstructural Features of As-Quenched Lath Martensite". In: *Metallurgical and Materials Transactions A: Physical Metallurgy and Materials Science* 47.11 (2016), pp. 5288–5301. ISSN: 10735623. DOI: 10.1007/s11661-016-3525-4.
- [59] B. Ravi Kumar et al. "Effect of cyclic thermal process on ultrafine grain formation in AISI 304L austenitic stainless steel". In: *Metallurgical and Materials Transactions A: Physical Metallurgy and Materials Science* 40.13 (2009), pp. 3226–3234. ISSN: 10735623. DOI: 10.1007/s11661-009-0033-9.
- [60] L. Duan et al. "Austenite Grain Growth Behavior of X80 Pipeline Steel in Heating Process". In: *Journal of Iron and Steel Research International* 17.3 (2010), pp. 62–66. ISSN: 1006706X. DOI: 10.1016/S1006-706X(10)60074-X. URL: [http://dx.doi.org/10.1016/S1006-706X\(10\)60074-X](http://dx.doi.org/10.1016/S1006-706X(10)60074-X).
- [61] V. A. Alza. "Spheroidizing in Steels : Processes , Mechanisms , Kinetic and Microstructure - A Review". In: *IOSR Journal of Mechanical and Civil Engineering* 18.3 (2021), pp. 63–81. DOI: 10.9790/1684-1803036381.
- [62] W. W. Sun et al. "Advanced high strength steel (AHSS) development through chemical patterning of austenite". In: *Scripta Materialia* 146 (2018), pp. 60–63. ISSN: 13596462. DOI: 10.1016/j.scriptamat.2017.11.007.
- [63] J. L. Cunningham, D. J. Medlin, and G. Krauss. "Effects of induction hardening and prior cold work on a microalloyed medium carbon steel". In: *Journal of Materials Engineering and Performance* 8.4 (1999), pp. 401–408. ISSN: 10599495. DOI: 10.1361/105994999770346684.
- [64] S. Li et al. "Study of partition to non-partition transition of austenite growth along pearlite lamellae in near-eutectoid Fe-C-Mn alloy". In: *Acta Materialia* 177 (2019), pp. 198–208. ISSN: 13596454. DOI: 10.1016/j.actamat.2019.07.038.
- [65] Z. D. Li et al. "Kinetics of reverse transformation from pearlite to austenite in an Fe-0.6 mass pct C alloy and the effects of alloying elements". In: *Metallurgical and Materials Transactions A: Physical Metallurgy and Materials Science* 42.6 (2011), pp. 1586–1596. ISSN: 10735623. DOI: 10.1007/s11661-010-0560-4.

- [66] R. A. Jaramillo, M. T. Lusk, and M. C. Mataya. "Dimensional anisotropy during phase transformations in a chemically banded 5140 steel. Part I: Experimental investigation". In: *Acta Materialia* 52.4 (2004), pp. 851–858. ISSN: 13596454. DOI: 10.1016/j.actamat.2003.11.017.
- [67] S. J. Lee, M. T. Lusk, and Y. K. Lee. "Conversional model of transformation strain to phase fraction in low alloy steels". In: *Acta Materialia* 55.3 (2007), pp. 875–882. ISSN: 13596454. DOI: 10.1016/j.actamat.2006.09.008.
- [68] R. K. Dutta et al. "In-situ synchrotron diffraction studies on transformation strain development in a high strength quenched and tempered structural steel - Part I. Bainitic transformation". In: *Metallurgical and Materials Transactions A: Physical Metallurgy and Materials Science* 45.1 (2014), pp. 218–229. ISSN: 10735623. DOI: 10.1007/s11661-013-1992-4.
- [69] L. Cheng et al. "Lattice parameters of iron-carbon and iron-nitrogen". In: *Scripta metallurgica et materialia* 24.2 (1990), pp. 509–514.
- [70] H. S. Yang and H. K. D. H. Bhadeshia. "Austenite grain size and the martensite-start temperature". In: *Scripta Materialia* 60.7 (2009), pp. 493–495. DOI: 10.1016/j.scriptamat.2008.11.043. URL: <http://dx.doi.org/10.1016/j.scriptamat.2008.11.043>.
- [71] S. J. Lee and Y. Kook Lee. "Effect of Austenite Grain Size on Martensitic Transformation of a Low Alloy Steel". In: *Materials Science Forum* 475-479 (2005), pp. 3169–3172. DOI: 10.4028/www.scientific.net/msf.475-479.3169.
- [72] J. E. Garnham and C. L. Davis. *Rail materials*. Woodhead Publishing Limited, 2009, pp. 125–171. ISBN: 9781845696788. DOI: 10.1533/9781845696788.1.125. URL: <http://dx.doi.org/10.1533/9781845696788.1.125>.
- [73] J. E. Garnham and C. L. Davis. "The role of deformed rail microstructure on rolling contact fatigue initiation". In: *Wear* 265.9-10 (2008), pp. 1363–1372. ISSN: 00431648. DOI: 10.1016/j.wear.2008.02.042.
- [74] H. C. Eden, J. E. Garnham, and C. L. Davis. "Influential microstructural changes on rolling contact fatigue crack initiation in pearlitic rail steels". In: *Materials Science and Technology* 21 (2005), pp. 623–629. DOI: 10.1179/174328405X43207.
- [75] F. J. Franklin et al. *The evolution and failure of pearlitic microstructure in rail steel - observations and modelling*. Woodhead Publishing Limited, 2009, pp. 311–348. ISBN: 9781845696788. DOI: 10.1533/9781845696788.1.311. URL: <http://dx.doi.org/10.1533/9781845696788.1.311>.
- [76] G. R. Speich, V. A. Demarest, and R. L. Miller. "Formation of Austenite During Inter-critical Annealing of Dual-Phase Steels." In: *Metallurgical transactions. A, Physical metallurgy and materials science* 12 A.8 (1981), pp. 1419–1428. ISSN: 03602133. DOI: 10.1007/bf02643686.
- [77] D. V. Shtansky, K. Nakai, and Y. Ohmori. "Pearlite to austenite transformation in an Fe-2.6Cr-1C alloy". In: *Acta Materialia* 47.9 (1999), pp. 2619–2632. ISSN: 13596454. DOI: 10.1016/S1359-6454(99)00142-1.

- [78] Z. D. Li et al. "Nucleation of austenite from pearlitic structure in an Fe-0.6C-1Cr alloy". In: *Scripta Materialia* 60.7 (2009), pp. 485–488. ISSN: 13596462. DOI: 10.1016/j.scriptamat.2008.11.041. URL: <http://dx.doi.org/10.1016/j.scriptamat.2008.11.041>.
- [79] S. Sharma et al. "A simulation study of pearlite-to-austenite transformation kinetics in rapidly heated hot-rolled low carbon steel". In: *Materials and Design* 107 (2016), pp. 65–73. ISSN: 18734197. DOI: 10.1016/j.matdes.2016.06.025. URL: <http://dx.doi.org/10.1016/j.matdes.2016.06.025>.
- [80] G. Shen et al. "Micro-scale Cellular Automaton Modeling of Interface Evolution During Reaustenitization from Pearlite Structure in Steels". In: *Acta Metallurgica Sinica (English Letters)* 31.7 (2018), pp. 713–722. ISSN: 21941289. DOI: 10.1007/s40195-018-0706-8. URL: <https://doi.org/10.1007/s40195-018-0706-8>.
- [81] A. Jacot, M. Rappaz, and R. C. Reed. "Modelling of reaustenitization from the pearlite structure in steel". In: *Acta Materialia* 46.11 (1998), pp. 3949–3962. ISSN: 13596454. DOI: 10.1016/S1359-6454(98)00048-2.
- [82] M. Militzer. "Phase field modelling of phase transformations in steels". In: *Phase Transformations in Steels*. 2012, pp. 405–432. DOI: 10.1533/9780857096111.3.405.
- [83] V. Savran. "Austenite formation in C-Mn steel". PhD thesis. Delft University of Technology, 2009. ISBN: 9789077172407.
- [84] R. G. Thiessen, I. M. Richardson, and J. Sietsma. "Physically based modelling of phase transformations during welding of low-carbon steel". In: *Materials Science and Engineering A* 427.1-2 (2006), pp. 223–231. ISSN: 09215093. DOI: 10.1016/j.msea.2006.04.076.
- [85] J. Rudnizki et al. "Phase-field modeling of austenite formation from a ferrite plus pearlite microstructure during annealing of cold-rolled dual-phase steel". In: *Metallurgical and Materials Transactions A: Physical Metallurgy and Materials Science* 42.8 (2011), pp. 2516–2525. ISSN: 10735623. DOI: 10.1007/s11661-011-0626-y.
- [86] M. Militzer and H. Azizi-Alizamini. "Phase field modelling of austenite formation in low carbon steels". In: *Solid State Phenomena* 172-174 (2011), pp. 1050–1059. ISSN: 10120394. DOI: 10.4028/www.scientific.net/SSP.172-174.1050.
- [87] J. O. Andersson et al. "THERMO-CALC DICTRA, Computational Tools For Materials Science". In: *Calphad Computer Coupling Of Phase Diagrams And Thermochemistry* 26.2 (2002), pp. 273–312.
- [88] V. Mattos Ferreira et al. "Microstructure Development of Pearlitic Railway Steels Subjected to Fast Heating". In: *SSRN Electronic Journal* 221 (2022), p. 110989. ISSN: 0264-1275. DOI: 10.2139/ssrn.4108630. URL: <https://doi.org/10.1016/j.matdes.2022.110989>.
- [89] F. G. Caballero, C. Capdevila, and C. García De Andrés. "Influence of pearlite morphology and heating rate on the kinetics of continuously heated austenite formation in a eutectoid steel". In: *Metallurgical and Materials Transactions A: Physical Metallurgy and Materials Science* 32.6 (2001), pp. 1283–1291. ISSN: 10735623. DOI: 10.1007/s11661-001-0218-3.

- [90] A. Roósz, Z. Gácsi, and E. G. Fuchs. “Isothermal formation of austenite in eutectoid plain carbon steel”. In: *Acta Metallurgica* 31.4 (1983), pp. 509–517. ISSN: 00016160. DOI: 10.1016/0001-6160(83)90039-1.
- [91] I. Steinbach et al. “A phase field concept for multiphase systems”. In: *Physica D: Non-linear Phenomena* 94.3 (1996), pp. 135–147. ISSN: 01672789. DOI: 10.1016/0167-2789(95)00298-7.
- [92] J. Eiken. “A Phase-Field Model for Technical Alloy Solidification”. PhD thesis. Rheinisch-Westfälischen Technischen Hochschule Aachen, 2021.
- [93] M. Militzer. “Phase field modeling of microstructure evolution in steels”. In: *Current Opinion in Solid State and Materials Science* 15.3 (2011), pp. 106–115. ISSN: 13590286. DOI: 10.1016/j.cossms.2010.10.001. URL: <http://dx.doi.org/10.1016/j.cossms.2010.10.001>.
- [94] <https://micress.rwth-aachen.de/>. URL: <https://micress.rwth-aachen.de/> (visited on 03/20/2023).
- [95] G. P. Krielaart and S. van der Zwaag. “Kinetics of gamma to alpha phase transformation in Fe-Mn alloys containing low manganese”. In: *Materials Science and Technology* 14 (1998), pp. 10–18.
- [96] T. Nagano and M. Enomoto. “Calculation of the interfacial energies between  $\alpha$  and  $\gamma$  iron and equilibrium particle shape”. In: *Metallurgical and Materials Transactions A* 37.12 (2006), pp. 929–937. ISSN: 1073-5623. DOI: 10.1007/s11661-006-1013-y.
- [97] H. Azizi-Alizamini and M. Militzer. “Phase field modelling of austenite formation from ultrafine ferrite-carbide aggregates in Fe-C”. In: *International Journal of Materials Research* 101.4 (2010), pp. 534–541. ISSN: 18625282. DOI: 10.3139/146.110307.
- [98] M. G. Mecozzi et al. “The Role of Nucleation Behavior in Phase-Field Simulations of the Austenite to Ferrite Transformation”. In: *Metallurgical and Materials Transactions A* 39.June (2008), pp. 1237–1247. DOI: 10.1007/s11661-008-9517-2.
- [99] G. R. Speich, V. A. Demarest, and R. L. Miller. “Formation of Austenite During Inter-critical Annealing of Dual-Phase Steels.” In: *Metallurgical transactions. A, Physical metallurgy and materials science* 12 A.8 (1981), pp. 1419–1428. ISSN: 03602133. DOI: 10.1007/bf02643686.
- [100] M. G. Mecozzi et al. “Quantitative comparison of the phase-transformation kinetics in a sharp-interface and a phase-field model”. In: *Computational Materials Science* 50.6 (2011), pp. 1846–1853. ISSN: 09270256. DOI: 10.1016/j.commatsci.2011.01.028. URL: <http://dx.doi.org/10.1016/j.commatsci.2011.01.028>.
- [101] M. Militzer et al. “Three-dimensional phase field modelling of the austenite-to-ferrite transformation”. In: *Acta Materialia* 54.15 (2006), pp. 3961–3972. ISSN: 13596454. DOI: 10.1016/j.actamat.2006.04.029.
- [102] V. Dikshit, P. Clayton, and D. Christensen. “Investigation of rolling contact fatigue in a head-hardened rail”. In: *Wear* 144.1-2 (1991), pp. 89–102. ISSN: 00431648. DOI: 10.1016/0043-1648(91)90008-I.



- [103] M. Djahanbakhsh et al. “Nanostructure formation and mechanical alloying in the wheel/rail contact area of high speed trains in comparison with other synthesis routes”. In: *Journal of Metastable and Nanocrystalline Materials* 360-362 (2001), pp. 175–182. DOI: 10.4028/www.scientific.net/msf.360-362.175.
- [104] H. G. Feller and K. Waif. “Surface analysis of corrugated rail treads”. In: *Wear* 144 (1991), pp. 153–161.
- [105] A. Al-Juboori et al. “Characterisation of White Etching Layers formed on rails subjected to different traffic conditions”. In: *Wear* 436-437.June (2019). ISSN: 00431648. DOI: 10.1016/j.wear.2019.202998.
- [106] B. Hieu Nguyen et al. “Formation mechanism and evolution of white etching layers on different rail grades”. In: *International Journal of Fatigue* 163 (2022), p. 107100. DOI: 10.1016/j.ijfatigue.2022.107100. URL: <https://doi.org/10.1016/j.ijfatigue.2022.107100>.
- [107] Q. LI et al. “Microstructural Evolution of a Hypoeutectoid Pearlite Steel under Rolling-sliding Contact Loading”. In: *Journal of Iron and Steel Research International* 23.10 (2016), pp. 1054–1060. DOI: 10.1016/S1006-706X(16)30157-1.
- [108] P.Y. Tung et al. “Formation mechanism of brown etching layers in pearlitic rail steel”. In: *Materialia* 26.November (2022), p. 101625. ISSN: 25891529. DOI: 10.1016/j.mtla.2022.101625. URL: <https://doi.org/10.1016/j.mtla.2022.101625>.
- [109] J. M. Hyzak and I. M. Bernstein. “The role of microstructure on the strength and toughness of fully pearlitic steels”. In: *Metallurgical Transactions A* 7A (1976), pp. 1217–1224. ISSN: 03602133. DOI: 10.1007/BF02656606.
- [110] H. Yahyaoui et al. “Effect of interlamellar spacing on the elastoplastic behavior of C70 pearlitic steel: Experimental results and self-consistent modeling”. In: *Materials and Design* 55 (2014), pp. 888–897. ISSN: 0261-3069. DOI: 10.1016/j.matdes.2013.10.062. URL: <http://dx.doi.org/10.1016/j.matdes.2013.10.062>.
- [111] J. E. Garnham, R. Ding, and C. L. Davis. “Ductile inclusions in rail, subject to compressive rolling–sliding contact”. In: *Wear* 269 (2010), pp. 733–746. ISSN: 0043-1648. DOI: 10.1016/j.wear.2010.07.010. URL: <http://dx.doi.org/10.1016/j.wear.2010.07.010>.
- [112] K. Hashimoto et al. “Effect of inclusion/matrix interface cavities on internal-fracture-type rolling contact fatigue life”. In: *Materials and Design* 32 (2011), pp. 4980–4985. ISSN: 0261-3069. DOI: 10.1016/j.matdes.2011.06.056. URL: <http://dx.doi.org/10.1016/j.matdes.2011.06.056>.
- [113] J. E. Garnham and C. L. Davis. “Very early stage rolling contact fatigue crack growth in pearlitic rail steels”. In: *Wear* 271.1-2 (2011), pp. 100–112. ISSN: 00431648. DOI: 10.1016/j.wear.2010.10.004. URL: <http://dx.doi.org/10.1016/j.wear.2010.10.004>.
- [114] K. Ando, O. Hirofumi, and T. Tetsuya. “Effect of pro-eutectoid cementite on fatigue crack growth behavior of pearlitic steels”. In: *ISIJ International* 63.1 (2023), pp. 159–169.
- [115] R. Ordonez et al. “New rail steels for the 21st century”. In: *Railway Track and Structures* 104 (2008), pp. 17–21.

- [116] R. Ordóñez Olivares et al. “Advanced metallurgical alloy design and thermomechanical processing for rails steels for North American heavy haul use”. In: *Wear* 271.1-2 (2011), pp. 364–373. ISSN: 00431648. DOI: 10.1016/j.wear.2010.10.048.
- [117] K. Han, D. V. Edmonds, and G. D. W. Smith. “Optimization of mechanical properties of high-carbon pearlitic steels with Si and V additions”. In: *Metallurgical and Materials Transactions A: Physical Metallurgy and Materials Science* 32.6 (2001), pp. 1313–1324. DOI: 10.1007/s11661-001-0222-7.
- [118] A. T. Davenport and R. W. K. Honeycombe. “Precipitation of carbides at  $\gamma$ - $\alpha$  boundaries in alloy steels”. In: *Proceedings of the Royal Society of London* 322 (1971), pp. 191–205.
- [119] G. Miyamoto et al. “Interphase precipitation of VC and resultant hardening in V-added medium carbon steels”. In: *ISIJ International* 51.10 (2011), pp. 1733–1739. ISSN: 09151559. DOI: 10.2355/isijinternational.51.1733.
- [120] F. A. Khalid and D. V. Edmonds. “Interphase precipitation in microalloyed engineering steels and model alloy”. In: *Materials Science and Technology* 9.5 (1993), pp. 384–396. ISSN: 17432847. DOI: 10.1179/mst.1993.9.5.384.
- [121] K. Han, G. D.W. Smith, and D. V. Edmonds. “Pearlite phase transformation in Si and V steel”. In: *Metallurgical and Materials Transactions A* 26.7 (1995), pp. 1617–1631. ISSN: 10735623. DOI: 10.1007/BF02670750.
- [122] S. A. Parsons and D. V. Edmonds. “Microstructure and mechanical properties of medium carbon ferrite-pearlite steel microalloyed with vanadium”. In: *Materials Science and Technology* 3.11 (1987), pp. 894–904. DOI: 10.1179/mst.1987.3.11.894.
- [123] D. E. Parsons, T. F. Malis, and J. D. Boyd. “Microalloying and precipitation in Cr-V rail steels”. In: *Journal of Heat Treating* 3.3 (1984), pp. 1129–1135.
- [124] W. Solano-Alvarez et al. “Synchrotron and neural network analysis of the influence of composition and heat treatment on the rolling contact fatigue of hypereutectoid pearlitic steels”. In: *Materials Science and Engineering A* 707. July (2017), pp. 259–269. ISSN: 09215093. DOI: 10.1016/j.msea.2017.09.045. URL: <https://doi.org/10.1016/j.msea.2017.09.045>.
- [125] F. Fang et al. “Effect of vanadium on the microstructure and property of rebar steel”. In: *Materials Science Forum* 928 MSF (2018), pp. 269–272. ISSN: 16629752. DOI: 10.4028/www.scientific.net/MSF.928.269.
- [126] F. B. Pickering and B. Garbarz. “Strengthening in pearlite formed from thermomechanically processed austenite in vanadium steels and implications for toughness”. In: *Materials Science and Technology* 5.3 (2012), pp. 227–237. ISSN: 02670836. DOI: 10.1179/026708389790343317.
- [127] F. A. Khalid and D. V. Edmonds. “Effect of vanadium on the grain boundary carbide nucleation of pearlite in high-carbon steels”. In: *Scripta Metallurgica et Materialia* 30.10 (1994), pp. 1251–1255. ISSN: 0956716X. DOI: 10.1016/0956-716X(94)90254-2.

- [128] A. M. Elwazri, P. Wanjara, and S. Yue. "Dynamic recrystallization of austenite in microalloyed high carbon steels". In: *Materials Science and Engineering A* 339.1-2 (2003), pp. 209–215. ISSN: 09215093. DOI: 10.1016/S0921-5093(02)00164-8.
- [129] A. M. Elwazri, S. Yue, and P. Wanjara. "Effect of prior-austenite grain size and transformation temperature on nodule size of microalloyed hypereutectoid steels". In: *Metallurgical and Materials Transactions A* 36 (2005), pp. 2297–2305. ISSN: 1073-5623. DOI: 10.1007/s11661-005-0102-7.
- [130] S. T. Fonseca et al. "Effects of Vanadium on the Continuous Cooling Transformation of 0.7 % C Steel for Railway Wheels". In: *Defect and Diffusion Forum* 367 (2016), pp. 60–67. ISSN: 16629507. DOI: 10.4028/www.scientific.net/DDF.367.60.
- [131] EN ISO 6892-1. *Metallic materials - Tensile testing - Part 1: Method of test at room temperature*. CEN, 2019.
- [132] EN 13674-1. *Railway applications - Track - Rail - Part 1: Vignole railway rails 46 kg/m and above*. CEN, 2011.
- [133] J. Wen et al. "Comparison of microstructure changes induced in two pearlitic rail steels subjected to a full-scale wheel/rail contact rig test". In: *Wear* 456-457.November 2019 (2020), p. 203354. ISSN: 00431648. DOI: 10.1016/j.wear.2020.203354. URL: <https://doi.org/10.1016/j.wear.2020.203354>.
- [134] S. Maya-Johnson, A. J. Ramirez, and A. Toro. "Fatigue crack growth rate of two pearlitic rail steels". In: *Engineering Fracture Mechanics* 138 (2015), pp. 63–72. ISSN: 00137944. DOI: 10.1016/j.engfracmech.2015.03.023. URL: <http://dx.doi.org/10.1016/j.engfracmech.2015.03.023>.
- [135] K. Han, G. D. W. Smith, and D. V. Edmonds. "Pearlite phase transformation in Si and V steel". In: *Metallurgical and Materials Transactions A* 26.7 (1995), pp. 1617–1631. DOI: 10.1007/BF02670750.
- [136] J. G. Zimmerman, H. R. Aborn, and E. C. Bain. "Some effects of small additions of vanadium to eutectoid steel , 1937, 25, 755-788". In: *ASM Transactions* 25 (1937), pp. 755–788.
- [137] C. Zhen et al. "Influence of Vanadium Microalloying on Isothermal Transformation Behavior of Eutectoid Steel". In: *Physics of Metals and Metallography* 120.10 (2019), pp. 936–942. ISSN: 15556190. DOI: 10.1134/S0031918X19100120.
- [138] X. L. Pan and M. Umemoto. "Precipitation Characteristics and Mechanism of Vanadium Carbides in a V-Microalloyed Medium-Carbon Steel". In: *Acta Metallurgica Sinica (English Letters)* 31.11 (2018), pp. 1197–1206. ISSN: 21941289. DOI: 10.1007/s40195-018-0775-8. URL: <https://doi.org/10.1007/s40195-018-0775-8>.
- [139] K. Han et al. "Effects of vanadium addition on nucleation and growth of pearlite in high carbon steel". In: *Materials Science and Technology* 10.11 (1994), pp. 955–963. ISSN: 17432847. DOI: 10.1179/mst.1994.10.11.955.
- [140] G. Miyamoto, Y. Karube, and T. Furuhashi. "Formation of grain boundary ferrite in eutectoid and hypereutectoid pearlitic steels". In: *Acta Materialia* 103 (2016), pp. 370–381. ISSN: 13596454. DOI: 10.1016/j.actamat.2015.10.032.

- [141] W. Solano-Alvarez, L. Fernandez Gonzalez, and H. K. D. H. Bhadeshia. “The effect of vanadium alloying on the wear resistance of pearlitic rails”. In: *Wear* 436-437 (2019), p. 203004. ISSN: 00431648. DOI: 10.1016/j.wear.2019.203004. URL: <https://doi.org/10.1016/j.wear.2019.203004>.
- [142] R. G. Baker and J. Nutting. “Precipitation Processes in Steels”. In: *Special Report No. 64*. London: The Iron and Steel Institute, 1959, pp. 1–22.
- [143] T. Maejima et al. “Lattice strain and strength evaluation on V microalloyed pearlitic steel”. In: *ISIJ International* 60.8 (2020), pp. 1810–1818. ISSN: 09151559. DOI: 10.2355/isijinternational.ISIJINT-2019-708.
- [144] P. I. Christodoulou, A. T. Kermanidis, and G. N. Haidemenopoulos. “Fatigue and fracture behavior of pearlitic Grade 900A steel used in railway applications”. In: *Theoretical and Applied Fracture Mechanics* 83 (2016), pp. 51–59. ISSN: 01678442. DOI: 10.1016/j.tafmec.2015.12.017.
- [145] A. Hohenwarter et al. “Effect of Large Shear Deformations on the Fracture Behavior of a Fully Pearlitic Steel”. In: *Metallurgical and Materials Transactions A* 42.6 (2011), pp. 1609–1618. ISSN: 1073-5623. DOI: 10.1007/s11661-010-0541-7.
- [146] Y. Zhao et al. “In situ study of cementite deformation and its fracture mechanism in pearlitic steels”. In: *Materials Science and Engineering: A* 731 (2018), pp. 93–101. ISSN: 09215093. DOI: 10.1016/j.msea.2018.05.114.
- [147] M. Dollar, I. M. Bernstein, and A. W. Thompson. “Influence of deformation substructure on flow and fracture of fully pearlitic steel”. In: *Acta Metallurgica* 36.2 (1988), pp. 311–320. ISSN: 00137944. DOI: 10.1016/j.msea.2018.05.114. URL: <https://doi.org/10.1016/j.msea.2018.05.114> <http://dx.doi.org/10.1016/j.engfracmech.2010.02.003>.
- [148] A. R. Rosenfield, G. T. Hahn, and J. D. Embury. “Fracture of Steels Containing Pearlite”. In: *Metallurgical Transactions* 3 (1972), pp. 2797–2804. DOI: 10.1007/BF02652845.

# LIST OF PUBLICATIONS

## PUBLICATION RELATED TO THE THESIS

### Journal papers

1. **V. Mattos Ferreira**, M.G. Mecozzi, R.H. Petrov, J. Sietsma, "Microstructure development of pearlitic railway steels subjected to fast heating", *Materials & Design*, 2022, vol. 221, 110989;
2. **V. Mattos Ferreira**, M.G. Mecozzi, R.H. Petrov, J. Sietsma, "Details of pearlite to austenite transformation: experiments and phase-field modeling", *Computational Materials Science*, 2023, vol. 228, 112368;
3. **V. Mattos Ferreira**, B. Schotsman, M.G. Mecozzi, R.H. Petrov, J. Sietsma, "Microstructural characterization of hypereutectoid pearlitic steel containing vanadium", *Materials Characterization*, 2024, submitted;

## OTHER PUBLICATIONS

### Journal papers

1. K. Nikolic, **V. Mattos Ferreira**, L. Malet, T. Depover, K. Verbeken, R. H. Petrov, "Uncovering the white etching area and crack formation mechanism in bearing steel", *Materials Characterization*, 2023, vol. 197, 112659;
2. A. Sood, J. Schimmel, **V. Mattos Ferreira**, M. Bosman, C. Goulas, V. Popovich, M.J.M. Hermans, "Directed energy deposition of Invar 36 alloy using cold wire pulsed gas tungsten arc welding: effect of heat input on the microstructure and functional behaviour", *Journal of Materials Research and Technology*, 2023;

### Conference papers

1. D. Leonetti, **V. Mattos Ferreira**, B. Schotsman, "Fracture behavior and mechanical characterization of R350HT rail steel", *Procedia Structural Integrity*, 2023;



# ACKNOWLEDGEMENTS

First, I wanted to thank my promotors Jilt Sietsma and Roumen Petrov for allowing me to do a PhD at the MSE Department of TU Delft.

Jilt, thank you for your openness to discuss any topic, your support in changing the initial project proposal to an alternative route, the constant (and quick) feedback on my research outputs and your suggestions to significantly improve the quality of my work. I learned a lot about Materials Science from you and I truly admire your intelligence and your way of thinking.

Roumen, thank you for your more practical inputs on the experimental part of my thesis, your availability to help me not only perform but also analyze EBSD and TEM data, and your help in looking for collaborations where I could perform my experiments.

I would like to especially thank Pina Mecozzi for playing an essential role in the completion of this work. You not only helped me perform all phase-field simulations but also agreed on reading, discussing, and revising all the work done in this thesis. Step by step it became clear that you were the daily supervisor I wish I had since the beginning of my PhD. Thank you for all the support, for being kind to me on days when I was not feeling confident enough, and for explaining some complicated topics numerous times until I had no doubts left. Your strong interest in understanding the reason why things happen the way they do is inspiring to me. It was a pleasure to navigate through this male-dominated academic world having you as a female role model to look for.

This thesis has also been positively influenced by the successful scientific collaboration I had with several researchers. It has been a pleasure working with Bart Schotsman (Pro-Rail/TU Delft), Davide Leonetti (TU Eindhoven), Marc van Maris (TU Eindhoven), Dominik Weil (KLA), Steven Lewis (British Steel), Andrew Wilson (British Steel) and Jacob Corteen (British Steel). Thank you for the interesting discussions and suggestions to improve this work.

A big portion of this research was based on experimental data which required the assistance of several specialists who agreed to teach, help, and discuss with me different aspects of each technique used. For this, I am thankful to Kees Kwakernaak, Remko Seijffers, Sander van Asperen, Nico Gerlofs, Hans Hofman, Jurriaan van Slingerland, Richard Huizenga, Ruud Hendriks, Ton Riemslog, Durga Mainali Sharma, Frans Tichelaar and Vitaliy Bliznuk (UGhent).

I would also like to thank Prisca Koelman not only for arranging my meetings with my promotors but also for answering all the bureaucratic questions I had. Reina and Imas thank you for the nice talks whenever we met in the corridors and Jan van Turnhout for making me feel like an IT expert even if I don't have much knowledge about computers.

I also would like to thank Prof. Dilson Silva dos Santos for helping me doing an internship in Grenoble (FR) where I had the pleasure to work with Dr. Laetitia Laversenne who was essential for my approval in this PhD position at TU Delft.

I consider myself very lucky to have been surrounded by amazing colleagues over these five years, sharing lunch times, laughs, coffee breaks, PhD sports events (go Marsenite!),

M2i Conferences, and most importantly: cakes! For this reason, I wanted to thank Viviam, Arthur, Alfonso, Sudhindra, Wei, Vibhor, Tim Boot, Virginia, Sajaad, Elsa, Pablo, Xiaohui, Gesa, Luis, Farnaz, Naveena, Joep, Gaojie, Philipp, Arjun, José, Amir, Mohammed, Camila, Aravind, Konstantina, Can, Jia-Ning, Tim Djedilbaev, Gautham, Naveen and Zhaorui. I also would like to thank Francesca, Wenli and Meilin who were not from my department but were still present in fun out-of-office activities.

I wanted to especially thank Jithin, Jhon, Soroush, and Daniel who became my small family in the Netherlands. Jithin, you were my first friend in the office and, since the first day we met, I simply knew that we would become friends. Not even in my wildest dreams I would've imagined sharing my PhD journey with someone from India who could speak (almost fluent) Portuguese! Your connection with Brazil made me feel at home and as I joked many times: you sometimes seem more Brazilian than Indian! I always felt no barriers while talking to you and I guess this represents the great friendship we have. Thank you for the incredible moments, stupid jokes, laughs and tears shared.

Next, I would like to thank Jhon, who is one of the best people I had the pleasure to meet in the Netherlands. You are a reliable friend (almost like a brother to me), always offering me your shoulder whenever I need the most. Your unique sense of humor often caught me off-guard, which rendered pure moments of joy laughing at our misfortune haha.

After some time in the department, I met Soroush. I don't exactly remember when or why we became friends but I am glad for that. You were always ready for ANYTHING and even proposed the weirdest activities such as going to a camper's exhibition even though none of us could afford one. I just hope that I will never have to be belayed by you in the future (actually, no one should, it's PURE DANGER!).

The last one I met was Daniel, my fellow Brazilian. It was great to speak my native language during working hours and share some things that only you could understand. Through these four guys, I also met Raquel, Ana, Eszter, Rosana and Fabio who became my "small community" in the Netherlands. Thank you guys for all the Brazilian barbecues, parties, pizza at BarSil, afternoons by the lake/canals, homemade dinners, King's Day and most importantly for making my life in the Netherlands happier than I could've thought.

I also wanted to thank my Brazilian friends Bianca Guimarães, Ronaldo, Gabi, Paloma, Caroline Pessanha, Isabela, Bruno and Ana for our friendship and for finding ways to be connected despite living in different countries.

A special thanks to my psychologist Juliana Caravelos who was essential for the completion of this thesis. I met you during one of those moments when I was sure that the world was falling apart and that nothing could save me from the inevitable failure. After many sessions, you helped me see some light in the darkness, understand and compartmentalize my problems, and act by solving each one of them at a time. Thank you for leading me in the right direction (considering all my limitations) and reassuring me that I was able to finish the PhD at my own pace (and indeed you were right!). Thank you once more for your amazing and necessary work.

Some friends come on a long journey together and these are mine: Caroline, Grolla, Polyana, Alanna, and Bianca. Thank you for providing me with a safe space to express myself freely, for the empowering conversations and for always cheering for my achievements! I am looking forward to the countless karaoke sessions where we'll sing "Umbrella" together and the memories we have yet to create.

I would like to thank my relatives not only for always showing your support by sending



comforting messages during these years away from Brazil but also for making sure I had a great time whenever I was back home.

My grandparents Jirvânio e Sônia also deserve special thanks for being two of the most important people in my life. Thank you for helping take care of me and my brother, for the amazing holidays in the beach house when we were kids, for all the lessons and laughter we had together, and most importantly for the immeasurable love and respect you constantly showed us. Thank you also for all the support and encouragement when I decided to move to another continent. I couldn't be more grateful for having such amazing grandparents. I hope our journey together lasts many more years! I love you!

I also would like to thank my brother Emanuel who, together with Tamiris, gave our family the best gift so far: our precious Miguel. Unfortunately, it took me a long time to even meet Miguel (the downside of living on the other side of the ocean). However, seeing his pictures every day filled my heart with joy and gave me the additional strength I needed in the final months to complete this thesis. Emanuel, although the distance, work, and different time zones make our contact a bit limited, I want you to know that you can always count on me just like I am sure that you'll always be there when I need you.

Dad and mom, I have no words to describe your importance in my life. You both sacrificed so much for me to have a good education. Dad, thank you for all your hard and long working hours with little to no annual vacations to provide for our family. I hope you know that you play an essential role in all my achievements. Mom, you are simply my biggest inspiration. You always prioritized knowledge so much in our lives even if you didn't have all the opportunities we had. I can say for sure that without your incentive, I wouldn't have reached so far academically. I would probably not even be able to write this thesis in English as you were the one pushing for us to start learning English at a very young age. Thank you for the extreme and sometimes unappreciated effort you put into making my life more comfortable so that I only had to focus on my education. Thank you both for supporting my decision to live abroad even if it meant sacrificing our daily contact, I know it was/is not easy. I love you with all my heart!

Finally, only one person can understand what I've experienced during these 5 years of my PhD, and that's you Marcolino. We started this journey together in 2018 when we both moved to the Netherlands to pursue our PhDs and also build our lives together. I can say for sure that I wouldn't have finished this PhD without you. You were always by my side when I needed someone to talk to, to hug, or simply forget about the PhD for a while. Because of you, I tried so many different things in the past 5 years: bouldering, mountain biking, a 3-day bike trip, Survival Run and even hiking very long (and steep!) distances which I would've never thought I was able to (being the big-city girl you constantly make fun of!). Most of these activities rendered moments of pure fear (with lots of tears from my side) but with your encouragement (and my unbreakable strength haha), I always managed to cross the finish line. Thank you for your patience and understanding. I can't wait to complain more and more about how annoying you can be on purpose! Grazie per tutto, io ti voglio tanto bene.

Vitória Mattos Ferreira  
Amsterdam, 2024



# AGRADECIMENTOS

Primeiramente, eu gostaria de agradecer aos meus orientadores Jilt Sietsma e Roumen Petrov por me proporcionarem a oportunidade seguir meu doutorado no Departamento de MSE da TU Delft.

Roumen, obrigada pelas suas sugestões na parte experimental da minha tese, por sua disponibilidade para me ajudar não apenas a realizar, mas também a analisar dados de EBSD e TEM, e sua ajuda para buscar colaborações de outros institutos onde eu poderia conduzir meus experimentos.

Jilt, obrigada pela sua abertura para discutir qualquer tópico, seu apoio em modificar a proposta inicial do projeto para uma rota alternativa, pelo feedback constante (e rápido) sobre os resultados da minha pesquisa e suas sugestões para melhorar significativamente a qualidade do meu trabalho. Aprendi muito sobre Ciência dos Materiais com você e realmente admiro sua inteligência e sua forma de pensar.

Gostaria de agradecer especialmente a Pina Mecozzi por seu papel essencial para a conclusão deste trabalho. Você não só me ajudou a realizar todas as simulações de transformação de fase, mas também concordou em ler, discutir e revisar todo o trabalho feito nesta tese. Passo a passo, ficou claro que você era a supervisora que eu gostaria de ter tido desde o início do meu doutorado. Obrigada por todo o apoio, por ser gentil comigo nos dias em que eu não me sentia confiante o suficiente e por explicar alguns tópicos complicados incessantemente até que eu sanasse completamente minhas dúvidas. Seu forte interesse em entender o motivo pelo qual as coisas acontecem do jeito que acontecem é inspirador para mim. Foi um prazer navegar por este mundo acadêmico predominantemente masculino tendo você como uma referência feminina.

Esta tese também foi positivamente influenciada pela colaboração científica que tive com pesquisadores de outros departamentos ou instituições. Foi um prazer trabalhar com Bart Schotsman (ProRail/TU Delft), Davide Leonetti (TU Eindhoven), Marc van Maris (TU Eindhoven), Dominik Weil (KLA), Steven Lewis (British Steel), Andrew Wilson (British Steel) e Jacob Corteen (British Steel). Obrigada pelas discussões interessantes e sugestões para o aprimoramento científico desse trabalho.

Grande parte desta pesquisa foi baseada em dados experimentais que exigiram a assistência de vários especialistas que concordaram em me ensinar, ajudar e discutir diferentes aspectos de cada técnica utilizada. Por isso, sou grata a Kees Kwakernaak, Remko Seijffers, Sander van Asperen, Nico Gerlofs, Hans Hofman, Jurriaan van Slingerland, Richard Huizenga, Ruud Hendriks, Ton Riemsdag, Durga Mainali Sharma, Frans Tichelaar e Vitaliy Bliznuk (UGhent).

Gostaria também de agradecer a Prisca Koelman, não apenas por agendar minhas reuniões com meus orientadores, mas também por me ajudar em todas as questões burocráticas relacionadas ao meu doutorado. A Reina e Imas, obrigada pelas conversas agradáveis sempre que nos encontrávamos nos corredores, e a Jan van Turnhout, por me fazer sentir como uma especialista em TI, mesmo que eu não tenha muito conhecimento sobre computadores.

Também gostaria de agradecer ao Prof. Dilson Silva dos Santos (UFRJ) por me dar a oportunidade de estagiar em Grenoble (FR), onde tive o prazer de trabalhar com a Dra. Laetitia Laversenne, fundamental para a minha aprovação nesta posição de doutorado na TU Delft.

Considero-me muito sortuda por ter sido cercada por colegas incríveis ao longo desses cinco anos, compartilhando almoços, risadas, pausas para café, eventos esportivos (vai Marsenite!), Conferências M2i e, o mais importante, bolos! Por esse motivo, gostaria de agradecer a Viviam, Arthur, Alfonso, Sudhindra, Wei, Vibhor, Tim Boot, Virginia, Sajaad, Elsa, Pablo, Xiaohui, Gesa, Luis, Farnaz, Naveena, Joep, Gaojie, Philipp, Arjun, José, Amir, Mohammed, Camila, Aravind, Konstantina, Jia-Ning, Tim Djedilbaev, Gautham, Naveen e Zhaorui. Gostaria também de agradecer a Francesca, Wenli e Meilin, Cristian, Jiayu Li e Ksenija, que não eram do meu departamento, mas ainda estavam presentes em atividades fora do escritório.

Gostaria de agradecer especialmente a Jithin, Jhon, Soroush e Daniel, que se tornaram minha pequena família nos Países-Baixos. Jithin, você foi meu primeiro amigo no departamento e, desde o primeiro dia em que nos conhecemos, eu simplesmente soube que nos tornaríamos amigos. Nem nos meus melhores sonhos eu imaginaria compartilhar minha jornada de doutorado com alguém nascido na Índia que falasse (quase fluentemente) Português! Sua conexão com o Brasil me fez sentir em casa, e como eu sempre digo: às vezes você parece mais brasileiro do que indiano! Eu sempre senti que não havia barreiras enquanto conversava com você, e acredito que isso representa a grande amizade que contruímos. Obrigada pelos momentos incríveis, piadas bobas, risadas e lágrimas compartilhadas.

A seguir, gostaria de agradecer a Jhon, que é uma das melhores pessoas que tive o prazer de conhecer na Holanda. Você é realmente um amigo confiável (quase como um irmão para mim), sempre oferecendo seu ombro quando mais preciso. Seu senso de humor único muitas vezes me pegou de surpresa, resultando em momentos puros de alegria rindo das nossas próprias desventuras haha.

Depois de algum tempo no departamento eu conheci o Soroush. Não lembro exatamente quando ou por que nos tornamos amigos, mas sou muito feliz por isso. Você sempre estava pronto para QUALQUER COISA e até propunha as atividades mais inusitadas, como ir a uma exposição de campers, mesmo que nenhum de nós pudesse comprar um. Só espero que eu nunca tenha que ser "belayed" por você no futuro enquanto fazemos escalada (na verdade, ninguém deveria, é PERIGO PURO!).

O último que conheci foi Daniel, meu querido compatriota. Foi ótimo falar minha própria língua durante o expediente e compartilhar algumas coisas que apenas você poderia entender. Através desses quatro, também conheci Raquel, Ana, Eszter, Rosana e Fabio, que se tornaram minha "pequena comunidade" nos Países-Baixos. Obrigada a todos pelos churrascos brasileiros, festas, pizzas no BarSil, tardes à beira do lago/canais, jantares caseiros, Dia do Rei (King's Day) e, o mais importante, por tornar minha vida nos Países-Baixos mais feliz do que eu poderia imaginar.

Um agradecimento especial à minha psicóloga Juliana Caravelos, que foi fundamental para a conclusão desta tese. Eu a conheci durante um daqueles momentos em que eu estava certa de que o mundo estava desmoronando e que nada poderia me salvar do inevitável fracasso. Depois de longas sessões, você me ajudou a enxergar uma pequena luz em meio a escuridão, a entender e compartimentalizar meus problemas e agir resolvendo cada um deles no momento certo. Obrigada por me guiar na direção certa (considerando todas as

minhas limitações) e me assegurar que eu seria capaz de terminar o doutorado no meu próprio ritmo (e, realmente, você estava certa!). Mais uma vez, obrigada pelo seu trabalho incrível e necessário.

Queria também agradecer aos meus amigos brasileiros Bianca Guimarães, Ronaldo, Gabi, Paloma, Caroline Pessanha, Isabela, Bruno e Ana pela amizade e por encontrarem maneiras de manter nossa conexão apesar de morarmos em países diferentes.

Alguns amigos têm uma longa jornada juntos, e essas são as minhas: Caroline, Grolla, Polyana, Alanna e Bianca. Obrigada por me fornecerem um espaço seguro para me expressar livremente, pelas conversas empoderadoras e por sempre torcerem pelos meus feitos! Estou ansiosa para as inúmeras sessões de karaokê onde cantaremos "Umbrella" juntas e as memórias que ainda temos que criar.

Gostaria de agradecer a todos os meus familiares não apenas por mostrarem sempre seu apoio enviando mensagens reconfortantes durante esses anos longe do Brasil, mas também por garantirem que eu tivesse uma ótima estadia sempre que voltasse para casa.

Meus avós Jirvânio e Sônia também merecem agradecimentos especiais por serem duas das pessoas mais importantes da minha vida. Obrigada por ajudarem a cuidar de mim e do meu irmão, pelas incríveis férias na casa de praia quando éramos crianças, por todas as lições e risadas que compartilhamos e, mais importante, pelo amor e respeito imensuráveis que constantemente nos mostraram. Obrigada também por todo o apoio e encorajamento quando decidi me mudar para outro continente. Não poderia ser mais grata por ter avós tão incríveis. Espero que nossa caminhada juntos dure muitos anos! Amo vocês!

Também gostaria de agradecer ao meu irmão Emanuel, que, junto com Tamiris, deu à nossa família o melhor presente até agora: nosso precioso Miguel. Infelizmente, levei muito tempo para conhecer Miguel (o lado negativo de viver do outro lado do Oceano). No entanto, ver suas fotos todos os dias encheu meu coração de alegria e me deu a força adicional que eu precisava nos últimos meses para concluir esta tese. Emanuel, embora a distância, o trabalho e os diferentes fusos horários limitem um pouco nosso contato, quero que saiba que você sempre pode contar comigo, assim como tenho certeza de que você sempre estará pronto para me ajudar quando eu precisar.

Pai e mãe, não tenho palavras para descrever importância de vocês em minha vida. Vocês dois sacrificaram muito para que eu tivesse uma boa educação. Pai, obrigada por todas as suas longas horas de trabalho árduo, com poucas ou mesmo sem férias anuais, para sustentar nossa família. Espero que você saiba que desempenha um papel essencial em todas as minhas conquistas. Mãe, você é simplesmente minha maior inspiração. Você sempre priorizou o conhecimento em nossas vidas, mesmo que você não tenha tido todas as oportunidades que nós tivemos. Posso afirmar com certeza que, sem seu incentivo, eu não teria chegado tão longe academicamente. Na verdade, eu provavelmente nem conseguiria escrever esta tese em inglês, pois foi você quem nos incentivou a aprender inglês desde muito pequenos. Obrigada pelo esforço extremo - e por vezes não apreciado - que você fez para tornar minha vida o mais confortável possível para que eu focasse apenas nos meus estudos. Sou muito grata a vocês por apoiarem minha decisão de morar fora do Brasil, mesmo que isso significasse sacrificar nosso contato diário, eu sei que não foi e nem é fácil. Eu os amo com todo o meu coração!

Apenas uma pessoa pode entender o que vivi durante esses cinco anos de doutorado, e essa pessoa é você, Marcolino. Começamos essa jornada juntos em 2018, quando ambos nos mudamos para os Países-Baixos para cursar nossos doutorados e também construir

nossas vidas juntos. Posso afirmar com certeza que eu não teria concluído este doutorado sem você. Você sempre esteve ao meu lado quando eu precisava de alguém para conversar, abraçar ou simplesmente esquecer de tudo por um tempo. Por sua causa, eu experimentei muitas coisas diferentes nos últimos 5 anos: escalada, ciclismo de montanha, uma viagem de bicicleta de três dias, corrida de obstáculos e até mesmo trilhas muito longas (e íngremes!), que eu nunca teria pensado ser capaz (sendo a garota da cidade grande que você constantemente zomba!). A maioria dessas atividades rendeu momentos de puro medo (com muitas lágrimas do meu lado) mas com seu incentivo (e minha força inabalável haha), sempre consegui cruzar a linha de chegada. Obrigada pela sua paciência e compreensão. Mal posso esperar para reclamar cada vez mais sobre o quão chato você pode ser de propósito! Muito obrigada por tudo, io ti voglio tanto bene!

Por fim, gostaria de agradecer a Deus e à todas as pessoas que me colocaram em suas orações para que eu alcançasse meus sonhos.

Vitória Mattos Ferreira  
Amsterdão, 2024

# BIOGRAPHY

Vitória Mattos Ferreira was born in Rio de Janeiro, Brazil in 1995. She received a Bachelor's degree in Materials Science and Engineering from the Federal University of Rio de Janeiro, Brazil, in 2018. From 2018 to 2023 she has been working towards a Ph.D. in the field of materials science and engineering at the Delft University of Technology, the Netherlands.

# Propositions

accompanying the dissertation

## MICROSTRUCTURAL PHENOMENA IN PEARLITIC RAILWAY STEELS

by

**Vitória MATTOS FERREIRA**

1. White and brown etching layers in railway steels are formed due to the combination of mechanical loadings and temperature. (*this thesis*)
2. Phase transformation simulation of pearlite to austenite indicates the importance of carbon inhomogeneities in the formation of white etching layers. (*this thesis*)
3. Laser heating can be used as an effective way of reproducing white and brown etching layer formation due to frictional heating in controlled laboratory conditions. (*this thesis*)
4. The push for green steel production should not be seen as a hurdle for the steel industry but rather as a chance to revitalize a well-established scientific discipline.
5. Scientific development is essential not only to combat a global crisis but also to prevent it.
6. Open discussions on mental health help reduce stigma, but addressing the root causes remains necessary for improvement.
7. A good education system for all individuals is the basis for social and economic development.
8. The resistance to feminism reflects how females are still not seen nor treated as equal in modern society.
9. The exposure to different cultures is an interesting way of discovering the unique qualities and specificities of your own culture.
10. Privilege awareness is the first step towards social equity.

These propositions are regarded as opposable and defensible, and have been approved as such by the promoters Prof. dr. ir. J. Sietsma and Prof. dr. ir. R. H. Petrov.



